Intermittent events and structure propagation in plasma turbulence

INAUGURALDISSERTATION

zur

Erlangung des akademischen Grades eines

doctor rerum naturalium (Dr. rer. nat.)

an der Mathematisch-Naturwissenschaftlichen Fakultät

der

Ernst-Moritz-Arndt-Universität Greifswald

vorgelegt von
Thomas Windisch
geboren am 15.04.1978
in Berlin

Greifswald, im März 2007

Dekan:	Prof. Dr. K. Fesser
1. Gutachter:	Prof. Dr. T. Klinger
2. Gutachter:	Prof. Dr. U. Stroth
Tag der Promotion:	4. Mai 2007

Abstract

Turbulence is an omnipresent phenomenon in nature. Its main characteristics, fluctuations under a wide spread of spatial and temporal scales, are observed in neutral fluid or gaseous systems as well as in plasmas. Although the electromagnetic character of a plasma makes plasma turbulence more complex, the basic features of turbulence are universal. In magnetically confined plasmas, fluctuating plasma parameters give rise to turbulent transport of plasma particles and energy, which degrades the confinement and affects key issues of future fusion devices. The intermittent character of this convective particle flux is associated with high-amplitude turbulent structures, called "blobs", propagating radially outwards across the magnetic field. Also the intermittent fluctuations observed in the plasma edge of devices with linear magnetic field geometry seem to be related to propagating turbulent structures. The mechanism of the radial propagation is however poorly understood. The present thesis reports on the formation and radial propagation of turbulent structures in the linearly magnetized VINETA helicon device. By imaging the fluctuations in the azimuthal plane with multi-dimensional probe arrays, it is demonstrated that turbulent structures develop out of drift-wave turbulence in the maximum plasma density gradient region. The turbulent structures propagate mainly azimuthally in direction of the background $\boldsymbol{E}\times\boldsymbol{B}$-drift but they exhibit also a strong radial velocity component. The radial propagation is caused by the self-consistent potential of the turbulent structures. They are the main contributors to fluctuation-induced radial transport. In the plasma edge the turbulent structures occur as intermittent density bursts with high amplitudes. A comparison of the experimental findings with numerical three-dimensional fluid simulations with appropriate geometry and boundary conditions reveals consistency, i.e., the formation of the turbulent structures is causally connected with a quasi-coherent drift mode and their radial propagation is caused by the self-consistent electric field that develops due to their three-dimensional dynamics. For a comparison with a fusion plasma, the propagation properties of turbulent structures in the edge plasma of the National Spherical Torus Experiment (NSTX) are investigated and compared with the common propagation models.

Zusammenfassung

Turbulenz ist allgegenwärtig in der Natur. Ein wichtiges Charakteristikum sind Fluktuationen auf einer Vielzahl von räumlichen und zeitlichen Skalen, die sowohl in neutralen Fluiden und gasförmigen Systemen, als auch in Plasmen beobachtet werden. Obwohl der elektromagnetische Charakter von Plasmen eine erhöhte Komplexität von Plasmaturbulenz bedingt, sind die grundlegenden Eigenschaften universell. In magnetisch eingeschlossenen Plasmen führen fluktuierende Plasmaparameter zu turbulentem Transport von Plasmateilchen und Energie, der die Einschlusszeit verringert und wichtige Aspekte zukünftiger Fusionskraftwerke beeinflusst. Der intermittente Charakter dieses konvektiven Teilchenflusses ist verbunden mit turbulenten Strukturen mit großen Amplituden, auch "blobs" genannt, die radial durch das Magnetfeld propagieren. Intermittente Fluktuationen im Randplasma von Experimenten mit linearer Magnetfeldgeometrie werden ebenfalls propagierenden turbulenten Strukturen zugeschrieben. Dabei ist der Mechanismus der radialen Propagation kaum verstanden. In dieser Arbeit wird die Bildung und Propagation von turbulenten Strukturen im linear magnetisierten Helikonexperiment VINETA untersucht. Durch Messungen der Fluktuationen in der azimuthalen Ebene mit multi-dimensionalen Sonden wird gezeigt, dass turbulente Strukturen in Driftwellenturbulenz im Gebiet des maximalen Dichtegradienten entstehen. Die turbulenten Strukturen propagieren hauptsächlich azimuthal in Richtung der Hintergrund $\boldsymbol{E} \times \boldsymbol{B}$-Drift, aber sie besitzen auch eine starke radiale Geschwindigkeitskomponente. Die radiale Propagation wird durch das selbstkonsistente Potential der turbulenten Struktur verursacht, dass zu einem fluktuations-induzierten radialen Transport führt. Im Plasmarand werden die turbulenten Strukturen als intermittente Dichteeruptionen mit großen Amplituden beobachtet. Ein Vergleich der experimentellen Ergebnisse mit numerischen dreidimensionalen Fluid-Simulationen mit abgestimmten Geometrie- und Randbedingungen zeigt Übereinstimmung. Die Bildung der turbulenten Strukturen ist kausal mit einer quasikohärenten Driftmode verbunden und ihre radiale Propagation wird durch das selbstkonsistente elektrische Feld verursacht, dass aus der dreidimensionalen Dynamik resultiert. Zum Vergleich wird die Propagation von turbulenten Strukturen im Randplasma vom National Spherical Torus Experiment (NSTX) untersucht und mit theoretischen Propagationsmodellen verglichen.

Contents

1

Introduction - a primer to the turbulence problem

Turbulence is an ubiquitous phenomenon in nature that affects various physical processes, ranging from molecular to astrophysical scales. Although turbulence is the most common state of fluid and gas flows under a wide range of natural conditions, among others also Feynman (1918-1988) believed that a comprehensive turbulence description is the most important challenge in classical physics. Regardless of a strict mathematical definition, the basic characteristics of turbulent flows can be observed in our everyday life, e.g. the disordered smoke of a cigarette or smoke stacks, water flowing from a pipe with high velocity or dye injected into a fluid at high speed. Turbulence in all systems exhibits universal features: The flow is unsteady, irregular, disordered in time and space, seemingly random and unpredictable. The turbulent motions span over many spatial scales and can be observed from large eddies - comparable in size to the geometry of the system - to the smallest scales that can be barely resolved with the pure eye. Another important characteristic of turbulent flows is its ability to transport and to mix fluid and gases much more efficiently than molecular diffusion. This process can be studied e.g. by observing a cup of coffee. To mix efficiently milk and coffee without permanent stirring one only has to stir it strongly once and let the turbulent flow do the rest. Of course diffusion would eventually yield the same result but on a much larger time scale (and the coffee gets cold). While the universal character of turbulence makes it being an interesting research subject for physicists, it is also a challenging subject for many engineering processes. For example the drag of an aircraft's wing or a ship's hull is increased by turbulent flows and the combustion in car engines is mainly determined by turbulent mixing of matter and heat.
Boundary conditions or external forces (like the stirring process) impose certain constraints on the dynamics of a turbulent flow which might lead to a breakdown of universality, especially for the large scales. The universal character of turbulence is observed from the intermediate to small scales, where the dynamics is determined on the one hand by the rate at which they receive energy from the large scales and on the other hand by the

viscosity. Hence the small-scale motion is universal and independent of the actual flow geometry.

The first systematic observations and a concise description of turbulent water flows were done by Leonardo da Vinci (1492-1519), who reported on its characteristic swirling motion. The first detailed laboratory experiments on turbulent flows were conducted by Reynolds (1842-1912), who analyzed the transition from a laminar flow in a pipe to a turbulent flow [1]. He found that the dynamical stability of the system for incompressible fluids is determined by a single, dimensionless parameter, the Reynolds number $R = LU/\nu$. The quantities L and U are the typical length and velocity scales of the flow and ν is the kinematic viscosity. The Reynolds number can be interpreted as the ratio of inertial to dissipative forces of the fluid. For low Reynolds numbers, the flow is laminar and bears a certain amount of symmetry while for $R \approx 50$ the onset of the formation of nonlinear, spinning vortices (or eddies) can be observed, known as "von-Karman street" [2]. An example of a flow passing a circular obstacle at a Reynolds number of $R = 140$ is shown in Fig. 1.1a. The propagating eddies are coherent structures, i.e. their lifetime is much larger than the eddy turnover time, which is the time it takes to transport the flow energy and momentum across the eddy. The same behavior can also be observed in the earth's atmosphere around high mountains leading to the formation of swirling clouds. For large Reynolds numbers $R > 1800$ the flow is in a state of fully developed turbulence, where the eddies merge into a quasi-uniform turbulent wake (Fig. 1.1b).

The formation of spatiotemporal structures is a characteristic feature of many instabilities. For example the Kelvin-Helmholtz instability, driven by a sheared flow, can be observed in the mixing layer between two flows of different velocities in laboratory experiments [4] but also in the earth's magnetosphere [5] related to space weather phenomena. Another instability, the Rayleigh-Taylor instability, occurs if a dense, heavy fluid is supported against gravity by a lighter fluid. A characteristic feature of the Rayleigh-Taylor instability is the formation of bubble structures of the heavy fluid penetrating into the lighter fluid. The same effect is observed in supernova explosions at the interface between the

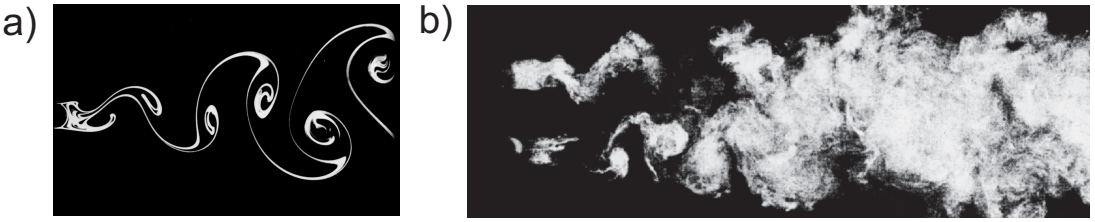

Figure 1.1: a) Development of a 'von-Karman vortex street' in a fluid flow passing a circular obstacle at $R = 140$ (a) and the merging of vortices into a turbulent wake at $R = 1800$ (b). Pictures are taken from Refs. [2] and [3].

hot gas ejected in the explosion and the interstellar medium [6].
The dynamics of turbulence in incompressible fluids (here the flow field is divergence-free) can be entirely described by the Navier-Stokes momentum equation that was already derived in 1822 [7]:

$$\partial_t \boldsymbol{u} + \boldsymbol{u} \cdot \nabla \boldsymbol{u} = \frac{\nabla p}{\rho} + \nu \nabla^2 \boldsymbol{u} \qquad \text{with} \qquad \nabla \cdot \boldsymbol{u} = 0. \tag{1.1}$$

Here $\boldsymbol{u}(\boldsymbol{r}, t)$ denotes the velocity field, $p(\boldsymbol{r}, t)$ the pressure, ρ the mass density and ν the kinematic viscosity. By rewriting the Reynolds number

$$R = \frac{LU}{\nu} = \frac{U^2}{L} \cdot \frac{L^2}{\nu U} = \frac{\boldsymbol{u} \cdot \nabla \boldsymbol{u}}{\nu \nabla^2 \boldsymbol{u}} \tag{1.2}$$

one recognizes that the Reynolds number describes the "competition" between the nonlinear term and the dissipation. For turbulent flows at high Reynolds numbers the nonlinear term dominates the dynamics. The energy of the flow ($E = m\boldsymbol{u}^2/2$) is redistributed by the nonlinear term over all scales of motion without affecting the global energy budget [3]. In this sense the Reynolds number can also be interpreted as the ratio of energy transfer between different spatial scales and dissipation, which predominantly occurs at small scales. The mechanism of local transfer of energy in wavenumber space was first expressed by Richardson [8], who took inspiration from cloud observations and from a poem of Jonathan Swift [9]:

> "Big whorls have little whorls,
> Which feed on their velocity;
> And little whorls have lesser whorls,
> And so on to viscosity
> (in the molecular sense)."

In this sense turbulence is organized as a hierarchy of eddies spanning over all spatial scales of turbulent motion, breaking up during their evolution into smaller and smaller eddies. The energy cascade from large to small eddies is known as Richardson-cascade [8]. Based on the ideas of the Richardson cascade Kolmogorov formulated in 1941 the theory of locally isotropic turbulence [10] (also known as K41 theory). The energy cascade in wavenumber space together with the resulting energy spectrum is schematically shown in Fig. 1.2a. Energy input into the system occurs on large scales (injection range) due to some stirring process. This region is separated from the dissipative range on smaller scales where the energy is transferred into heat. In the intermediate region, the inertial range, the eddies form a hierarchy of scales $l_n = l_0 r^n$ with l_0 being the largest eddy scale and $0 < r < 1$ [3]. Kolmogorov conjectured that this self-similarity is universal and the

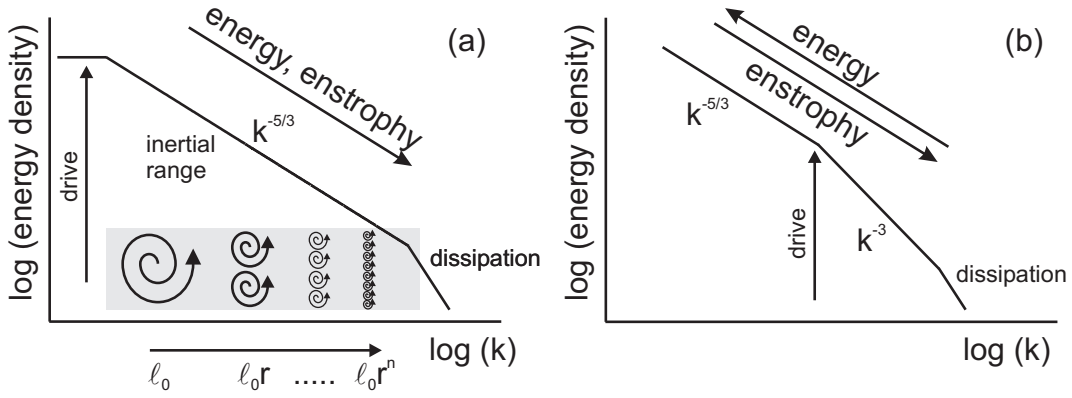

Figure 1.2: Energy power spectrum of 3D isotropic turbulence (a) and 2D turbulence (b) in neutral fluids. The inset shows schematically the hierarchy of eddies of different scales.

energy spectrum in the inertial range only depends on the energy transfer rate or mean flux of energy $\langle\epsilon\rangle$ from large to small scales. From dimensional arguments Kolmogorov found that in 3D isotropic turbulence the energy spectrum scales as $E \sim \epsilon^{2/3}k^{-5/3}$, which is often in agreement with experimental observations [11]. In general fluid turbulence is three-dimensional but under certain circumstances the system can reduce to two dimensions. This reduction can be due to geometric constraints, e.g. the boundary conditions in thin soap film experiments, or if the flow itself is restricted to two dimensions. Examples are rotating fluids and gaseous systems, where the Coriolis force restricts the flow to a plane perpendicular to the axis of rotation like an accretion disk around a rapidly spinning system as stars or planets. To understand the main differences between 3D and 2D turbulence the Navier-Stokes equation (1.1) is rewritten in terms of the vorticity $\boldsymbol{\omega} = \nabla \times \boldsymbol{u}$, which is related to the local rotation of fluid elements:

$$(\partial_t + \boldsymbol{u} \cdot \nabla)\,\boldsymbol{\omega} = \boldsymbol{\omega} \cdot \nabla \boldsymbol{u} + \nu \nabla^2 \boldsymbol{\omega}. \tag{1.3}$$

The first term on the right hand side describes the production of vorticity due to vorticity stretching and tilting while the second term describes the reduction of vorticity due to viscosity. The production of vorticity is based on the conservation of angular momentum: Imagine a spinning eddy embedded in an incompressible fluid. If the eddy is stretched in the direction of its angular momentum vector, e.g. due to a velocity gradient in the flow, it becomes at the same time narrower in the other directions and the eddy spins up.
In the 2D Navier-Stokes equation

$$(\partial_t + \boldsymbol{u} \cdot \nabla)\,\boldsymbol{\omega} = \nu \nabla^2 \boldsymbol{\omega} \tag{1.4}$$

the vorticity production term vanishes. Consequently in an ideal ($\nu = 0$) incompressible 2D fluid, both energy and enstrophy (the squared magnitude of the vorticity) are conserved. The conservation of energy and enstrophy under the action of nonlinearity imposes several constraints on the dynamics. The main consequence is the dual cascade of energy and enstrophy which was first formulated by Kraichnan [12]. The principle of the dual cascade is shown in Fig. 1.2b. In contrast to the three-dimensional situation, energy is now injected at intermediate scales and is cascaded inversely to smaller wavenumbers (larger scales) while the enstrophy is cascaded directly to large wavenumbers (smaller scales). In the energy and enstrophy inertial ranges the energy spectrum scales as $E \sim k^{-5/3}$ and $E \sim k^{-3}$, respectively. Note that energy can still be transferred towards smaller scales, nevertheless the majority goes into the large scales. The dual cascade is observed in soap film experiments [13].

A specific feature of two-dimensional turbulence is the formation of coherent vortices directly connected to the inverse cascade. This has been intensively studied experimentally [4; 14] and in numerical simulations [15]. The presence of coherent structures localized in wavenumber space strongly affects the scaling of the energy spectrum, since it perturbs the non-local self-similarity concept in the inertial ranges. Moreover, it was realized that the occurrence of coherent structures is strongly linked with intermittency [16; 17]. The definition of intermittency used here goes back to Frisch [3]: *"A signal is intermittent, if it displays activity during a fraction of time only, which decreases with the scale under consideration."*

However, the characteristic features of turbulence can not only be observed in neutral fluids and gaseous flows but also in electric plasmas. A plasma behaves in many respects similar to a fluid and thus can be described as a fluid consisting of charged particles, whose dynamics is also governed by electric and magnetic fields. The basic approach to describe plasma dynamics is known as Magnetohydrodynamics (MHD). Different to the Navier-Stokes equation for a neutral fluid, in a plasma the current $\boldsymbol{J}$ and the magnetic field $\boldsymbol{B}$ enter the momentum equation owing to the Lorentz force

$$\rho \left(\partial_t + \boldsymbol{u} \cdot \nabla\right) \boldsymbol{u} = -\nabla p + \boldsymbol{J} \times \boldsymbol{B}. \tag{1.5}$$

The dynamical state is here characterized by the magnetic Reynolds number R_m

$$R_m == \frac{uL}{\eta} = \frac{L^2/\eta}{L/u}, \tag{1.6}$$

where η is the magnetic diffusivity. The magnetic Reynolds number is the ratio between the characteristic time scale for the diffusion of a magnetic field L^2/η and the charac-

teristic time scale of turbulence $\tau = L/u$. The similarity between the MHD momentum equation and the Navier-Stokes equation suggests already that the characteristics of turbulence exhibit the same features. Intermittency and the formation of coherent structures has been observed experimentally in the solar wind [18] and in numerical simulations [19]. In MHD turbulence the energy is cascaded directly both in two and three dimensions with $E \sim k^{-3/2}$ (known as Irishnikhov-Kraichnan spectrum) [20] but nevertheless an inverse cascade also exists (e.g. the magnetic helicity in three-dimensions) that is closely related to the dynamo effect, i.e., the generation of large-scale magnetic fields by turbulent fluid motion [21].

Although the basic characteristics of neutral fluid and MHD turbulence are very similar, the complexity in the latter one is greatly enhanced. In particular electromagnetic effects give rise to several types of instabilities that can not be observed in neutral fluids. The situation gets even more complex since MHD is a simplified description of a plasma. To fully recover the plasma dynamics observed in magnetically confined plasmas, more advanced plasma descriptions as two-fluid models or kinetic approaches are necessary. A distinct number of plasma instabilities can be attributed to plasma pressure gradients, which are inevitable in laboratory devices due to the spatial limitations by material boundaries. Examples for plasma pressure driven instabilities are the drift-wave instability and the interchange instability. It is worthwhile to note that both plasma instabilities are also observed in fluid or gaseous systems: The analogon of the drift-wave instability is the Røssby wave [22]. It is due to gradients in the corriolis force and can be observed in the earth's atmosphere. The interchange instability is the analogon of the Rayleigh-Taylor instability in neutral fluids. Similar to neutral fluids, the instabilities act as a stirring process and introduce energy into the system which is then transferred via the nonlinearity towards different spatial scales. The external magnetic field imposes an important constraint on the direction of the energy transfer: The turbulent advection velocity is restricted to a plane perpendicular to the ambient magnetic field. Hence, plasma turbulence is basically two-dimensional, with the energy being transferred mainly to large scale eddies (dual cascade).

Plasma turbulence attracted much attention during the last decades. The interest is motivated by experimental observations of surprisingly high particle and energy fluxes across the confining magnetic field, which cannot be explained by diffusive processes [23]. It was soon realized that turbulent transport is a major mechanism for energy losses [24; 25], degrading the plasma confinement time and affecting key issues like erosion of wall material. Thereby, the turbulent transport controls the evolution of the plasma parameter profiles. It has been experimentally observed, that the convective particle flux across the confining magnetic field is governed by large-scale coherent eddies [26; 27; 28; 29],

which emerge from broad-band turbulence in the plasma edge. In the plasma edge the magnetic field lines are still closed and radial transport perpendicular to the magnetic field is the only mechanism for plasma losses to material surfaces. The turbulent eddies propagate into the scrape-off layer (SOL), where the magnetic field lines intersect with material boundaries, and eventually reach the first wall. In the SOL the propagating turbulent structures are associated with an intermittent fluctuation of plasma parameters and they appear as density bursts with amplitudes, which are significantly larger than the background density. The formation process of these turbulent structures is poorly understood. A direct link between an inverse transfer of energy, which is most likely provided by pressure gradient driven instabilities, and the formation process of the turbulent structures has not been reported yet.

The present thesis is dedicated to gain insight into the formation and propagation mechanism of turbulent structures under experimentally well defined conditions. The measurements are done in the linearly magnetized laboratory device VINETA. In contrast to fusion devices the overall complexity is greatly reduced due to the cylindrical geometry of the device, the homogeneous magnetic field, and negligible temperature and electromagnetic fluctuations. These limitations strongly reduce the number of involved plasma instabilities. Detailed investigations have shown [30; 31] that the governing instability in VINETA is the drift-wave instability. The knowledge of the primary instability is a major advantage in turbulence research. Coherent drift-waves, characterized by a spatiotemporal mode structure, can be destabilized by external control parameters as e.g. the external magnetic field. The destabilization of coherent drift modes leads to the onset of drift-wave turbulence, where the formation of turbulent structures is observed. Similar to the findings in toroidal fusion devices, the turbulent structures propagate radially outwards across the confining magnetic field and occur as intermittent density bursts with high amplitudes.

The present thesis is organized as follows: In Ch. 2 the drift-wave mechanism is outlined and a brief introduction into linear and non-linear drift-wave and drift-wave turbulence models is given. The diagnostic setup and the applied signal processing techniques to extract the turbulent structures are compiled in Ch. 3. An overview of the VINETA device, the basic experimental features of the drift-wave instability and the transition to drift-wave turbulence is given in Ch. 4. The experimentally obtained spatiotemporal intermittent fluctuations are analyzed in detail in Ch. 5. They are compared with numerical simulations in Ch. 6. The propagation properties of turbulent structures in the plasma edge of a spherical tokamak device, the National Spherical Torus Experiment (NSTX), have also been investigated. The results are presented in Ch. 7. Finally, in Ch. 8 a summary is given and conclusions are drawn.

2

Theory of drift waves and drift-wave turbulence

A common feature of magnetoplasmas limited by material boundaries is the occurrence of gradients in the plasma profiles, especially perpendicular to the magnetic field, which represent a source of free energy and are able to drive instabilities. One of the most important instability is the drift-wave instability, also called a "universal" instability since it develops in any geometry of the confining magnetic field. The drift-wave instability was first discovered in cylindrical Q-machines with homogeneous magnetic field in the 1960's [32; 33] followed by an initial theoretical description [34]. Already the early investigations were motivated by the associated drift-wave turbulence [35] and related transport phenomena [36]. In the subsequent years substantial measurements have been performed with respect to the destabilization of drift modes [37; 38] and the characterization of its spatiotemporal vortex structure [39; 40]. The observation of drift-wave type fluctuations in high-temperature plasmas with toroidal magnetic field geometry (for instance in tokamaks) [41] suggested that drift waves are responsible for the anomalous transport perpendicular to the confining magnetic field. Moreover, numerical simulations based on nonlinear drift wave models [42; 43] demonstrated the formation of large-scale coherent structures in drift-wave turbulence [44], a fact which has been confirmed by experimental observations [45; 46].
In the following sections the basic mechanism of the drift-wave instability is described and a brief introduction into common nonlinear drift wave models is given.

2.1 Physical picture

The basic mechanism of drift waves is illustrated in Fig. 2.1. For the moment being we consider an isothermal plasma ($\nabla p = T\nabla n$) with a density gradient ∇n perpendicular to the external homogeneous magnetic field $\boldsymbol{B} = B\hat{\boldsymbol{z}}$ and pointing in the $-\hat{\boldsymbol{x}}$-direction. Note that throughout the thesis the directions parallel ($\|$) and perpendicular ($\perp$) are always with respect to the ambient magnetic field. If a small-amplitude harmonic density perturbation $\tilde{n}$ of the background density n_0 located in the density gradient region is assumed

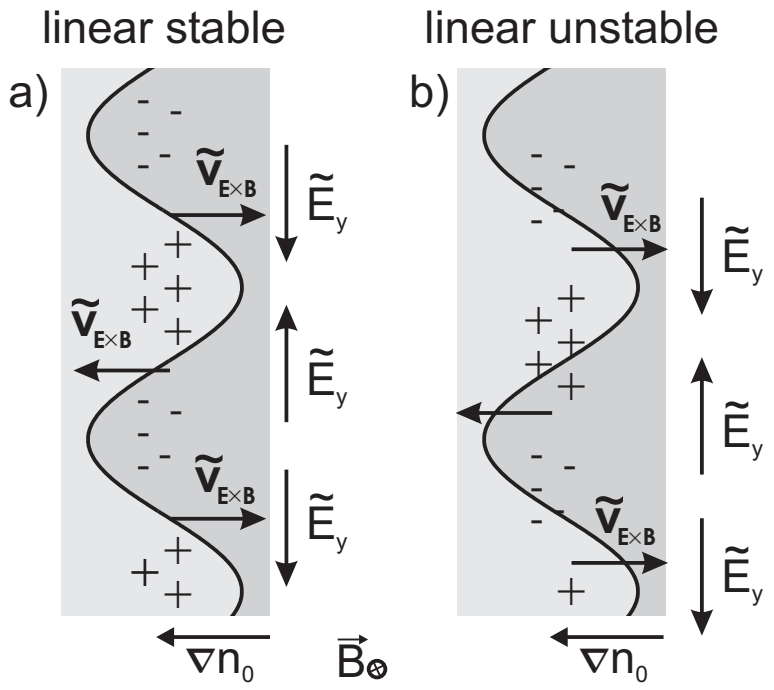

Figure 2.1: Schematic illustration of the drift-wave mechanism. A sinusoidal density perturbation perpendicular to the density gradient region ∇n_0 and magnetic field $\boldsymbol{B}$ causes a perturbation of the space charge potential. If density and potential perturbation are in phase the drift-wave is linearly stable (a) and becomes linearly unstable (b) if the perturbations are phase-shifted.

(Fig. 2.1a), the density perturbation causes a perturbation of the space-charge potential due to the different mobility of electrons and ions parallel to the magnetic field. In the region of the positive density perturbations (the perturbed density exceeds the background density) electrons respond to the increased pressure and move instantly away along the magnetic field leaving behind a positive space charge $\tilde{\phi}$. The inverse process happens in regions of negative density perturbation. The resulting non-stationary electric field $\tilde{E}_y(t)$ gives rise to a polarization drift of the ions perpendicular to the magnetic field to ensure quasi-neutrality. The electric field $\tilde{E}_y(t)$ causes a local $\boldsymbol{E}\times\boldsymbol{B}$-drift, which advects the plasma in $\hat{\boldsymbol{x}}$-direction resulting in a displacement of the perturbation in $\hat{\boldsymbol{y}}$-direction. Consequently, the initial perturbation propagates in direction of the electron diamagnetic drift velocity $\boldsymbol{v}_{de} \sim \nabla n_0 \times \boldsymbol{B}$. However, in this simple model the electric field does not amplify the perturbation and the drift wave is linearly stable. This is due to the assumed adiabatic electron response parallel to the magnetic field, which means that the electrons are in thermodynamic equilibrium, characterized by the Boltzmann relation

$$\tilde{n} = n_0 \exp\left(\frac{e\tilde{\phi}}{T_\mathrm{e}}\right). \tag{2.1}$$

Thus, the density and potential perturbations are in phase. Any violation of the adiabatic electron response results in a non-vanishing phase shift. Such a situation is depicted in Fig. 2.1b. Here the potential perturbation lags behind the density perturbation and the $\boldsymbol{E}\times\boldsymbol{B}$-drift causes an amplification of the density perturbation, meaning that the drift waves are linearly unstable. The parallel electron response can be affected by several processes, the most important ones being plasma resistivity (Coulomb collisions and electron-neutral collisions), magnetic induction and kinetic effects like Landau damping. However, it should be stressed that the drift wave is not associated with a motion of plasma particles in the direction of the electron diamagnetic drift. Due to the tight coupling between parallel and perpendicular dynamics the drift wave also exhibits a parallel wavelength $\boldsymbol{k}_{\parallel} << \boldsymbol{k}_{\perp}$, which makes a drift wave being three-dimensional. A specific feature of drift waves are spatiotemporal mode structures that evolve in geometries with periodic boundary conditions (here cylindrical geometry). In the following sections a brief introduction into common nonlinear drift wave models is given.

2.2 Basic plasma equations

In the framework of the present thesis the drift-wave models are based on the two-fluid plasma description. Drift-wave models in cylindrical geometry with homogeneous magnetic field are based on the following set of two-fluid equations [47] for each particle specie (electrons and ions with $\alpha = e, i$):

• **Continuity equation:**

$$\partial_t n_\alpha + \nabla \cdot (n_\alpha \boldsymbol{v}_\alpha) = 0. \tag{2.2}$$

• **Momentum equation:**

$$m_\alpha n_\alpha \mathrm{d}_t \boldsymbol{v}_\alpha = -\nabla \cdot \boldsymbol{\Pi}_\alpha + q_\alpha n_\alpha \left(\boldsymbol{E} + \boldsymbol{v}_\alpha \times \boldsymbol{B}\right) + q_\alpha n_\alpha \left(\frac{\boldsymbol{J}^\alpha_\parallel}{\sigma^\alpha_\parallel} + \frac{\boldsymbol{J}^\alpha_\perp}{\sigma^\alpha_\perp}\right) + \boldsymbol{F}_\alpha, \tag{2.3}$$

with conductivities

$$\sigma_\perp = \frac{q_\alpha^2 n_\alpha}{m_\alpha \nu_\alpha} \qquad \text{and} \qquad \sigma_\parallel = 1.96 \cdot \sigma_\perp, \tag{2.4}$$

where ν_α denotes the Coulomb collision frequency. The stress tensor $\boldsymbol{\Pi}$ splits up into an isotropic part $p = nT$ and an anisotropic part. The latter is also known as magnetic viscosity tensor and accounts for ion-ion collisions and finite Larmor radius (FLR) effects. The term $\boldsymbol{F}_\alpha = m_\alpha n_\alpha \nu_{\alpha n} \boldsymbol{v}_\alpha$ arises from momentum loss due to collisions between the particle specie α and the neutral background gas.

• **Maxwell's equations:**

$$\nabla \cdot \boldsymbol{B} = 0, \tag{2.5}$$

$$\nabla \times \boldsymbol{B} = \mu_0 \epsilon_0 \partial_t \boldsymbol{E} + \mu_0 \boldsymbol{J}, \tag{2.6}$$

$$\nabla \cdot \boldsymbol{E} = \frac{\rho}{\epsilon_0}, \tag{2.7}$$

$$\nabla \times \boldsymbol{E} = -\partial_t \boldsymbol{B}. \tag{2.8}$$

In the electrostatic limit, Faraday's law simplifies to $\nabla \times \boldsymbol{E} = 0$, which yields $\boldsymbol{E} = -\nabla\phi$ or rewritten as Poisson equation $\nabla^2\phi = -\rho/\epsilon_0$. The treatment can be simplified, since drift waves are low frequency waves and the time light needs to pass the plasma domain with size L is much shorter compared to the drift-wave time scales T, $L/c << T$ or equivalently $\partial_t/c << \nabla$. In this non-relativistic limit the displacement current can be neglected.

• **Quasi-neutrality:**

$$\nabla \cdot \boldsymbol{J} = 0. \tag{2.9}$$

The convective derivative describes the transformation from the co-moving frame to the laboratory frame:

$$\mathrm{d}_t = \left(\partial_t + \boldsymbol{v} \cdot \nabla\right). \tag{2.10}$$

According to Ref. [48] the drift velocities perpendicular to the magnetic field are defined as

$$\boldsymbol{E}\times\boldsymbol{B}\text{-drift:} \quad \boldsymbol{v}^{\perp}_{E\times B} = \frac{1}{B^2}\boldsymbol{B} \times \nabla_{\perp}\phi,$$

$$\text{diamagnetic drift:} \quad \boldsymbol{v}^{\perp}_{d,\alpha} = \frac{1}{q n_\alpha B^2}\,\boldsymbol{B} \times \nabla p_\alpha,$$

$$\text{polarization drift:} \quad \boldsymbol{v}^{\perp}_{p,\alpha} = \frac{m_\alpha}{qB^2}\,\boldsymbol{B} \times \mathrm{d}_t \boldsymbol{v}_{\perp}.$$

For simplicity the symbol $(\perp)$ is in the following sections omitted for the perpendicular drift velocities. $\boldsymbol{E}\times\boldsymbol{B}$-drift and diamagnetic drift are first order drifts whereas the polarization drift is a second order drift. The latter is retained for the following reason: The $\boldsymbol{E}\times\boldsymbol{B}$-drift has no charge dependence and consequently is equal for electrons and ions. In other words there is no current $\boldsymbol{J} = en(\boldsymbol{v}_i - \boldsymbol{v}_e)$ associated with the $\boldsymbol{E}\times\boldsymbol{B}$-drift. However, the diamagnetic current is divergence–free in a homogeneous magnetic field and therefore the ion polarization current is the only perpendicular contribution to the quasi-neutrality condition

$$\nabla \cdot \boldsymbol{J} = \nabla \cdot \boldsymbol{J}_{\perp} + \nabla \cdot \boldsymbol{J}_{\parallel} = 0, \tag{2.11}$$

that governs the coupling between parallel and perpendicular dynamics. Due to the small electron inertia the electron polarization drift can be neglected, while the ion diamagnetic drift is negligible for cold ions.

2.3 Hasegawa-Mima model

Based on the above equations a simple model (known as Hasegawa-Mima model) can be formulated that describes two-dimensional drift-wave turbulence in a plane perpendicular to the ambient magnetic field. Since the background density n_0 is the only stationary quantity in this model,

$$n(\boldsymbol{r},t) = n_0(\boldsymbol{r}) + \tilde{n}(\boldsymbol{r},t), \tag{2.12}$$

the superscript $\sim$ is neglected in the following for the fluctuating quantities.
The basic assumptions of this dissipationless model are

a) adiabatic electron response:

$$n = n_0 \exp\left(\frac{e\phi}{T_\mathrm{e}}\right), \tag{2.13}$$

b) cold ions:

$$T_\mathrm{i} = 0 \qquad \Longrightarrow \qquad \nabla p_i = 0, \tag{2.14}$$

and

c) electrostatic fluctuations:

$$\boldsymbol{E} = -\nabla\phi. \tag{2.15}$$

In the electrostatic limit the ion polarization drift $\boldsymbol{v_p}$ can be written as

$$\boldsymbol{v}_p = \frac{M}{eB^2}\boldsymbol{B}\times \mathrm{d}_t\boldsymbol{v}_\perp = \frac{M}{eB^2}\boldsymbol{B}\times \mathrm{d}_t\boldsymbol{v}_{E\times B} = -\frac{M}{eB^2}\mathrm{d}_t\nabla_\perp\phi. \tag{2.16}$$

Inserting the perpendicular ion velocity $\boldsymbol{v}_\perp = \boldsymbol{v}_{E\times B} + \boldsymbol{v}_p$ into the ion continuity equation yields

$$\mathrm{d}_t \ln n + \boldsymbol{v}_{E\times B}\cdot\nabla_\perp \ln n_0 + \nabla\cdot\boldsymbol{v}_\perp = 0 \tag{2.17}$$

or equivalently

$$\mathrm{d}_t\left(\frac{e\phi}{T_\mathrm{e}} - \frac{M}{eB^2}\nabla_\perp^2\phi\right) - \frac{\nabla_\perp\phi\times\boldsymbol{B}}{B}\cdot\nabla_\perp \ln n_0 = 0. \tag{2.18}$$

Normalization with typical time and length scales

$$\frac{e\phi}{T_\mathrm{e}} \to \phi \quad \frac{t}{\Omega_{ci}} \to t \quad \rho_s \nabla \to \nabla, \tag{2.19}$$

where $\rho_s = \sqrt{k_B T_e M/e^2 B^2}$ is the drift scale and $\Omega_{ci} = eB/M$ is the ion cyclotron frequency, yields the Hasegawa-Mima equation

$$\partial_t(\nabla_\perp \phi - \phi) + (\hat{\boldsymbol{z}} \times \nabla_\perp \phi) \cdot \nabla_\perp (\nabla_\perp^2 \phi) - \kappa_n \partial_y \phi = 0, \tag{2.20}$$

with $\kappa_n = -\partial_x \ln n_0(x)$. Introducing the Poisson-bracket notation

$$\{f, g\} = \partial_x f \partial_y g - \partial_y f \partial_x g = \hat{\boldsymbol{z}} \cdot (\nabla_\perp f \times \nabla_\perp g) \tag{2.21}$$

a more compact formulation of the Hasegawa-Mima equation can be obtained

$$\boxed{\partial_t(\nabla_\perp^2 \phi - \phi) - \kappa_n \partial_y n_0 + \{\phi, \nabla_\perp \phi\} = 0.} \tag{2.22}$$

The Hasegawa-Mima equation [42] was first derived in 1978 although a similar equation for Røssby waves has already been derived earlier [22]. By rewriting the Hasegawa-Mima equation (2.22) in terms of a potential vorticity $q = \phi - \nabla_\perp^2 \phi - \kappa_n$ one obtains

$$(\partial_t - \boldsymbol{v}_{E\times B} \cdot \nabla_\perp)\, q = 0. \tag{2.23}$$

In this notation, the Hasegawa-Mima equation is formally equivalent with the the incompressible two-dimensional Navier-Stokes equation (1.4) in the dissipationless limit (also known as Euler equation). From the linearized Hasegawa-Mima equation a drift wave dispersion relation is obtained by looking for plane-wave solutions

$$\phi(\boldsymbol{r}, t) = \sum_k \phi_k \exp\left(i\boldsymbol{k} \cdot \boldsymbol{r} - i\omega t\right) \tag{2.24}$$

to obtain

$$\omega = \frac{\kappa_n k_y}{1 + k_\perp^2} = \frac{\omega^\star}{1 + k_\perp^2}, \tag{2.25}$$

where

$$\omega^\star = \frac{k_B T_e}{eB} \frac{k_y}{L_\perp} = \frac{k_B T_e}{eB} k_y |\partial_x \ln n_0| \tag{2.26}$$

is the electron diamagnetic drift frequency. Transformed back to physical units the drift wave dispersion relation reads

$$\boxed{\omega = \frac{\omega^\star}{1 + \rho_s^2 k_\perp^2}.} \tag{2.27}$$

Since the Hasegawa-Mima equation assumes adiabaticity, the drift wave frequency is a real valued quantity, indicating linear stability. This is of course not the right picture. However, if sufficiently large amplitudes are initialized the basic nonlinear evolution of drift waves can be studied by means of the Hasegawa-Mima model. Such a forced system is often utilized to study the properties of decaying turbulence but an artificial damping term must be added to the Hasegawa-Mima equation [49]. One approach to include linearly unstable drift waves is to extend the Hasegawa-Mima model by a non-adiabatic electron response, the so-called $i\delta$-models [50; 51; 52].

Similar to the two-dimensional fluid turbulence outlined in Ch. 1 the Hasegawa-Mima equation obeys two conserved quantities, the energy

$$E = \frac{1}{2}\int \phi^2 + (\nabla\phi)^2 \,\mathrm{d}x\,\mathrm{d}y, \tag{2.28}$$

and the enstrophy

$$W = \frac{1}{2}\int (\nabla\phi)^2 + (\nabla^2\phi)^2 \,\mathrm{d}x\,\mathrm{d}y. \tag{2.29}$$

In addition to the linear dynamics of the waves $\phi_{\boldsymbol{k}}(t)$, which is described by the linear dispersion relation, the quadratic nonlinearity of the Hasegawa-Mima equation gives rise to three-wave interaction that alters the wave amplitudes $\phi_{\boldsymbol{k}}(t)$ in time. In Fourier representation the Hasegawa-Mima equation (2.22) reads

$$\mathrm{d}_t\phi_{\boldsymbol{k}}(t) + i\omega_{\boldsymbol{k}}\phi_{\boldsymbol{k}}(t) = \sum_{\boldsymbol{k}'+\boldsymbol{k}''-\boldsymbol{k}=0} \Lambda^{-\boldsymbol{k}}_{\boldsymbol{k}',\boldsymbol{k}''}(\boldsymbol{k}''^2 - \boldsymbol{k}'^2)\phi'_{\boldsymbol{k}}(t)\phi''_{\boldsymbol{k}}(t), \tag{2.30}$$

with the coupling coefficient

$$\Lambda^{-\boldsymbol{k}}_{\boldsymbol{k}',\boldsymbol{k}''} = \frac{1}{2}\frac{(\boldsymbol{k}'\times\boldsymbol{k}'')\cdot\hat{\boldsymbol{z}}}{(1+\boldsymbol{k}^2)}. \tag{2.31}$$

In physical terms, the latter equation describes the interaction of three Fourier modes or waves $\phi_{\boldsymbol{k}}(t)$, i.e. the beating of two modes $(\boldsymbol{k}', \boldsymbol{k}'')$ into a third one $(\boldsymbol{k})$ obeying the summation rule $\boldsymbol{k}' + \boldsymbol{k}'' - \boldsymbol{k} = 0$.
The strength of the interaction is determined by the coupling coefficient Λ. With energy and enstrophy as conserved quantities it can be shown that in the three-wave interaction the enstrophy is transported to the modes with higher wavenumbers while the energy is transferred to the lower wavenumbers, Fjortoft's theorem in Ref. [53]. This is the inverse or dual cascade that has been already discussed in Ch. 1 for two-dimensional fluid turbulence.

2.4 Hasegawa-Wakatani model

In contrast to the Hasegawa-Mima equation discussed in the foregoing section the Hasegawa-Wakatani model is a self-consistent description of drift-wave turbulence. The three-dimensional Hasegawa-Wakatani model is a set of two coupled equations for density and potential fluctuations for a homogeneous magnetic field that reduces in the adiabatic (collisionless) limit to the two-dimensional Hasegawa-Mima equation if the parallel gradients are kept fixed. In the following section a brief derivation of the Hasegawa-Wakatani equation from a closed three-field model for density, vorticity and parallel current is given.

Vorticity equation: From the quasi-neutrality condition $\nabla \cdot \boldsymbol{J} = 0$ an equation for the vorticity is easily obtained by inserting the perpendicular drift velocities. It was already emphasized (cf. Sec. 2.2) that there is no current associated with the $\boldsymbol{E}\times\boldsymbol{B}$-drift and that the contribution of the diamagnetic current vanishes in geometries with straight magnetic field lines. Thus the only contribution to the perpendicular current is the ion polarization current $\boldsymbol{J}_{pi} = en\boldsymbol{v}_{pi}$ with

$$0 = -\nabla_\parallel \cdot J_\parallel - \nabla_\perp \cdot \boldsymbol{J}_{pi}, \tag{2.32}$$

which yields

$$\nabla_\perp \cdot \frac{nM}{B^2} \mathrm{d}_t \nabla_\perp \phi = \nabla_\parallel J_\parallel. \tag{2.33}$$

The latter equation can be simplified by taking the drift-ordering into account

$$\frac{\omega}{\Omega_{ci}} \sim \frac{k_\parallel}{k_\perp} \sim \frac{\tilde{n}}{n_0} \sim \frac{\rho_s}{L_\perp} \sim \delta << 1, \tag{2.34}$$

where δ is a smallness parameter. A consequence of the drift ordering can be illustrated by use of the operator $\nabla_\perp$. The operation of $\nabla_\perp$ on a fluctuating quantity carries the scale ρ_s while the operation of $\nabla_\perp$ on a background quantity carries the scale $L_\perp$. According to this, the operation of $\nabla_\perp$ on a fluctuating quantity and background quantity is the same:

$$\nabla_\perp \tilde{n} \sim \frac{\tilde{n}}{\rho_s} \sim \frac{n_0}{L_\perp} \sim \nabla n_0. \tag{2.35}$$

In contrast, operation of higher orders of $\nabla_\perp$ yields

$$\nabla_\perp^2 \tilde{n} \sim \frac{\tilde{n}}{\rho_s^2} \sim \frac{n_0}{\rho_s L_\perp} >> \frac{n_0}{L_\perp^2} \sim \nabla_\perp^2 n_0. \tag{2.36}$$

Applying the drift-ordering, the vorticity equation (2.33) can be written as

$$\frac{nM}{B^2}\mathrm{d}_t\nabla_\perp^2\phi = \nabla_\parallel J_\parallel. \tag{2.37}$$

Parallel Dynamics: An equation for the parallel current can be derived from Ohm's law. It connects the parallel current and parallel forces. Within the present thesis electromagnetic effects can be neglected since the plasma-β obeys (cf. Sec. 4.1)

$$\beta = \frac{k_B nT}{B^2/2\mu_0} < 2k_\perp^2\rho_s^2\frac{m}{M}\frac{\nu_e}{\omega}. \tag{2.38}$$

Thus, the generalized Ohm's law simplifies to [54]

$$J_\parallel = -\frac{T_\mathrm{e}}{e\eta}\nabla_\parallel\left(\frac{e\phi}{T_\mathrm{e}} - \ln n\right), \tag{2.39}$$

which couples to the vorticity equation by the term $\nabla_\parallel J_\parallel$. Here, $\eta = m\nu_e/2e^2n$ is the plasma resistivity.

Continuity equation: To close the system an equation for the density is needed. It can be obtained from the electron continuity equation, which can be written as

$$\partial_t n = -\nabla_\perp(nv_\perp) + \nabla_\parallel\frac{J_\parallel}{e}, \tag{2.40}$$

or using the convective derivative

$$\mathrm{d}_t n = \nabla_\parallel\frac{J_\parallel}{e}. \tag{2.41}$$

With the latter equations a closed three-field model of plasma density, vorticity and parallel current is obtained. The parallel current couples the density perturbation to a potential perturbation, while the potential perturbation is determined by the ion polarization current perpendicular to the magnetic field that is balanced by the parallel electron current to ensure quasi-neutrality. Combining the coupled equations (2.37), (2.39) and (2.41) the closed three field model can be reduced to two equations

$$\mathrm{d}_t n = \frac{1.96}{m\nu_e}\nabla_\parallel^2(nT - en\phi) \tag{2.42}$$

$$\frac{nM}{B^2}\mathrm{d}_t\nabla_\perp^2\phi = \frac{1.96e}{m\nu_e}\nabla_\parallel^2(nT - en\phi). \tag{2.43}$$

Normalizing the latter equations yields the three-dimensional Hasegawa-Wakatani equa-

tions [43]

$$\partial_t n + \{n, \phi\} + \kappa_n \partial_y \phi = \frac{1}{\nu} \nabla_\parallel^2 (n - \phi), \tag{2.44}$$

$$\partial_t \nabla_\perp^2 \phi + \{\phi, \nabla_\perp^2 \phi\} = \frac{1}{\nu} \nabla_\parallel^2 (n - \phi), \tag{2.45}$$

where $\nu = 1.96\Omega_{ce}/\nu_e$ and $\kappa_n = -\partial_x \ln n_0(x)$. Due to the anisotropy of the magnetic field, the scale separation $k_\parallel << k_\perp$ motivates one to reduce the three-dimensional system to a 2D plane perpendicular to the magnetic field. This can be done by replacing the parallel derivative $\nabla_\parallel$ with the characteristic parallel scale length $k_\parallel$. With the approximation $\nabla_\parallel^2 \longrightarrow -k_\parallel^2$ the two-dimensional Hasegawa-Wakatani equations read

$$\partial_t n + \{n, \phi\} + \kappa_n \partial_y \phi = C(\phi - n), \tag{2.46}$$

$$\partial_t \nabla_\perp^2 \phi + \{\phi, \nabla_\perp^2 \phi\} = C(\phi - n), \tag{2.47}$$

with $C = k_\parallel^2/\nu$. Often the Hasegawa-Wakatani equations are extended to include also ion viscosity that arises from the collisional part $\mathbf{\Pi}^{coll}$ of the anisotropic stress tensor $\mathbf{\Pi}$ in (2.3). In the limit $\Omega_{ci}^2/\nu_{ii}^2 >> 1$ it can be written as [47]

$$\nabla_\perp \cdot \mathbf{\Pi}^{coll} = -\mu_i \nabla_\perp^2 \boldsymbol{v}, \tag{2.48}$$

with the ion viscosity $\mu_i = nT_\mathrm{i}\nu_{ii}/(4\Omega_{ci})$. Retaining the ion viscosity in the derivation of the ion polarization drift yields

$$\boldsymbol{v}_p = -\frac{M}{eB^2} \left(\partial_t + \boldsymbol{v}_{E\times B} \cdot \nabla_\perp - \mu_i \nabla_\perp^2\right) \nabla_\perp \phi. \tag{2.49}$$

Thus, an additional term appears in the Hasegawa-Wakatani equations that arises from ion viscosity,

$$\partial_t n + \{n, \phi\} + \kappa_n \partial_y \phi = C(\phi - n), \tag{2.50}$$

$$\partial_t \nabla_\perp^2 \phi + \{\nabla_\perp^2 \phi, \phi\} = C(\phi - n) + \mu \nabla_\perp^4 \phi. \tag{2.51}$$

Here the ion viscosity was normalized to $\mu = \mu_i/(\rho_s^2 \Omega_{ci})$. In the dissipation-less limit, the Hasegawa-Mima equation (2.22) is recovered for adiabatic electron response $n = \phi$. The dispersion relation for resistive drift waves is obtained from (2.50) and (2.51) assuming plane wave solutions [55]:

$$\omega^2 + i\omega(b + \mu k_\perp^2) - ib\frac{k_y \kappa_n}{1 + k_\perp^2} - \frac{k_\perp^4}{1 + k_\perp^2} \mu b = 0, \tag{2.52}$$

where $b = C(1 + k_\perp^2)/k_\perp^2$. In the limit $C \gg \omega$ and $\mu \ll \omega$ the solution reads

$$\boxed{\omega = \frac{\omega^\star}{1 + k_\perp^2} + i\left(\frac{\omega^{\star^2} k_\perp^2}{(1 + k_\perp^2)C} - \frac{\mu k_\perp^4}{1 + k_\perp^2}\right) = \omega_R + i\gamma.} \tag{2.53}$$

From the latter equation it is clear that for a drift-wave instability a background density gradient is necessary that provides the energy for the growth of the fluctuations. Finite resistivity ($\nu \sim 1/C$) acts destabilizing while the ion resistivity acts stabilizing. The influence of the magnetic field on the growth rate is hidden in the normalized equation since $k^2 \to \rho_s^2 k^2$.

Numerical simulations based on the Hasegawa-Wakatani model reveal that the energy spectrum scales as $E \sim k^{-3}$ for large wavenumbers as expected from the 2D Kolmogorov theory [43; 56], although the scaling exponent can be strongly altered by the presence of coherent structures. In contrast to the Hasegawa-Mima model, the Hasegawa-Wakatani model allows for transport, where the particle flux $\mathbf{\Gamma}$ in $\hat{\boldsymbol{x}}$-direction is given by

$$\Gamma_x = -\frac{1}{B} \langle n \partial_y \phi \rangle \,. \tag{2.54}$$

2.5 Model of the CYTO code

Common nonlinear drift-wave turbulence models, Hasegawa-Mima and Hasegawa-Wakatani models, are based on a separation between background quantities and fluctuating quantities. The background density profile is not affected by the fluctuating quantities, e.g. due to a perpendicular particle flux. This approach is also known as local approximation. Within the present thesis the experimental results are compared with fully nonlinear numerical simulations of drift-wave turbulence using the CYTO code [57]. The numerical model of the code, outlined in this section, will reduce to the well-known Hasegawa-Wakatani model in the limit of small fluctuation amplitude and scale separation between background and fluctuating quantities.

The main difference between the Hasegawa-Wakatani model and the numerical model of the CYTO code, except for its global character, is that the parallel velocities of electrons and ions are not replaced by currents. The global character becomes obvious in the vorticity equation, where the drift-approximation is not applied (cf. Sec. 2.4). Thus, the

modified vorticity equation reads

$$\nabla_\perp \cdot \left(\frac{nM}{eB^2} \mathrm{d}_t \nabla_\perp \phi \right) = \mu_i \nabla_\perp \cdot \frac{nM}{eB^2} \nabla_\perp^2 \nabla_\perp \phi - \nabla_\perp \frac{nM}{eB^2} \nu_{in} \nabla_\perp \phi + \nabla_\parallel n (U - V), \quad (2.55)$$

where $U = \boldsymbol{v}_{i,\parallel}$ is the parallel ion velocity and $V = \boldsymbol{v}_{e,\parallel}$ is the parallel electron velocity. The second term on the right hand side arises from the Pedersen current [58], which accounts for a polarizing ion current due to friction forces between ion and neutrals in low-temperature plasmas (ν_{in} denotes the ion-neutral collision frequency). An equation for the parallel electron and ion velocity is derived from the parallel momentum equation (2.3) in the electrostatic limit, where thermal forces are neglected and the ions are assumed to be cold

$$\begin{aligned} \mathrm{d}_t V &= \frac{e}{m} \nabla_\parallel \phi - \frac{T}{m} \nabla_\parallel \ln n - \nu_{ei}(V - U) - \nu_{en} V & (2.56) \\ \mathrm{d}_t U &= -\frac{e}{M} \nabla_\parallel \phi - \nu_{ie}(U - V) - \nu_{in} V. & (2.57) \end{aligned}$$

Similar to the Hasegawa-Wakatani model, the continuity equation closes the system. Scaling of the set of equations, where masses are normalized to the electron mass, yields

$$\begin{aligned} \nabla N \cdot \mathrm{d}_t \nabla_\perp \phi \, \mathrm{d}_t \nabla_\perp^2 \phi &= \nabla_\perp N \cdot (\mu \nabla_\perp (\nabla_\perp^2 \phi) - \nu_{in} \nabla_\perp^2 \phi) & (2.58) \\ &\quad -\nu_{in} \nabla_\perp^2 \phi + \nabla_\parallel (U - V) + (U - V) \nabla_\parallel n + \mu \nabla_\perp^4 \phi \\ \mathrm{d}_t N &= -(V \nabla_\parallel N + \nabla_\parallel V) + \mu_n (\nabla_\perp^2 N + (\nabla N)^2) & (2.59) \\ \mathrm{d}_t U &= -\nabla_\parallel \phi - \nu_{in} U - \nu_\parallel (V - U) & (2.60) \\ \mathrm{d}_t V &= M \nabla_\parallel (\phi - N) - M \nu_{en} V - \nabla_\parallel (V - U), & (2.61) \end{aligned}$$

where $\nu_\parallel = \nu_{ei} m / M \Omega_{ci} = \nu_{ie} / \Omega_{ci}$ and $N = \ln n$. Note that for numerical stabilization of the scheme an additional viscous damping term is added to the density equation. Physical input parameter of the code are the source density profile

$$S \sim \exp\left(-(r\kappa_n)^2\right) \cdot \exp\left(-z^2\right), \quad (2.62)$$

where $\kappa_n = |\partial_r \ln n_0|$, and the collisionalities, which are assumed to be constant across the plasma profile. At the end plate of the device the density is assumed to have vanishing parallel derivative, and the parallel boundary conditions of the potential and velocity is determined by sheath boundary conditions [59]. The typical plasma parameters for the

experimental results obtained in VINETA (cf. Sec. 4.1) transform into normalized input parameters for the code as compiled in Tab. 2.1.

normalized input parameter	range
density gradient length κ_n^{-1} $[\rho_s]$	0.5 - 5
Coulomb collisions $\nu_\parallel$ $[\Omega_{ci}]$	2 - 500
ion-neutral collisions ν_{in} $[\Omega_{ci}]$	0.03 - 0.25
electron-neutral collisions ν_{en} $[\Omega_{ci}]$	2 - 28
ion viscosity μ $[10^{-2}\,\Omega_{ci}]$	0.04 - 1

Table 2.1: Normalized input parameters for the CYTO code.

2.5.1 Linear properties

The linear properties of the CYTO model for vanishing parallel ion velocity U, negligible electron inertia and collisions with neutrals can directly be compared to the Hasegawa-Wakatani dispersion relation. To account for a stationary and homogeneous parallel electron current V_0, as it occurs in many laboratory discharges, V is substituted by $V + V_0$. In a local rectangular coordinate system (local slab model) the density gradient points in the $-\hat{\boldsymbol{x}}$-direction and any background potential profile ϕ_0 is neglected. Assuming harmonic perturbations of the form

$$V, \phi, n \sim \exp\left(-i\omega t + ik_y y + ik_\parallel z\right) \tag{2.63}$$

and neglecting higher order terms yields the linearized form of equations (2.58) and (2.59)

$$\begin{aligned} i\omega k_y^2 \phi &= \mu k_y^4 \phi + \tau k_\parallel^2 (\phi - n) - iV_0 k_\parallel n + \nu_{in} k_y^2 \phi & (2.64)\\ -i\omega n &= -i\omega^\star + \tau k_\parallel^2 (\phi - n) - iV_0 k_\parallel n, & (2.65) \end{aligned}$$

where $\tau = M/\nu_{en}$. Substituting $\omega_1 = V_0 k_\parallel$, $b = k_y^2$ and $\tau_e = \tau k_\parallel^2$ the latter equations can be combined to a quadratic dispersion relation

$$\begin{aligned} &b\omega^2 + \omega(i\tau_e(1+b) + ib(\nu_{in} + \mu b) - \omega_1 b) \qquad (2.66)\\ &-\tau_e(i\omega^\star + b(\nu_{in} + \mu b)) + \omega_1(\omega^\star - ib(\nu_{in} + \mu b)) = 0. \end{aligned}$$

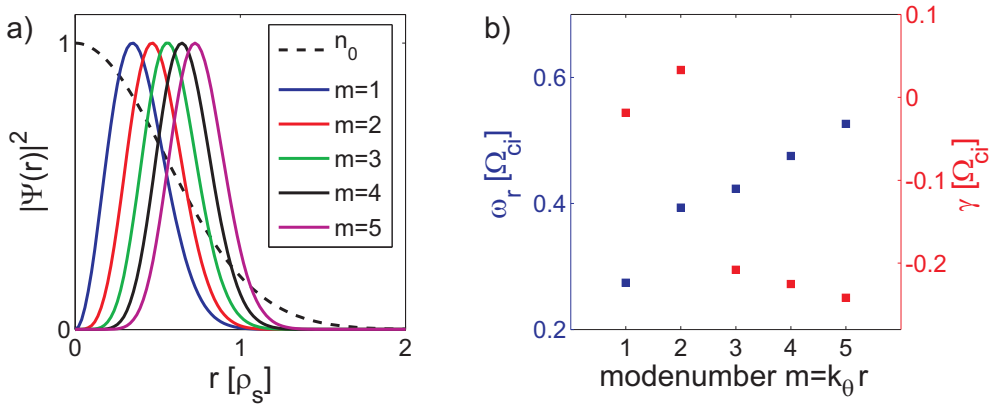

Figure 2.2: Eigenfunctions $|\psi(r)|^2$ (a) and eigenfrequencies ω_R and growth rates γ (b) for a Gaussian density profile and typical VINETA plasma parameters.

In the limit $\omega, \omega_1, \omega^\star << \tau_e$ the latter equation can be solved for $\omega = \omega_R + i\gamma$

$$\omega_R = \frac{\omega^\star}{1+b} \tag{2.67}$$

$$\gamma = \frac{\omega^\star}{\tau_e(1+b)}\left(\frac{b\omega^\star}{(1+b)^2} + \omega_1\right) - \frac{b}{1+b}(\nu_{in} + \mu b). \tag{2.68}$$

Similar to the drift wave dispersion obtained from the Hasegawa-Wakatani equations, the growth rate of the drift-wave instability is strongly affected by collisions. Electron-neutral collisions act destabilizing and amplify the perturbation, while ion-neutral collisions and ion viscosity act stabilizing. It is worthwhile to note that ion-neutral collisions damp all wavenumbers k_y while the ion viscosity preferentially damps high k_y modes. In the adiabatic limit, where the parallel electron flow is not impeded by collisions ($\tau_e \longrightarrow \infty$) the drift wave is linearly stable. An equivalent dispersion relation for this local slab model was derived by Ellis *et al.* [60].

Ellis *et al.* [60] also developed a non-local cylindrical model that is more comprehensive since background profiles of plasma density $n_0(r)$ and plasma potential $\phi_0(r)$ are explicitly considered. The set of equations derived in the non-local cylindrical model can be reduced to a set of first order differential equations that can be solved by Runge-Kutta shooting algorithms [61] to find the complex eigenfunctions $\psi(r)$ and eigenvalues $\omega = \omega_R + i\gamma$ [30; 62]. A solution for typical VINETA plasma parameters is shown in Fig. 2.2 for azimuthal modenumbers $m = k_\theta r = 1 - 5$ (k_θ is the azimuthal wavenumber). The drift-wave modes are located in the maximum plasma density gradient (Fig 2.2a) with frequencies $\omega_r \lesssim \Omega_{ci}/2$ (Fig. 2.2b). The growth rate is positive only for the $m = 2$ drift mode. All other modenumbers are damped. For a detailed discussion about the influence of parameters as collisionality and parallel wavenumber on the dispersion relation, the reader is referred to Ref. [30; 62].

2.5.2 Nonlinear properties

An important property of the global CYTO model is that it allows the coherent drift-wave modes to develop their nonlinearly saturated phase. Such a situation has not been yet reported for numerical simulations based on the Hasegawa-Wakatani model, in which drift-wave turbulence is observed predominantly. Nevertheless in numerical simulations performed with the CYTO code a transition from coherent drift-wave mode regimes to drift-wave turbulence is also observed, depending on the input parameters as collisionality or magnetic field strength.

In Fig. 2.3 a typical result of the numerical solution for two different input parameter sets is depicted. Shown are the density fluctuations in the azimuthal (x, y)-plane for a coherent drift-wave mode (Fig.. 2.3a) and weakly developed drift-wave turbulence (Fig. 2.3b). For the result shown in Fig. 2.3a the input parameters are $\kappa_n = 0.77$, $\nu_{in} = 0.075$ and $\mu = 0.005$, while for the turbulent situation shown in Fig. 2.3b $\kappa_n = 1.4$, $\nu_{in} = 0.05$ and $\mu = 0.001$. All other input parameters are identical. In other words, in the weakly developed drift-wave turbulence situation the drive of the drift mode is enhanced, the profile is steeper, and the stabilizing influence of ion-neutral collisions and ion dissipation in the

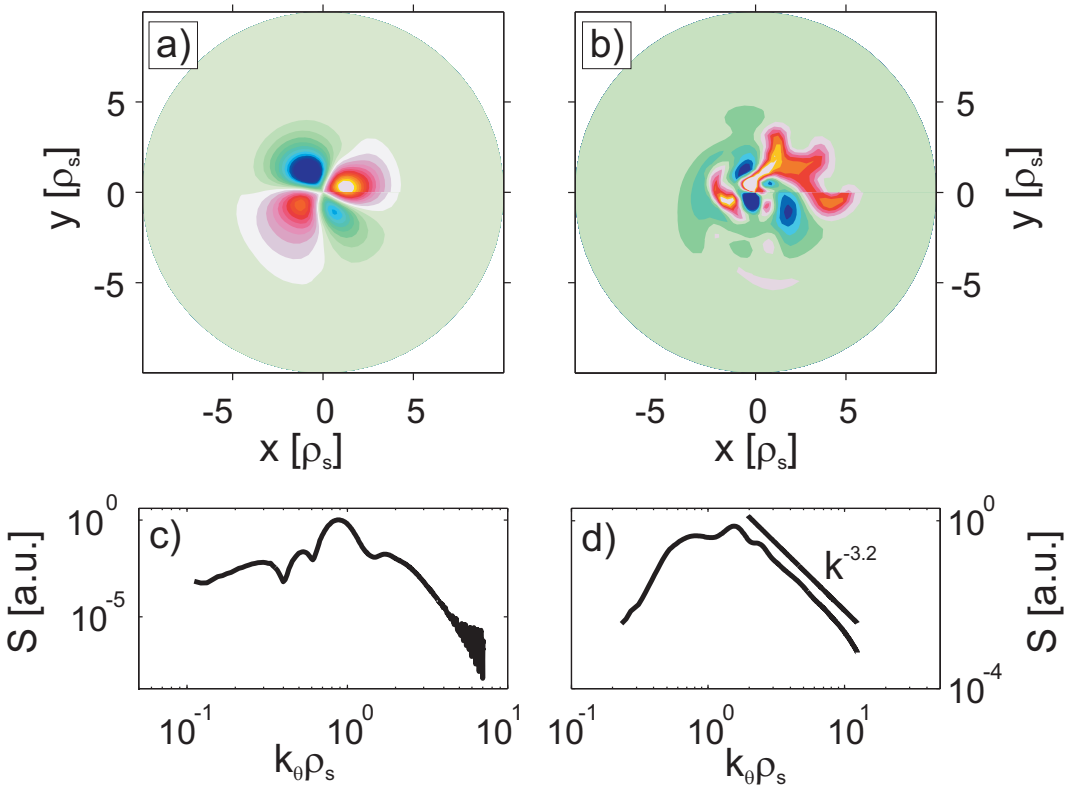

Figure 2.3: Density fluctuations in the azimuthal plane and corresponding azimuthal wavenumber spectrum: (a,c) for a coherent drift-wave mode and (b,d) for weakly developed drift-wave turbulence.

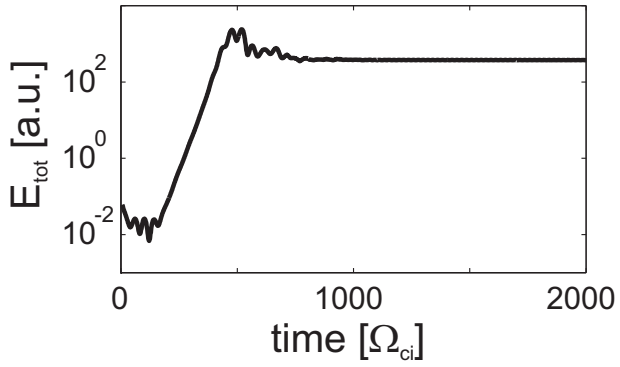

Figure 2.4: Time evolution of the total fluctuation energy for simulation of Fig. 2.3a.

linear growth rate (2.68) is reduced. In Fig. 2.3a a single coherent drift-wave mode with modenumber $m = 2$ is observed while in Fig. 2.3b the weakly developed turbulent state is characterized by a broadened modenumber spectrum with several interacting drift-wave modes. Note that both results are obtained in the nonlinearly saturated phase. The time trace of the total fluctuation energy $E = \int \tilde{n}^2 + |\nabla\tilde{\phi}|^2 \,\mathrm{d}\, x^2$ for the drift-wave mode situation (Fig. 2.3a) is shown in Fig. 2.4. In the linear phase the energy increases exponentially in time and saturates at $t \approx 800\,\Omega_{ci}$.

Figs. 2.3c and 2.3d show the time-averaged wavenumber spectra for both situations. The wavenumber spectra of the coherent drift-wave mode peaks at the azimuthal wavenumber k_θ that corresponds to the $m = 2$ mode. For higher wavenumbers a power-law decay is observed. In comparison the wavenumber spectra of weakly-developed turbulence exhibits no distinct peaks but remnants of drift-wave modes can still be observed at small wavenumbers $k_\theta \rho_s \leq 2$. For larger azimuthal wavenumbers a $k_\theta^{-\alpha}$-decay with a spectral exponent of $\alpha = 3.2$ is observed, which is in agreement with the findings of other numerical simulations of drift-wave turbulence based on the Hasegawa-Wakatani model (cf. Sec. 2.4). Why a $m = 2$ mode is observed in the coherent drift-wave mode situation becomes clear by reconsidering the linear dispersion relation. The corresponding frequencies ω_r and growth rates γ for drift-wave modes $m = 1 - 5$ have already been shown in Fig. 2.2 and it was found that only the $m = 2$ mode has a positive growth rate. The evolution of the drift-wave modes in the nonlinearly saturated phase is not controlled by the linear growth rates and a detailed analysis of the nonlinear dynamics requires an estimation of the three-wave coupling coefficient (2.30), which is not trivial.

For a fixed set of collisional input parameters, which are identical with the coherent drift-wave situation shown in Fig. 2.3a, the growth rate of the various drift modes can efficiently be influenced by the density gradient length of the (Gaussian) source profile. The resulting density fluctuations in the azimuthal plane obtained in the nonlinearly saturated phase are shown in Fig. 2.5 for four different (Gaussian) input profiles $S \sim \exp\left(-r^2\kappa_n^2\right)$ with

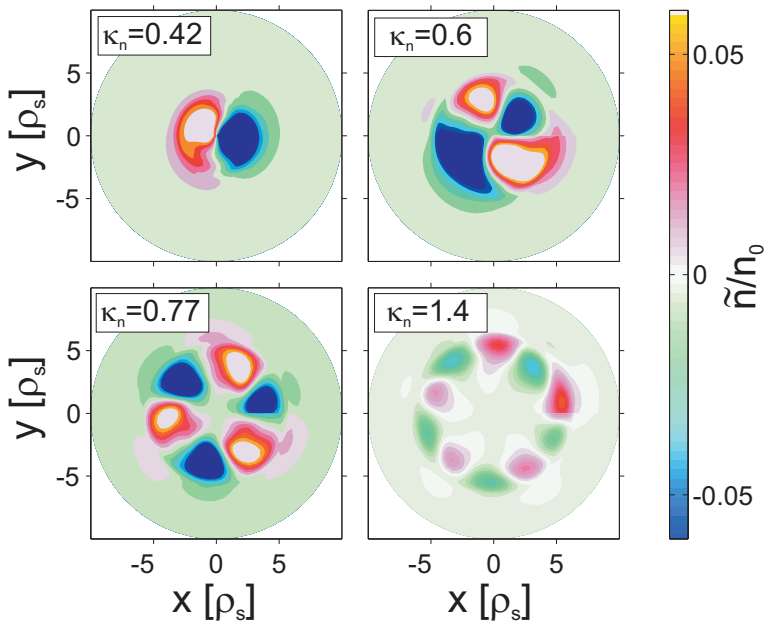

Figure 2.5: Relative fluctuation amplitude of density fluctuations $\tilde{n}/n_0$ in the azimuthal plane for four different widths of the Gaussian source profile $S \sim \exp(-r^2\kappa_n^2)$. All other input parameters are identical with the result shown in Fig. 2.3a.

κ_n varying between 0.42 and 1.4. For a broad source profile with $\kappa_n = 0.42$ the $m = 1$ drift mode has the largest growth rate and thus dominates the dynamics of density fluctuations in the azimuthal plane. If the source profile is steepened (for larger κ_n values) a transition to higher modenumbers $m = 2, 3, 5$ is observed. The relative amplitude of the density fluctuations is $\tilde{n}/n_0 \leq 10\,\%$ which is in agreement with experimental observations in VINETA for coherent drift-wave modes (cf. Sec. 4.3). In physics terms, the width of the source profile is determined by $1/\kappa_n = L_\perp/\rho_s \sim B$, where the magnetic field enters via the drift scale ρ_s. Thus, for an increasing magnetic field at constant density gradient length and constant collisionality higher modenumbers are observed, which is in agreement with experimental observations in VINETA [30; 31].

In conclusion, the CYTO code is able to describe the fluctuation dynamics for two different situations, coherent drift modes and weakly-developed drift-wave turbulence. According to the results presented later in Sec. 4.4 this is in agreement with experimental observations in VINETA, where both situations are observed as well. In the situation of coherent drift modes the fluctuation dynamics is solely determined by a single drift mode, which has the largest linear growth rate. All other modes are highly damped. The transition to the weakly-developed turbulent state is governed by the density gradient drive κ_n, ion viscosity μ, and ion-neutral collision rate ν_{in}. At low ion viscosity the growth rate (2.68) of the various drift modes is enhanced, which leads to nonlinear interaction of the drift modes. Since μ and ν_{in} are normalized to the ion cyclotron frequency Ω_{ci}, the

nonlinear interaction occurs predominantly at higher magnetic fields, which is consistent with the experimental findings presented in Sec. 4.4.
In Chap. 6 the numerical results of the CYTO code in weakly developed drift-wave turbulence are investigated in detail. Special attention is paid to the formation and propagation of turbulent structures.

3

Plasma diagnostics and signal processing

The main subject of the present thesis is the spatiotemporal analysis of fluctuating plasma parameters, in particular plasma density and plasma potential. In low-temperature plasmas the main diagnostic tool is the electrostatic Langmuir probe, which can either be used to measure time-averaged or fluctuating plasma parameters. The great advantage of this diagnostic is that it allows for high temporal resolution and, if arranged on arrays, also for a reasonable spatial resolution. However, it is an invasive technique that imposes a certain disturbance to the plasma. The Langmuir probe diagnostics that are used for the measurements presented in this thesis are described in Sec. 3.1.1.
The measurements discussed in Ch. 7 are obtained in a high-temperature fusion device, where Langmuir probes are not applicable, mainly due to the high heat load. In such devices, spatiotemporal fluctuations can be measured with optical techniques as gas puff imaging, which is described in detail in Sec. 3.1.4.
To characterize the fluctuating quantities several signal-processing tools as probability distribution functions, cross-correlation and conditional-averaging techniques, Fourier and wavelet decomposition or bicoherence analysis are utilized. They are briefly reviewed in Sec. 3.2.

3.1 Plasma diagnostics

3.1.1 Electrostatic probes

Langmuir discovered in 1923 that important plasma parameters as plasma density n, plasma potential ϕ, and electron temperature T_e can be measured with electrostatic probes, which are in principle small electrodes exposed to the plasma. The Langmuir probes used in this thesis have cylindrical geometry. They consist of a tungsten wire immersed in a ceramic tube to shield the probe electrically from the plasma, except for the probe tip. Typical dimensions of the probe tips are radius $r_p = 0.1\,\text{mm}$ and length $l_p = 3\,\text{mm}$. The insulating ceramic has a diameter of $0.6\,\text{mm}$ only to minimize the perturbations of the

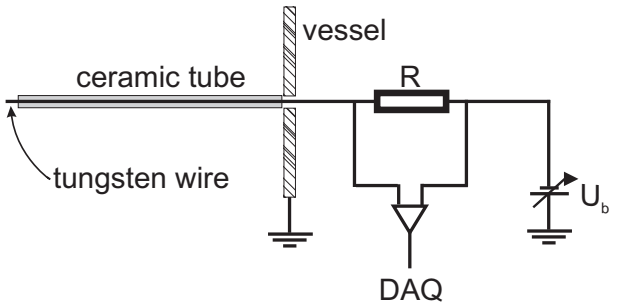

Figure 3.1: Typical setup for the measurement of the *IU*-characteristic with a cylindrical Langmuir probe.

plasma by the probe. Time-averaged plasma parameters are obtained from the current-voltage (*IU*) characteristic of the probe. A typical setup for measuring a *IU*-characteristic with a cylindrical probe is shown in Fig. 3.1. The probe is biased with a variable voltage and the probe current is digitally recorded as the voltage drop over a shunt resistor R. An example of the so-obtained *IU*-characteristic is shown in Fig. 3.2. It splits into three different regions, which are separated from each other by the floating potential ϕ_f and the plasma potential ϕ_p. At large negative voltages applied to the probe ($U_b \ll \phi_p$) all electrons are repelled and the current to the probe is determined solely by the ion flux. This branch of the *IU*-characteristic is called ion saturation region. For a less negative voltage relative to the plasma potential, the most energetic electrons are able to overcome the retarding electric field of the probe. The electron current contribution decreases the measured net probe current. If the applied voltage reaches the floating potential the ion current to the probe is balanced by the electron current (ambipolar flux) and the measured probe current is zero. In the transition region between the floating potential ϕ_f and the plasma potential ϕ_p the probe attracts increasingly more electrons. For a Maxwellian electron energy distribution function (EEDF) the electron current contribution to the *IU*-characteristic in the transition region is exponential. For probe voltages larger than the plasma potential ($U_b \gg \phi_p$) the electron current is independent of the electron energy. This is called the electron saturation region. For cylindrical probes, the electron current to the probe increases monotonically in the electron saturation regime as the sheath thickness around the probe increases with the applied voltage [63].

There is a vast number of probe theories to extract the plasma parameters from a *IU*-characteristic and they depend on the geometry of the probe as well as on the plasma parameters, especially collisionality and magnetic field. Langmuir's [64] basic ideas of a probe in a unmagnetized collisionless plasma are the following: The ion saturation current $I_{sat,i}$ is determined by the Bohm-criterion, which states that the ions are accelerated to the ion sound speed c_s in the pre-sheath of the probe. The resulting ion current to the

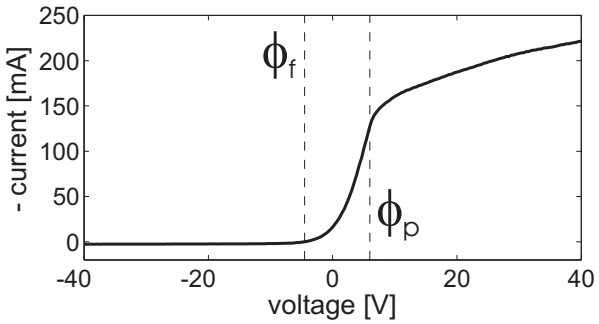

Figure 3.2: Measured current-voltage (*IU*) characteristic for a cylindrical Langmuir probe. The floating potential ϕ_f and the plasma potential ϕ_p are indicated as dashed lines.

probe reads

$$I_{sat,i} = eAnc_s = wneA\sqrt{k_{\mathrm{B}}T_{\mathrm{e}}/M}, \tag{3.1}$$

where M is the ion mass, A is the surface of the probe and w is a factor that accounts for the plasma density depletion in the pre-sheath ($w = 0.61$). At the plasma potential the electron saturation current $I_{sat,e}$ is given by

$$I_{sat,e} = -enA\bar{v}_e/4 = -neA\sqrt{k_{\mathrm{B}}T_{\mathrm{e}}/(2\pi em)}, \tag{3.2}$$

where m denotes the electron mass, $\bar{v}_e = \sqrt{8k_{\mathrm{B}}T_{\mathrm{e}}/\pi m}$ is the average electron velocity (averaged over a Maxwellian EEDF) and the factor $1/4$ arises from the estimation of the electron flux to the probe, $\Gamma_e = n\bar{v}_e/4$. In the limit $T_i << T_e$ the ratio of the ion and electron saturation currents is determined solely by the mass ratio, $I_{sat,i}/I_{sat,e} \sim \sqrt{m/M}$. Assuming a Maxwellian EEDF the electron current in the transition region reads

$$I_e = I_{sat,e}\ \exp\left(\frac{e(V-\phi_p)}{k_B T_e}\right). \tag{3.3}$$

The balance of ion and electron currents for a floating probe relates the floating potential ϕ_f to the plasma potential ϕ_p,

$$\phi_p = T_{\mathrm{e}}\ln\left(\frac{\bar{v}_e}{4c_s}\right) + \phi_f = \ln\left(\frac{M}{2\pi m_e}\right)^{1/2} T_{\mathrm{e}} + \phi_f = \alpha T_{\mathrm{e}} + \phi_f, \tag{3.4}$$

where $\alpha = 4.6$ for Argon [63]. The plasma potential ϕ_p is usually determined from the minimum of the first derivative $\mathrm{d}I/\mathrm{d}U$. The exponential slope of the *IU*-characteristic in the transition region yields the electron temperature. With the knowledge of the electron temperature the plasma density can be obtained from the ion saturation current (3.1).

The original theory of Langmuir is only applicable in the limit of small collisional-

regime	condition
collisionless	$\lambda_e \gg d + h$
non-local	$\lambda_\epsilon \gg d + h \gg \lambda_e$
hydrodynamic	$d + h \gg \lambda_\epsilon$

Table 3.1: Regimes of applicable probe theories for an unmagnetized plasma, where d is the probe dimension, h the sheath thickness, λ_e the electron mean-free path and λ_ϵ the energy relaxation length.

ity, where the sum of probe dimension d and thickness of the sheath around the probe $h \sim \lambda_{\mathrm{Debye}}$ is much smaller than the electron collisional mean-free path $\lambda_e = v_{th,e}/\nu_{ee}$, where λ_{Debye} is the Debye-length, $v_{th,e}$ is the thermal velocity of the electrons, and ν_{ee} is the Coulomb collision frequency for electron-electron collisions. Probe theories for highly collisional regimes with $d + h >> \lambda_e$ have been developed, which are also known as non-local and hydrodynamic approximation [65]. The validity of these approximations is determined by the energy relaxation length λ_ϵ, the spatial scale on which energy is dissipated. The different regimes are compiled in Tab. 3.1. According to Ref. [65] the non-local approximation is valid in plasma regimes where Coulomb collisions dominate over electron-neutral collisions, $\nu_{ee} >> \nu_{en}$, while in partially ionized plasmas the hydrodynamic approximation is valid since electron-neutral collisions strongly minimize the energy relaxation length and $d + h \gg \lambda_\epsilon$ holds.

The situation gets more complex if a magnetic field is taken into account. It imposes an anisotropic motion of the electrons and the ions. Recently, a non-local kinetic probe theory for strongly magnetized plasmas has been developed [66]. Due to the anisotropy perpendicular and parallel to the ambient magnetic field the first derivative of the probe current density $\mathrm{d}j/\mathrm{d}U$ yields the EEDF. For a cylindrical probe orientated perpendicular to the ambient magnetic field one obtains

$$\frac{\mathrm{d}j_e}{\mathrm{d}V} = -\frac{8\pi e^3 \rho_e U}{3m^2 r_p \ln \pi l_p/(4r_p)} \cdot f(W), \tag{3.5}$$

where $U = U_b - \phi_p$ and W is the electron energy in eV, ρ_e is the electron Larmor radius, and r_p and l_p are the the radius length of the probe tip, respectively. Assuming a Maxwellian EEDF

$$f(W) = n \left(\frac{m}{2\pi}\right)^{3/2} \exp\left(\frac{-W}{T_{e,[eV]}}\right) \tag{3.6}$$

the first derivative of the probe current can be fitted with the free parameters electron temperature T_e, plasma density n, and plasma potential ϕ_p.

To take collisionality and the magnetic field in the evaluation of the *IU*-characteristic into

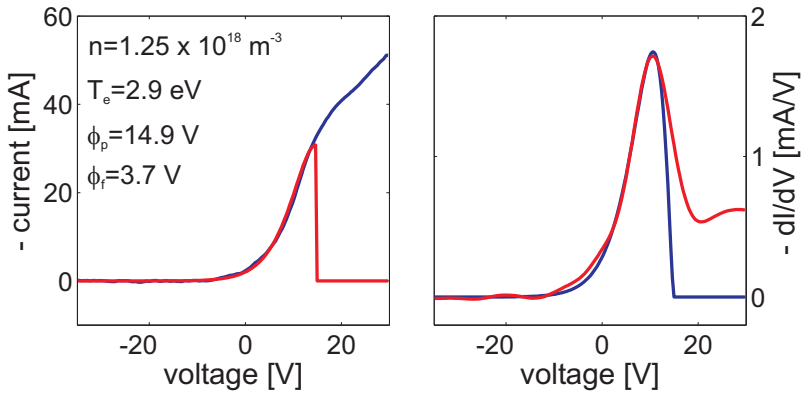

Figure 3.3: Results of the kinetic *IU*-characteristic fit; (a) measured *IU*-characteristic (blue) and modeled *IU*-characteristic (red). (b) First derivative of the probe current $\mathrm{d}I/\mathrm{d}U$ (blue) and fitted derivative (red).

account the kinetic approach is used for our measurements. An example of the probe evaluation is shown in Fig. 3.3.

For *rf*-driven discharges, the *rf*-potential oscillations driven by the plasma source strongly affect the probe sheath, thereby modifying the probe *IU*-characteristic and leading to an overestimation of the electron temperature [67]. Several *rf*-compensation schemes have been proposed [68]. A typical design of such a *rf*-compensated probe is shown in Fig. 3.4. An additional floating electrode, which is capacitively coupled to the probe tip follows the *rf*-driven oscillations and thereby re-adjusts the probe current with respect to the *rf*-voltage oscillations. As an additional measure, *rf*-chokes are used to suppress the *rf*-oscillations.

The fast measurement of *IU*-characteristics to analyze the fluctuations of the plasma density, potential and electron temperature is technically challenging since the sweep of the probe voltage has to be much faster than the typical time scale of the fluctuations [69]. However, if electron temperature fluctuations are assumed to be small ($\tilde{T}_e/T_e \ll \tilde{n}/n$) one may consider the fluctuations of the ion saturation current as a measure of plasma density fluctuations, $\tilde{I}_{sat,i} \sim \tilde{n}$. Under this assumption the plasma potential fluctuations can be approximated by the floating potential fluctuations, $\tilde{\phi}_p \sim \tilde{\phi}_f$. For the present measurements fluctuations of the plasma density or plasma potential are recorded with 1.25 MHz sampling frequency and 12 bit amplitude resolution. To obtain spatially re-

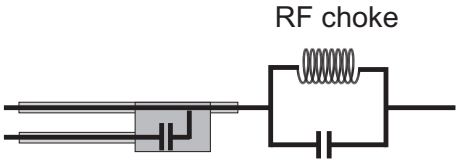

Figure 3.4: Basic principle of a *rf*-compensated probe.

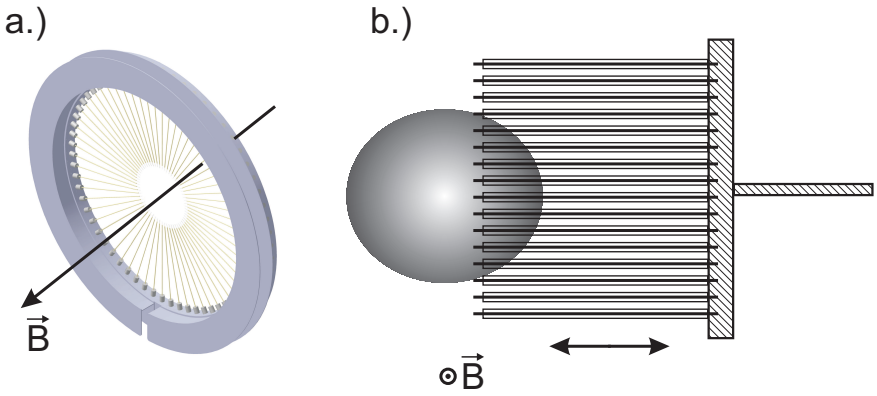

Figure 3.5: (a) Azimuthal probe array (Couronne) made of 64 single Langmuir probes. (b) Vertical probe array with 16 single Langmuir probes mounted on a radial probe positioning system to cover the entire azimuthal plasma cross-section.

solved measurements single Langmuir probes are mounted on probe positioning systems or are arranged as arrays. At VINETA the data acquisition system limits the number of probes to 64. Two different probe arrays are used: The azimuthal probe array Couronne [70] consists of 64 single Langmuir probes (Fig. 3.5a). The radial position of the single probes can be varied but is typically $r_c = 4\,\mathrm{cm}$ which results in a Nyquist wavenumber of $k_{\mathrm{Nyquist}} = 8\,\mathrm{cm}^{-1}$. A second vertical array is made of 16 single Langmuir probes with a spacing of $8\,\mathrm{mm}$ ($\approx \rho_s/2$) and a length of $120\,\mathrm{mm}$ (Fig. 3.5b). The whole array is mounted on a radial position system and can be moved across the radial plasma density profile.

The fluctuation-induced radial particle flux $\tilde{\Gamma} = \tilde{n}\tilde{E}_\theta/B$ (cf. Sec. 5.1) is measured using a triple probe which consists of three azimuthally displaced probe tips oriented perpendicular to the magnetic field (cf. Fig. 3.6). From the potential fluctuations $\tilde{\phi}_1$ and $\tilde{\phi}_2$ measured with the upper and lower probe tip the azimuthal electric field can be calculated as

$$\tilde{E}_\theta = -\nabla_\theta \tilde{\phi} = -\frac{\tilde{\phi}_2 - \tilde{\phi}_1}{\Delta y}, \tag{3.7}$$

where the vertical probe spacing of the probe tips Δy is typically $8 - 22\,\mathrm{mm}$. Together with density fluctuations measured with the middle probe, the radial particle flux $\tilde{\Gamma}$ can be estimated.

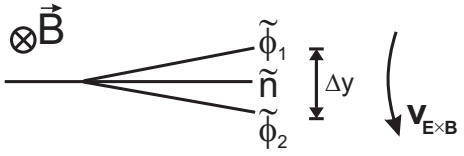

Figure 3.6: A triple probe to measure the fluctuation-induced perpendicular particle flux $\tilde{\Gamma}$.

3.1.2 Microwave interferometer

In contrast to the Langmuir probe, interferometry is a non-invasive diagnostic to measure the absolute line-of-sight integrated plasma density. The principle is based on the comparison of an electromagnetic wave traveling through the plasma with a phase reference. The refractive properties of a plasma act on the phase velocity of the traveling wave and introduce a phase shift with respect to the reference phase. The refractive index is the ratio of the vacuum speed of light and the phase velocity in the plasma. In a magnetized plasma the refractive index for a wave with frequency ω propagating perpendicular to the magnetic field and polarized parallel to the magnetic field (O-mode) is given by [71]

$$N = \frac{kc}{\omega} = \sqrt{1 - \frac{\omega_{pe}^2}{\omega^2}} = \sqrt{1 - \frac{n}{n_{cut}}}, \tag{3.8}$$

where ω_{pe} is the electron plasma frequency. The plasma is only transparent for densities below the cut-off density $n_{cut} = \omega^2 \epsilon_0 m/e^2$. The phase shift is given by

$$\Delta\varphi = \frac{2\pi}{\lambda} \int 1 - \sqrt{1 - \frac{n(l)}{n_{cut}}}\, \mathrm{d}l, \tag{3.9}$$

where λ is the wavelength and l the path length of the wave propagating through the plasma. For a frequency ω much larger than the electron plasma frequency, (3.9) can be approximated as

$$\Delta\varphi = \frac{\pi}{\lambda} \int n(l)\, \mathrm{d}l. \tag{3.10}$$

The interferometer system operated on VINETA has a frequency of 160 GHz corresponding to a cut-off density of $n_{cut} = 3.1 \times 10^{20}\,\mathrm{m}^{-3}$. Further information about the interferometer system can be found in Ref. [72].

The evolution of the line integrated density as measured with the 160 GHz interferometer

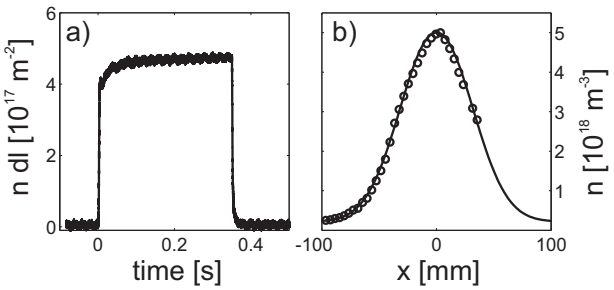

Figure 3.7: (a) Line integrated density for a plasma pulse with duration 350 ms measured with the 160 GHz interferometer system. (b) Measured ion saturation current profile normalized to the line integrated density obtained from the 160 GHz interferometer system.

system is shown in Fig. 3.7a for one plasma pulse with duration 350 ms. If the *rf*-source is switched on, the plasma density gets stationary after a transient time of typically 50 ms and decays exponentially after the *rf*-source is switched off at 350 ms. The decay time of the plasma density is determined by the parallel flux to the end plate. From Fig. 3.7a a decay time of 1.5 ms is estimated, which agrees well with the typical time for the plasma to reach the end plate, $t_{decay} = L_{\parallel}/c_s = 1.7$ ms, where $L_{\parallel} = 4.5$ m and c_s is the ion sound speed (estimated for $T_\mathrm{e} = 3$ eV). The line integrated density can be utilized to obtain absolute plasma densities if the radial plasma density profile is known. Shown in Fig. 3.7b is the measured radial ion saturation current profile normalized to the simultaneously measured line integrated density to obtain the radial plasma density profile. The line integrated density is $\int n \,\mathrm{d}l = 4.59 \pm 0.3 \times 10^{17}\,\mathrm{m}^{-2}$, which yields a peak plasma density of $n = 5 \pm 0.33 \cdot 10^{18}\,\mathrm{m}^{-3}$. This is in good agreement with the peak density evaluated from the *IU*-characteristic of the Langmuir probe $n = 4.5 \cdot 10^{18}\,\mathrm{m}^{-3}$.

3.1.3 Thomson scattering

If charged particles are accelerated in the field of an electromagnetic wave they oscillate and radiate like dipoles. In the classical limit, where the photon mass is much smaller than the particle mass, $\hbar\omega \ll mc^2$, this scattering process is called Thomson scattering. Electrons contribute mainly to the radiation because heavy ions are much less accelerated. For a single electron the Thomson scattering cross-section reads [71]

$$\sigma_{Th} = \frac{8\pi}{3} r_e^2 \sim 10^{-24}\,\mathrm{cm}^{-2}, \tag{3.11}$$

where r_e is the classical electron radius. If the phases of all contributing electrons can be assumed to be uncorrelated (incoherent scattering) the differential cross-section is given by

$$\frac{\mathrm{d}\sigma}{\mathrm{d}\Omega} = n_e r_e^2 \sin^2\varphi, \tag{3.12}$$

where φ is the angle between the electric field vector of the incident wave and the observation direction. The differential cross-section per unit volume is the ratio of power scattered into a room angle $\mathrm{d}\Omega$ to incident power per unit area. Measuring the scattered radiation intensity then yields the electron density n_e. As the electrons move they experience a Doppler-shifted excitation frequency of the incident wave in the moving frame of reference. But also the scattered radiation from the electrons is Doppler-shifted. Assuming a Maxwellian EEDF the scattered frequency spectrum exhibits a Gaussian shape with

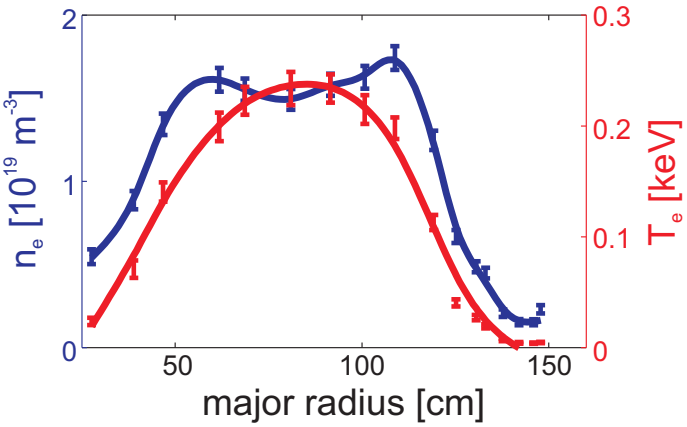

Figure 3.8: Radial profiles of electron density and temperature obtained from Thomson scattering for NSTX shot #113744.

a FWHM-wavelength [73]

$$\Delta\lambda = 4\lambda_0 \sin\frac{\theta}{2}\left(\frac{2k_\mathrm{B}T_\mathrm{e}}{mc^2}\ln 2\right)^{1/2}. \tag{3.13}$$

Here θ is the angle between wave vectors of the incident wave and the scattered wave and λ_0 is the wavelength of the incident wave. The electron temperature can be estimated from the width of the frequency peak of the scattered wave. Since the magnitude of the cross-section is very small, powerful lasers are typically used as radiation source to prevent long observation times and to increase the signal to noise ratio. On the National Spherical Torus Experiment (NSTX, cf. Ch. 7) Nd:YAG lasers operate at $\lambda_0 = 1.06\,\mu$m with high repetition rates. They are used in a backscatter geometry [74] to measure temporally resolved electron density $n_e(r,t)$ and electron temperature $T_\mathrm{e}(r,t)$ profiles. Typical profiles are shown in Fig. 3.8. The evaluation of the scattered radiation is complicated, since collective effects of the electron motion, e.g. flows, often require a coherent formulation of the differential cross-section. For electron temperatures larger than 1 keV also relativistic effects contribute to the scattering spectrum.

3.1.4 Gas puff imaging

The applicability of Langmuir probe arrays for measuring spatiotemporal fluctuations of plasma parameters in fusion devices is restricted to the far scrape-off layer (SOL) region. In regions closer to the plasma core, in particular in the plasma edge, Langmuir probes usually can not withstand the bombardment of plasma particles. The spatiotemporal structure of edge turbulence in fusion devices can be observed using optical line emission from neutral atoms. In contrast to Langmuir probe arrays, visible imaging is

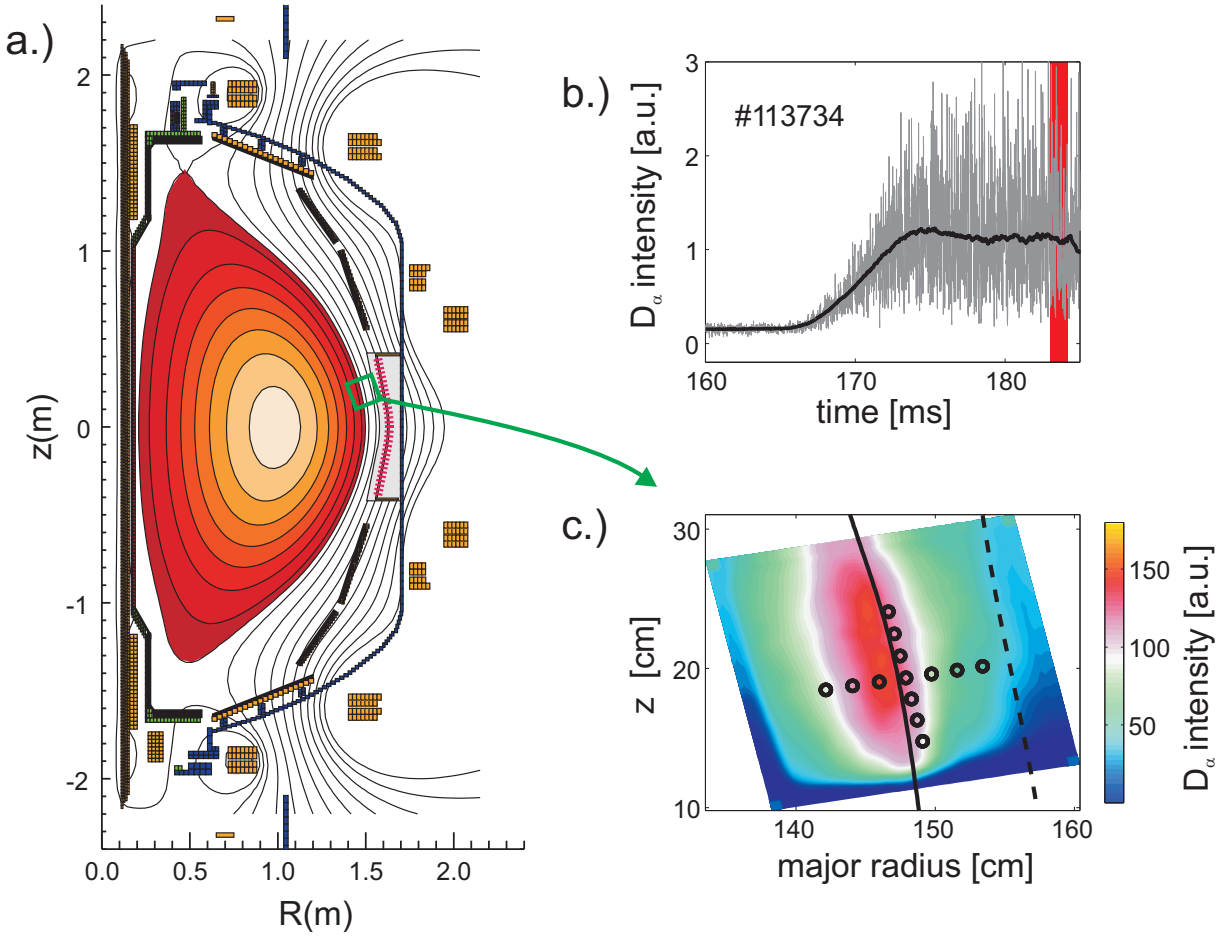

Figure 3.9: (a) Poloidal cross-section of the NSTX tokamak for shot #113734 ($t = 186\,\mathrm{ms}$). The GPI field-of-view is indicated by the green rectangular. (b) Time trace of emitted D_α light obtained from a single photodiode located close to the last closed flux surface (LCFS). The GPI data acquisition window is shown as red shaded area. (c) Time averaged D_α emission as measured with the PSI5 camera for NSTX shot #113734. The position of the LCFS obtained from LRDFit is indicated by the solid black line and the minimum position of the limiter by the dashed black line.

non-invasive and allows for higher spatial resolution. 2D-imaging of fluctuations can be obtained by using beam emission spectroscopy (BES) [75; 76; 77] or gas puff imaging (GPI) [78; 28; 79; 29]. The GPI technique is based on a localized gas puff of neutral atoms (usually Deuterium or Helium) into the plasma edge and a simultaneous measurement of the visible Balmer α-line emission with optically filtered fast framing cameras. The number of injected atoms is small enough to not significantly perturb the plasma [78] but the emission intensity is significantly increased when compared to the intrinsic plasma emission. The experimental results presented in Ch. 7 are obtained from GPI measurements at the National Spherical Torus Experiment (NSTX), where Deuterium gas is puffed into the plasma edge by use of a gas manifold mounted on the outer wall of the tokamak [80]. The visible D_α line emission (656.2 nm) is recorded with a Princeton Scientific Instru-

ments PSI5 camera (frame rate 250 kHz, 300 frames memory, 64×64 pixel) coupled to an 8×10 mm coherent optical fiber bundle [81]. The field-of-view spans over 23×23 cm radially and poloidally, centered near the last closed flux surface. The view is directed tangentially to the local magnetic field in order to resolve the radial and poloidal structure of the fluctuations perpendicular to the ambient magnetic field. A poloidal cross section of the plasma and the in-vessel components together with a D_α intensity recording is shown in Fig. 3.9 for shot #113734 at time instant $t = 186$ ms. The PSI5 field-of-view above the outer midplane is indicated by the green rectangular in Fig. 3.9a. In more detail the orientation of the GPI field-of-view is shown in Fig. 3.9c, where the time-averaged D_α emission intensity is displayed. The positions of the last closed flux surface (LCFS, derived from free boundary equilibrium reconstruction code LRDFIT at $t = 186$ ms) and the limiter shadow are indicated by the solid and dashed line, respectively. The field-of-view spans the entire plasma edge, the SOL region, and part of the limiter shadow. Complementary to the imaging system the temporal evolution of the D_α intensity is measured with 13 single views fiberoptically coupled to a photomultiplier tube and arranged as radial and poloidal one-dimensional arrays. The position of the chords is indicated in Fig. 3.9c by the black circles. Each chord is digitized with 500 kHz and 65 ksamples. The signal of the radially and poloidally centered chord close to the LCFS is shown in Fig. 3.9b. The deuterium gas manifold was opened at $t = 165$ ms and the gas starts to flow into the SOL at approximately $t = 167$ ms. At $t \approx 173$ ms a quasi-stationary D_α-emission intensity level is reached. The data acquisition of the PSI5 camera starts at $t = 183$ ms with a total acquisition time of 1.2 ms (the data acquisition time is indicated in Fig. 3.9b by the red shaded area).

The measured D_α line-emission is a nonlinear function of the electron density and electron temperature and proportional to the neutral gas density. The Balmer D_α emission rate S_α (in $\mathrm{m^{-3}s^{-1}}$) is given by [83]

$$S_\alpha = n_g f(n_e, T_e) A_{3,2} = n_g F(n_e, T_e), \tag{3.14}$$

where n_g is the ground state density of neutral Deuterium atoms, $f(n_e, T_e)$ is the branching ratio between atoms in the upper state ($m = 3$) and ground state, and $A_{3,2}$ is the spontaneous decay rate (Einstein coefficient) of the $m = 3$ to $n = 2$ transition. The function $f(n_e, T_e)$ is determined by several atomic processes as electron impact excitation, de-excitation, ionization, recombination and radiative decay [28]. Since the radiative decay rate $A_{3,2}$ is much larger than the inverse of the autocorrelation time of the fluctuations the observed emission intensity corresponds to the local plasma parameters [80]. The

spatial evolution of the ground state Deuterium density n_g and the time-resolved D_α light emission have been calculated using the DEGAS 2 neutral transport code and revealed consistency with GPI data [84; 83; 85]. For Helium a detailed comparison of the experimental and calculated He_α emission within the local GPI view is shown in Fig. 3.10 for NSTX shot #112814. For NSTX edge plasma parameters (shots considered in Ch. 7) the function $F(n_e, T_e)$ scales as $F(n_e, T_e) = n_e^{0.7-0.9} T_e^{0.6-0.8}$ due to the strong radial variation of the electron density and electron temperature in the plasma edge (cf. Fig. 3.8).
According to (3.14) the measured D_α fluctuations can be attributed to either fluctuations in n_e, T_e, n_g, or all of them. If the variations of the neutral gas density are assumed to occur on a much larger time scale than the turbulent fluctuations and assuming small electron temperature fluctuations at the edge, the D_α emission depends on the plasma density fluctuations only [29]. We note that temperature fluctuations cannot be assumed to be small *per se*, but the interpretation is simplified if electron density and temperature fluctuations are assumed to be in phase as expected theoretically [28] and confirmed by Langmuir probe measurements [86].

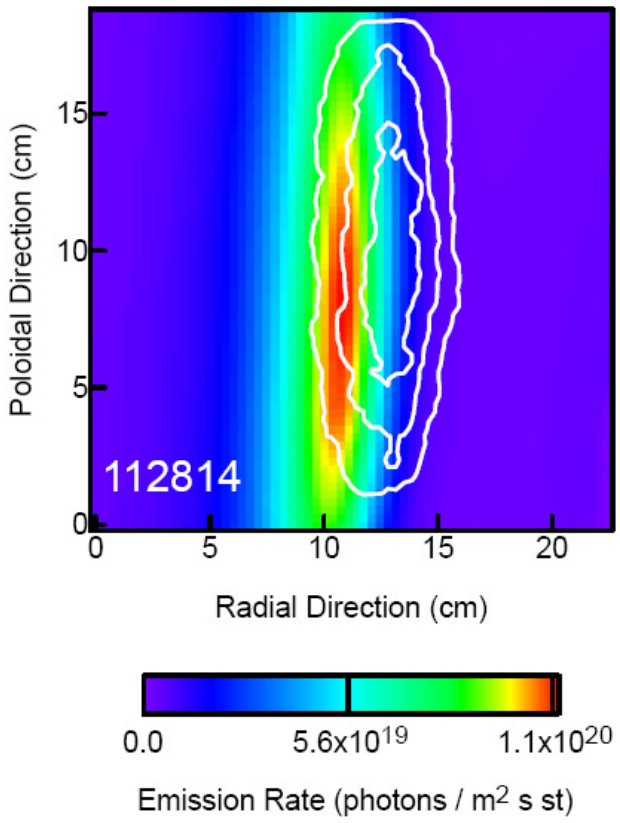

Figure 3.10: Calculated He_α emission rate of the local GPI view using the DEGAS 2 code for NSTX shot #112814 (taken from [82]). The He_α emission as measured measured with the PSI5 camera is superimposed as contour lines.

3.2 Signal processing

The characterization of fluctuating plasma parameters such as density and potential is based on the analysis of time series. From a time series the dynamical state of the plasma can be investigated by applying spectral tools as Fourier and wavelet transforms in frequency and wavenumber space or by estimating the probability distribution functions and their moments. More advanced analysis methods are higher order spectra (bicoherence) that allow for the investigation of nonlinear interaction of waves. From spatiotemporally resolved measurements the coherent part of the fluctuations can be extracted using cross-correlation or conditional-averaging techniques. These signal processing tools mentioned here are briefly introduced in the following sections.

3.2.1 Wavelet transform

Spectral analysis of time series of fluctuating quantities is mainly performed by applying the Fourier transform (FT). In 1807 Fourier discovered that sine and cosine functions can be used as orthogonal basis to represent other functions. Problems arise if the analyzed signal is non-stationary (signals whose frequency spectrum changes in time e.g. a chirp signal). Non-stationary signals can be analyzed by windowed Fourier transform, which averages the spectrum over a fraction of the timeseries and thereby yields time resolution. The main disadvantage of the windowed FT is the fixed resolution at all times and frequency scales. The resolution is determined by the Heisenberg uncertainty condition, which states that the exact time-frequency representation of a signal is unknown. For a small window width the FT gives good time resolution but poor frequency resolution and *vice versa*. In general the wavelet transform is comparable to the windowed FT but the window width changes for every analyzed spectral component. In contrast to the windowed FT, where the basic functions sine and cosine are not localized in space or time, a wavelet is a localized wave package [87; 88; 89; 90]. The wavelet transform is based on a wavelet prototype function, called mother wavelet ψ. A variety of mother wavelets exists, which all must satisfy certain mathematical criteria. In particular, a wavelet must have finite energy and no zero-frequency component, the latter requirement is also known as admissibility condition. Admissible wavelets are in principle bandpass filters. The passing spectral components are characterized by the Fourier energy spectrum of the wavelet $|\hat{\psi}(f)|^2$. The wavelet transform presented within the scope of this work is based on the Morlet wavelet, essentially a modified Gaussian [90],

$$\psi(t) = \frac{1}{\pi^{1/4}} e^{i2\pi f_0 t} e^{-t^2/2}, \tag{3.15}$$

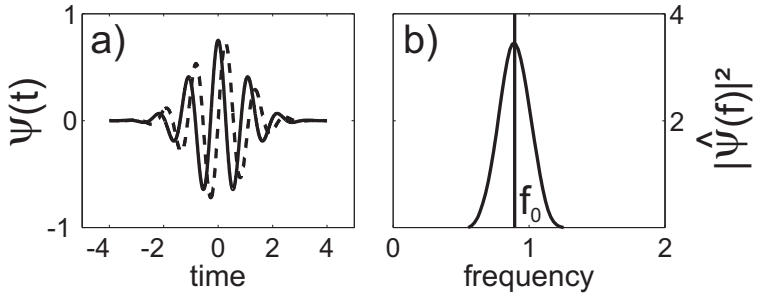

Figure 3.11: Real (solid) and imaginary (dashed) part of the Morlet wavelet (a) and corresponding energy spectrum for $f_0 = 0.894$ (b).

where the central frequency f_0 is the frequency of the complex sinusoidal inside the Gaussian envelope. The complex Morlet wavelet and its Fourier energy spectrum $|\hat{\psi}(f)|^2$ are shown in Fig. 3.11. The wavelet transform of a continuous signal $x(t)$ is defined as [90]

$$\Psi(\tau, s) = w(s) \cdot \int_{-\infty}^{\infty} x(t) \cdot \psi_{a,b}^{*} \left(\frac{t-b}{a} \right) \mathrm{d}t, \tag{3.16}$$

where a and b are the dilation and translation parameter of the wavelet, respectively. The weighting function $w(s)$ is set to $2/\sqrt{|s|}$ to ensure that the wavelet has on each scale the same energy. The scale parameter s of the wavelet is related to the frequency via $s = 1/f$. An example of a Morlet wavelet transform for a chirped signal is shown in Fig. 3.12. For detailed informations about using wavelets in plasma physics the reader is referred to Refs. [91; 92].

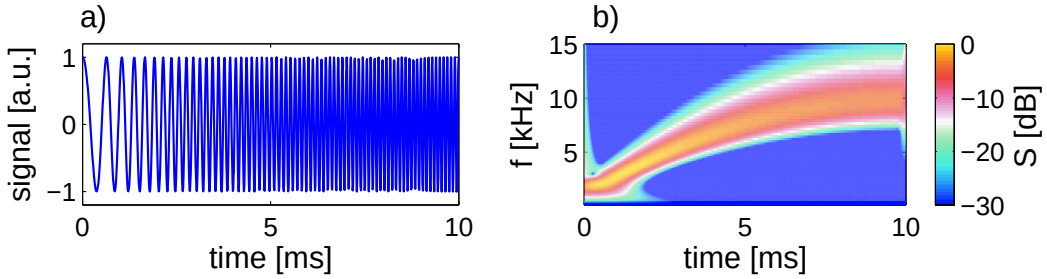

Figure 3.12: Chirped signal with increasing frequency $f = 1 - 10\,\mathrm{kHz}$ (a) and corresponding Morlet wavelet spectrum (b).

3.2.2 Probability distribution function

The probability distribution function is defined as the probability p to find a stochastic variable x in the interval $(x_1, x_1 + \mathrm{d}x)$,

$$p(x_1 \leq x \leq x_1 + \mathrm{d}x) = \int_{x_1}^{x_1+\mathrm{d}x} P(x)\,\mathrm{d}x. \tag{3.17}$$

$P(x)$ is the probability distribution function (PDF), which obeys

$$P(x) \geq 0 \;\forall\, x_1 \qquad \text{and} \qquad \int_{-\infty}^{\infty} P(x)\,\mathrm{d}x = 1. \tag{3.18}$$

In other words the PDF is a measure of the amplitude distribution of the stochastic variable x_1. For the estimation of the PDF of a fluctuation time series the time series is binned into N amplitude intervals between the minimum and maximum amplitude of the time series. The probability p to find an event in the ith amplitude interval is then given by the ratio of the numbers of events within the ith amplitude interval and the number of all detected events. From the probability p the PDF is estimated by normalization to the amplitude interval width. The properties of the PDF are characterized by its moments. For discretized signals, the summation over the PDF multiplied by $(x- < x >)^j$ yields the jth moment μ_j of the PDF

$$\mu_j = \sum_n (x- < x >)^j\, P_n, \tag{3.19}$$

with $n = 1, 2, \cdots, N$. The first four moments are:

a) mean value

$$\mu_1 =< x >= \sum_n x^n P_n, \tag{3.20}$$

b) variance

$$\sigma^2 = \sum_n (x^n - \mu_1)^2 P_n, \tag{3.21}$$

c) skewness

$$s = \sum_n (x^n - \mu_1)^3 P_n/\sigma^3, \tag{3.22}$$

d) kurtosis

$$K = \sum_n (x^n - \mu_1)^4 P_n/\sigma^4 - 3. \tag{3.23}$$

The variance is the squared standard deviation σ. Skewness and kurtosis measure the asymmetry and the flatness of the PDF compared to a Gaussian PDF, respectively (for

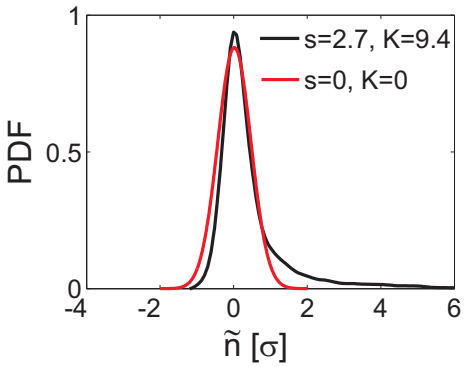

Figure 3.13: Probability distribution function (PDF) of density fluctuations (black) with skewness $s = 2.7$ and kurtosis $K = 9.4$. A Gaussian fit to the PDF (red) with $s = K = 0$ is also shown.

a Gaussian PDF skewness and kurtosis are zero). For illustration, a PDF with non-zero kurtosis and skewness is shown in Fig. 3.13.

The PDF is a robust measure of intermittency. As outlined in Ch. 1, the PDF of self-similar isotropic turbulence has a Gaussian shape, independent of the scale under consideration due to the concept of self-similarity. Intermittent events, i.e., large amplitude events with short auto-correlation times, are located in the wings of the PDF and lead to a deviation of the PDF from a Gaussian shape. This can be quantified by the moments of the PDF and the kurtosis is a measure how peaked the PDF is, compared to a Gaussian. For an intermittent signal the kurtosis is expected to grow without bound with frequency or wavenumber [3].

3.2.3 Bicoherence analysis

The relation of three-wave interaction and nonlinearities and its importance for redistributing energy among various scales of motion was already described in Sec. 2.3. Nonlinear mode-coupling and energy transfer can be investigated by higher order spectra [93; 94; 95; 96], such as bispectrum or trispectrum. Three wave-interactions that arise from quadratic nonlinearities can be described by the auto-bispectrum

$$B_{k,l} = \left\langle \hat{u}_l \hat{u}_k \hat{u}^*_{m=k+l} \right\rangle , \tag{3.24}$$

where $\hat{u}$ is the fluctuating physical quantity of interest (e.g. plasma density fluctuations) in Fourier space, k, l, m are the Fourier modenumbers, and * denotes the complex conjugate. The $\langle\cdot\rangle$ denotes ensemble averaging over a large number of realizations of the spectral function inside the brackets. The bispectrum measures the degree of phase coherence between three Fourier modes that obey the summation rule $\omega_m = \omega_k \pm \omega_l$ in frequency space and $\boldsymbol{k}_m = \boldsymbol{k}_k \pm \boldsymbol{k}_l$ in wavenumber space. If the phases of the Fourier modes are fully

uncorrelated, the bispectrum vanishes. It is often more convenient to use the normalized bispectrum, called bicoherence

$$b_m^2 = \frac{|B_{k,l}|^2}{\langle |u_k u_l|^2 \rangle \, \langle |u_{k+l}|^2 \rangle}. \tag{3.25}$$

To illustrate the analysis a signal $y(t)$ is generated, which consists of two coupled sine waves

$$\begin{aligned} y_a(t) &= A \, \sin(2\pi f_a t + \phi_a), \\ y_b(t) &= B \, \sin(2\pi f_b t + \phi_b), \\ y(t) &= y_a(t) + y_b(t) + y_a(t) \cdot y_b(t) + \chi, \end{aligned}$$

where $f_a = 1.2\,\text{kHz}$, $f_b = 0.8\,\text{kHz}$ and χ denotes 10% noise. The amplitudes A and B and the phases ϕ_a and ϕ_b are randomly choosen constants. The calculated bicoherence is shown in Fig. 3.14a and the corresponding frequency spectrum in Fig. 3.14b. The bicoherence peaks at $f_1 \pm f_2$ which yields bi-frequencies of $2\,\text{kHz}$ and $0.4\,\text{kHz}$. The contribution of the bi-frequencies to the frequency spectrum is clearly observed in Fig. 3.14b.
The bicoherence is a measure for the coupling of different Fourier modes in frequency and wavenumber space. The energy that is exchanged by the different Fourier modes of the spectrum due to three-wave interaction is determined by the energy transfer function $T(\omega_k, \omega_l)$ and is related with to the wave coupling coefficient $\Lambda(\omega_k, \omega_l)$, which measures the strength of the coupling (cf. Sec. 2.3). Direct measurements of the energy transfer function are difficult to obtain. A few attempts were made with data obtained in the TEXT

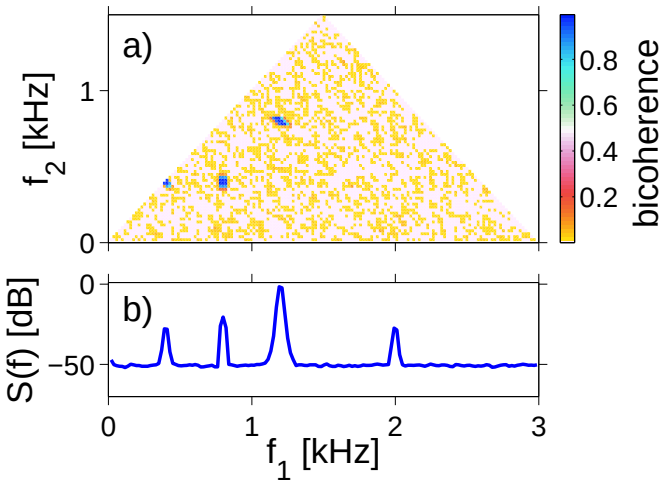

Figure 3.14: Auto-bicoherence (a) of the signal $y(t)$ (3.26) and corresponding frequency spectrum (b) of $y(t)$. The frequency domain of the bicoherence in (a) is restricted by the Nyquist limit.

tokamak [97] and in the TFTR tokamak [98].

3.2.4 Cross-correlation and conditional-averaging techniques

The cross-correlation function of two time series $u_1(\boldsymbol{r}_1, t)$ and $u_2(\boldsymbol{r}_2, t)$ with length T is defined as [99]

$$R(\boldsymbol{r}_1, \boldsymbol{r}_2, \tau) = \lim_{T\to\infty} \frac{1}{T} \int_0^T u_1(\boldsymbol{r}_1, t) u_2(\boldsymbol{r}_2, t+\tau)\, \mathrm{d}t, \tag{3.26}$$

where τ is a variable time lag. To compare the cross-correlation amplitude of various signals with different amplitudes the normalized cross-correlation function

$$\rho(\tau) = \frac{R(\boldsymbol{r}_1, \boldsymbol{r}_2, \tau)}{[R(\boldsymbol{r}_1, \boldsymbol{r}_1, 0) R(\boldsymbol{r}_2, \boldsymbol{r}_2, 0)]^{1/2}} \qquad \text{with} \qquad \rho(\tau) \in [-1, 1] \tag{3.27}$$

is more suitable. $R(\boldsymbol{r}_1, \boldsymbol{r}_1, 0)$ and $R(\boldsymbol{r}_2, \boldsymbol{r}_2, 0)$ are the auto-correlation functions of the individual signals. The auto-correlation function always peaks at $\tau = 0$ and its $1/e$ decrease is the correlation length (or time). The cross-correlation is a measure for the phase coherence of the two signals. If one time series is shifted in time by t_0, the maximum is found at $\tau = t_0$. If the signals are not correlated (no defined phase relation as for random signals) $\rho = 0$ for all time lags. A negative cross-correlation amplitude $\rho = -1$ results from time series with a phase shift of π. An efficient way to calculate the cross-correlation function is to apply the Wiener-Khintchine therorem [100], which relates the cross-correlation function to the inverse Fourier transform of the cross-power spectral density $S_{u_1,u_2}(\omega)$

$$R(\boldsymbol{r}_1, \boldsymbol{r}_2, 0) = \int_{-\infty}^{\infty} S_{u_1,u_2}(\omega) \exp(i\omega t)\, \mathrm{d}\omega. \tag{3.28}$$

The cross-correlation function can be utilized to extract the coherent part of a fluctuating quantity. If one is interested in the coherent part of the fluctuations that is associated with specific features such as high-amplitude intermittent bursts that appear occasionally, the conditional-averaging (CA) technique [101] is more appropriate, which is in many ways comparable to the cross-correlation function. It can be described as follows: When the first time series $u_1(\boldsymbol{r}_1, t)$ fulfills a pre-defined condition p at a certain time instant t_i, a time interval of length $\Delta\tau$ centered around t_i is extracted from both time series. If the condition is satisfied for N times, the N sub-timeseries are taken as statistically independent realizations. By ensemble averaging the sub-time series the coherent part of the fluctuations is extracted while the incoherent part is suppressed. The conditional

averaging procedure can be formally expressed as

$$\langle R_{CA} \rangle (\boldsymbol{r}_0 + \mathrm{d}\boldsymbol{r}, \tau) = \frac{1}{N} \sum_{i=1}^{N} \left[u_2(\boldsymbol{r}_0 + \mathrm{d}\boldsymbol{r}, t_i + \tau) \mid u_1(\boldsymbol{r}, t_i) = p \right], \tag{3.29}$$

with $\tau \in [-\Delta\tau/2, \Delta\tau/2]$. The condition p is a free parameter and is chosen usually as a threshold condition on the amplitude combined with a slope condition (events can be detected at rising or falling slope). The choice of $\Delta\tau$ is not critical. To avoid overlapping effects, the time between each two detected events must be greater than $\Delta\tau$. However, $\Delta\tau$ should be larger than the autocorrelation time of the signal to ensure that the subseries are statistically independent realizations of a random process [102].

Both methods are well suited to reconstruct the coherent part of spatiotemporal dynamics of fluctuations. To recover the dynamics of the coherent fluctuations in the two dimensional (x, y)-plane with sparse spatial resolution, a fixed Langmuir probe acts as reference probe recording the time series $u_1(\boldsymbol{r}_1, t)$ while $u_2(\boldsymbol{r}_2, t)$ is obtained from a single Langmuir probe or probe array that is moved across the plasma column. For each position of the displaced probe, time series of $u_1(\boldsymbol{r}_1, t)$ and $u_2(\boldsymbol{r}_2, t)$ are recorded and the cross-correlation or conditional averaging technique is applied. As a result, the spatiotemporal evolution of the coherent fluctuations in the time interval $\Delta\tau$ is obtained. The effect of extracting the coherent part of the fluctuation from a signal embedded in random noise is illustrated in Fig. 3.15. Fig. 3.15.a shows the surrogate data $u(x, y, t)$ in the two-dimensional (x, y)-plane for a certain time instant t_0. The spatial grid is 64×64 points and the length of the dataset is $N = 8192$ samples (at a sampling frequency of 1 MHz). The data consists of a circular structure (2D-Gaussian) embedded in 80% Gaussian noise.

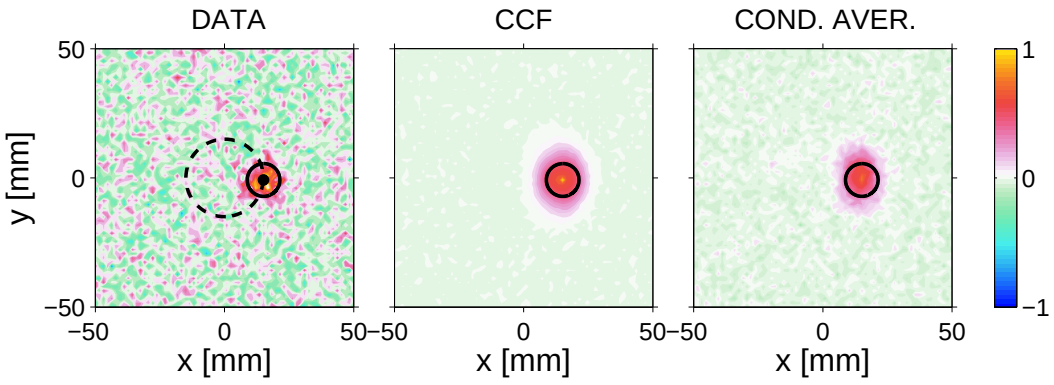

Figure 3.15: Example of extracting a spatiotemporal coherent structure using the cross-correlation and conditional- averaging techniques for surrogate data: (a) Two-dimensional surrogate data $u(x, y, t)$, (b) result of the cross-correlation technique and (c) result of the conditional-averaging technique (see text for details).

The solid black ring in Fig. 3.15a indicates the area where the amplitude of the structure dropped to $1/e$ of its peak amplitude. The structure propagates purely azimuthally in clockwise direction with an equivalent frequency $f = v_\theta/(2\pi r) = 8$ kHz. The trajectory of the structure is indicated in Fig. 3.15a with a dashed line and the position of the reference probe, recording the time series $u_1(\boldsymbol{r}_1, t)$, is indicated as a black dot. The reference probe is located in the center of the structure. For the entire grid of 64×64 points, the cross-correlation and conditional-averaging technique is applied.. The results at time lag $\tau = 0$ are shown in Figs. 3.15b and 3.15c. We observe that the incoherent fluctuations of the random noise are suppressed while the coherent structure is clearly identified. Note that the conditional-average amplitude is the amplitude of the structure itself, whereas the cross-correlation amplitude is normalized. It is clearly seen that the azimuthal correlation length is larger than the actual structure size, whereas the structure is well recovered by the the conditional-averaging technique [102].

4

The VINETA device

The VINETA device is a cylindrical linearly magnetized plasma experiment, specifically designed for studies at plasma waves and instabilities. A schematic drawing of the device is shown in Fig. 4.1. It consists of four stainless steel vacuum chambers with a diameter of 40 cm and a length of 1.1 m. The total length of the device is 4.5 m (including the helicon source region). To ensure good experimental access to the plasma, each module has 13 CF-40, two CF-63, and two rectangular ports (90×250 mm). The vacuum vessel is immersed in a set of 36 water cooled magnetic field coils which provide a magnetic field induction of $B \leq 100$ mT. The coil current of each module can be controlled separately by five 25 kW power supplies. A combination of a turbomolecular and rotary pump at the end of the device provides a base pressure of $p_0 < 10^{-4}$ Pa. Plasma is generated by wave-heated discharges, either by *rf*-heating or electron cyclotron resonance heating (ECRH). For the experiments presented here only the helicon plasma source was used.

The helicon source consists of a right-handed helical $m = 1$ antenna with a length of 30 cm placed around a glass vacuum extension with a diameter of 10 cm. The antenna is typically driven with a *rf*-frequency of $f_{\mathrm{rf}} = 13.56$ MHz and input powers of $P_{\mathrm{rf}} < 5$ kW. A conventional matching network is used to match the *rf*-amplifier output impedance of 50 Ω to the antenna impedance [103]. Dependent on the applied *rf*-power, a capacitive, inductive or helicon discharge can be established [104; 105]. Typical plasma density profiles for the three *rf*-discharge types are shown in Fig. 4.2.

The transition from the capacitive mode to the inductive mode is governed by the skin

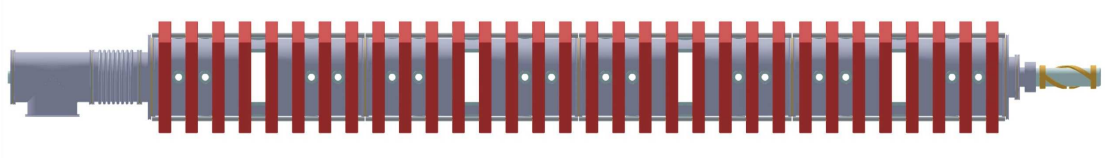

Figure 4.1: Schematics of the VINETA device. For illustration the magnetic field coils which surround the helicon plasma source to the right are not shown.

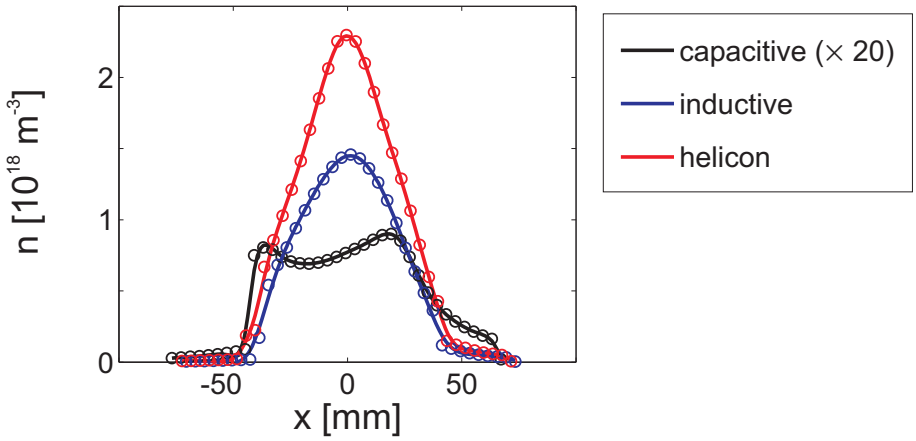

Figure 4.2: Radial plasma density profiles for a capacitive, inductive and helicon discharge. The *rf*-input power is $P_{\mathrm{rf}} = 600\,W$ (capacitive mode), $P_{\mathrm{rf}} = 800\,W$ (inductive mode) and $P_{\mathrm{rf}} = 1000\,W$ (helicon mode), respectively. All other operational parameters are kept constant.

depth, which reads in the collisionless limit ($\nu_{en} << \omega$) [63]

$$\delta_p = \frac{c}{\omega_{pe}} = \sqrt{\frac{m_e}{e^2 \mu_0 n}}. \tag{4.1}$$

The skin depth δ_p is a measure for the penetration depth of electromagnetic waves into the plasma. Shielding of electric fields is attributed to the *rf*-induced skin current within a skin depth layer of thickness δ_p. For low electron densities, the skin depth becomes larger than the plasma radius and no shielding of electric fields occurs. This is called capacitive mode, where the heating of the plasma is achieved only by Ohmic and stochastic heating in the *rf*-sheaths near the antenna [63]. For higher electron densities, the skin depth gets smaller than the plasma radius and the skin current dominates the plasma heating in addition to Ohmic and stochastic heating. This mode is known as inductive discharge. Capacitive and inductive discharges are well understood and commonly used for industrial applications. While capacitive and inductive discharges can be operated without a magnetic field, a helicon wave discharge requires a certain magnetic field strength, as outlined in the following brief excursion.

4.0.5 Helicon waves

Helicon waves were observed in the mid 1960's first in solid state plasmas [106; 107] and then in gaseous plasmas [108]. In the late 1970's Boswell discovered that helicon waves can be used to produce dense plasma with densities up to $10^{19}\,\mathrm{m}^{-3}$ with only a few kW of *rf*-power [109; 110]. Nowadays, helicon sources are widely used for practical applications, e.g. materials processing [111] and Hall thrusters [112]. However, it is still a

scientific debate what mechanism leads to the high ionization efficiency and strong damping of the helicon waves. The energy transfer from the wave to the plasma particles has been investigated with respect to Coulomb collisional damping [113], Landau damping [113; 114], mode conversion near the lower hybrid frequency [110; 115], and nonlinear trapping of fast electrons [116; 117]. In some operation regimes, non-Maxwellian electron distributions were found to contribute significantly to the ionization process [118]. However, the results are not fully conclusive.

Helicon waves are bounded whistler waves. Whistler waves in turn are right-handed circularly polarized electromagnetic waves in the low frequency range $\Omega_{ci} \ll \omega \ll \Omega_{ce}$ which can be naturally observed in the ionosphere. The dispersion relation of the whistler wave is

$$\frac{k^2 c^2}{\omega^2} = \frac{\omega_{pe}^2}{\omega \Omega_{ce} \cos\theta}. \tag{4.2}$$

Here $\boldsymbol{k}$ is the wave vector and θ is the angle between $\boldsymbol{k}$ and the axial magnetic field B_z. In the low-frequency limit, Helicon waves satisfy the same dispersion relation (4.2) [63]. The conducting boundaries of the vacuum vessel require that the tangential components of the wave electric fields vanish and thus impose an eigenmode structure on the helicon wave. The boundary condition can be written as [63]

$$mkJ_m(k_\perp r) + k_z J_m^{'}(k_\perp r) = 0, \tag{4.3}$$

where m is the azimuthal mode number and J_m the mth-order Bessel function of the first kind. One assumes wave field quantities to vary as $\boldsymbol{E}, \boldsymbol{B} \sim \exp\left[i(\omega t - k_z z - m\theta)\right]$. For the $m = 1$ antenna design used in VINETA , (4.3) can be solved numerically with $k_\perp r = 3.83$ in the limit $k_z << k_\perp$. The axial wavelength of the helicon mode yields in this limit [63]

$$\lambda_z = \frac{3.83}{r} \frac{B}{e\mu_0 n f_{\mathrm{rf}}}. \tag{4.4}$$

For a given parallel wavelength $\lambda_z = 2\pi/k_z$ of the helicon wave, which is mainly determined by the antenna length, the plasma density is proportional to the applied magnetic field. This is in agreement with experimental observations (cf. Sec. 4.2). Inserting the experimental parameters ($f_{\mathrm{rf}} = 13.56\,\mathrm{MHz}$, $B = 0.08\,\mathrm{T}$, $\lambda = 0.3\,m$, $r = 0.05\,\mathrm{m}$) in (4.4), one obtains a plasma density of $n = 2.2 \cdot 10^{18}\,\mathrm{m}^{-3}$, which is in excellent agreement with the experimental observations (cf. Fig. 4.2). For detailed measurements of the helicon wave fields in VINETA the reader is referred to Ref. [104].

4.1 Operation and plasma parameters

Typical plasma parameters for Argon helicon discharges are compiled in Tab. 4.1. Important frequencies, lengths, velocities and collisionalities are summarized in Tab. 4.2. Three parameters are worthwhile to note: The drift scale ρ_s as the typical spatial scale of fluctuations in drift-wave turbulence is $\approx 10 - 25\,\mathrm{mm}$ for our measurements. The plasma-β is relatively small, $\beta \approx 0.2\,\%$, and satisfies the electrostatic assumption (2.39). For the typical plasma parameters shown in Tab. 4.2, Coulomb collisions dominate over collisions with neutrals. This does usually not hold for the entire radial plasma profile, since plasma density and electron temperature exhibit specific radial profiles. Profiles of the different collisionalities are not shown here, but for the considered plasma parameters a transition between two collisional regimes are observed, i.e. the plasma core is dominated by Coulomb collisions and the plasma edge by collisions with neutrals [62].

parameter	typical value
rf-power P_{rf} [kW]	1 - 4
rf-frequency f_{rf} [MHz]	13.56
neutral gas pressure p_0 [Pa]	0.1 - 0.3
magnetic field B [mT]	35 - 100
peak electron density n_e [$10^{19}\,\mathrm{m}^{-3}$]	0.01 - 2
peak electron temperature T_{e} [eV]	2 - 3.5
peak ion temperature T_{i} [eV]	≤ 0.5
parallel connection length $L_{\parallel}$ [m]	4.5
density gradient length $L_{\perp}^{-1}$ [m^{-1}]	50-112

Table 4.1: Typical operational and plasma parameters for Argon helicon discharges.

parameter	unit	range	typical value
frequencies			
ion cyclotron frequency Ω_{ci}	[10^5 rad/s]	0.84 - 2.4	1.45
electron cyclotron frequency ω_{ce}	[10^{10} rad/s]	0.6 - 1.8	1.05
plasma frequency ω_{pe}	[10^{11} rad/s]	0.2 - 2.5	1.26
lengths			
electron gyroradius r_{ce}	[mm]	0.05 - 0.2	0.09
ion gyroradius r_{ci}	[mm]	6 - 11	7
Debye length λ_{Debye}	[μm]	2.4 - 30	5.8
collisionless skin depth δ_p	[cm]	0.1 - 1.7	0.24
drift scale ρ_s	[mm]	12 - 49	19
velocities			
ion sound speed c_s	[km/s]	2.2 - 2.9	2.7
electron thermal velocity $v_{th,e}$	[10^3 km/s]	0.8 - 1.1	1.03
ion thermal velocity $v_{th,i}$	[km/s]	0.9 - 1.5	0.98
Alfvén velocity v_A	[10^3 km/s]	0.028 - 1	0.092
plasma$-\beta$	[%]	0.0008 - 2	0.2
collisions			
electron-electron ν_{ee}	[10^7 s^{-1}]	0.04 - 13	2
electron-ion ν_{ei}	[10^7 s^{-1}]	0.06 - 18	2.9
ion-ion ν_{ii}	[10^6 s^{-1}]	0.03 - 15	4.4
electron-neutral ν_{en}	[10^6 s^{-1}]	0.5 - 4	1.6
ion-neutral ν_{in}	[10^4 s^{-1}]	0.8 - 4	1.1
charge-exchange ν_{cx}	[10^4 s^{-1}]	0.9 - 4	1.35

Table 4.2: Derived plasma parameters for Argon helicon discharges: The range of values is calculated for the plasma parameters compiled in Tab. 4.1 and typical values are calculated for the reference set $B = 60\,\mathrm{mT}$, $p_0 = 0.15\,\mathrm{Pa}$, $T_e = 3\,\mathrm{eV}$, $T_i = 0.2\,\mathrm{eV}$ and $n = 5 \cdot 10^{18}\,\mathrm{m}^{-3}$.

4.2 Time-averaged profiles

Time-averaged radial profiles of plasma density n, plasma potential ϕ, and electron temperature T_e of helicon discharges are shown in Fig. 4.3 for different values of the magnetic field $\boldsymbol{B}$, an Argon neutral gas pressure $p_0 = 0.15\,\mathrm{Pa}$ and *rf*-power $P_\mathrm{rf} = 1.5\,\mathrm{kW}$.
In general, the radial profiles of the plasma parameters follow the shape of a function

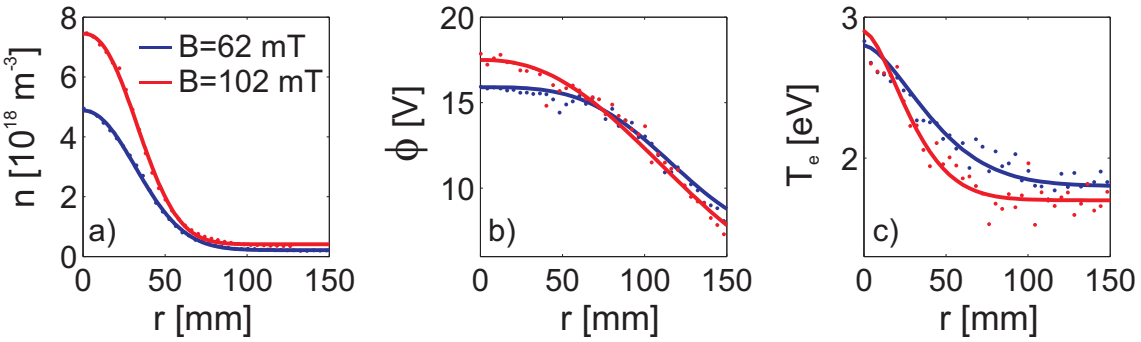

Figure 4.3: Radial profiles of plasma density (a), plasma potential (b) and electron temperature for helicon discharges with Argon neutral gas pressure $p_0 = 0.15\,\mathrm{Pa}$ and *rf*-power $P_{\mathrm{rf}} = 1.5\,\mathrm{kW}$. The solid lines correspond to fits to the data for a function $n, \phi, T_e \sim \exp\left([(r-a)/b]^c\right) + d$.

$n, \phi, T_e \sim \exp\left([(r-a)/b]^c\right) + d$ with the $1/e$-folding length of the plasma potential (Fig. 4.3b) being larger than that of the plasma density and the electron temperature (Figs. 4.3a and 4.3c). For increased magnetic field, the peak density increases from $n = 4.5 \cdot 10^{18}\,\mathrm{m}^{-3}$ at $B = 62\,\mathrm{mT}$ to $n = 7.5 \cdot 10^{18}\,\mathrm{m}^{-3}$ at $B = 102\,\mathrm{mT}$, which is in agreement with the helicon dispersion relation (4.4). From the fits to the data, the first order perpendicular drift velocities, $\boldsymbol{v}_{E\times B} \sim -\nabla_r \phi$ and $\boldsymbol{v}_{d,e} \sim \nabla_r \ln n/T_\mathrm{e}$ can be estimated. The modulus of these drift velocities together with the resulting azimuthal drift frequencies is shown in Fig. 4.4. Both, the $\boldsymbol{E}\times\boldsymbol{B}$- and electron diamagnetic drift exhibit absolute peak values of 1.2-2 km/s but they have opposite azimuthal directions. Due to the different radial profiles of plasma density and plasma potential, respectively, $\boldsymbol{v}_{d,e}$

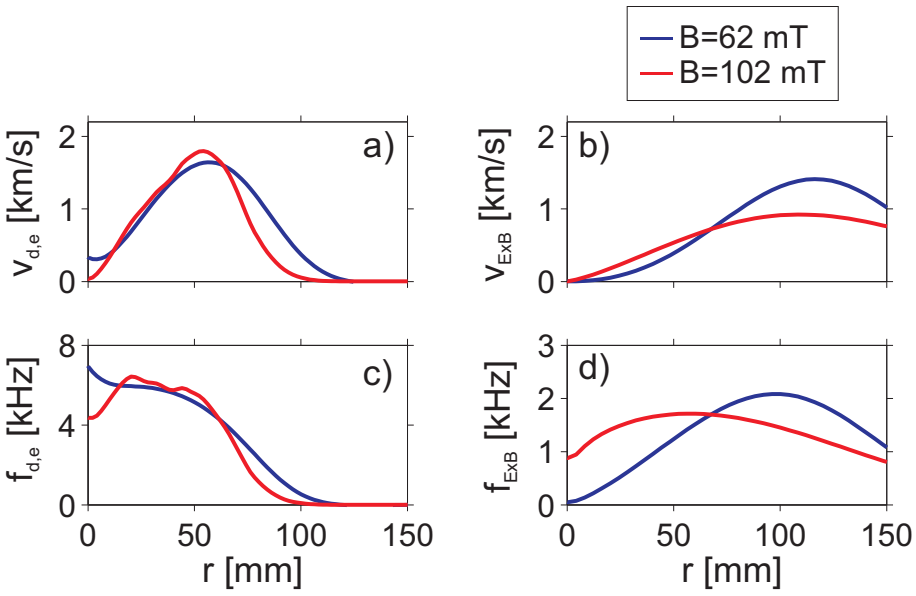

Figure 4.4: Modulus of the $\boldsymbol{E}\times\boldsymbol{B}$- and electron diamagnetic drift velocity (a-b) and corresponding frequencies (c-d), as calculated from the fits to the data shown in Fig. 4.3.

peaks in the maximum density gradient at $r = 50 - 70\,\text{mm}$ while $\boldsymbol{v}_{E\times B}$ reaches its peak value in the plasma edge at $r = 100 - 120\,\text{mm}$. The corresponding drift frequencies $\omega/2\pi = v/2\pi r$ are shown in Fig. 4.4c-d. The peak value of the electron diamagnetic drift frequency $\omega_{d,e}/2\pi$ is in a range of $4 - 6\,\text{kHz}$ while the $\boldsymbol{E}\times\boldsymbol{B}$-frequency $\omega_{E\times B}/2\pi$ is typically smaller with $2\,\text{kHz}$.

4.3 Basic characterization of fluctuations

For a wide range of external control parameters as neutral gas pressure p_0 and magnetic field B low-frequency oscillations with $\omega << \Omega_{ci}$ of plasma density and plasma potential can be observed in VINETA. The fluctuations are localized in the region of maximum radial plasma pressure gradient, indicating that the fluctuations are due to the gradient driven drift-wave instability. This conjecture is confirmed by other experimentally observable features:

- The plasma density and plasma potential fluctuation levels peak in the radial plasma pressure gradient region and the normalized plasma density and plasma potential fluctuations are of similar magnitude, $\tilde{n}/n \sim e\tilde{\phi}/T_\text{e}$.
- The phase shift between plasma density and plasma potential fluctuations is non-zero, $\delta(\tilde{n}, \tilde{\phi}) > 0$, with $\tilde{n}$ ahead of $\tilde{\phi}$.
- The phase velocity $v_{ph} = \omega/k$ is determined by the electron diamagnetic drift velocity, Doppler shifted by the $\boldsymbol{E}\times\boldsymbol{B}$-drift.
- The parallel wavelength $\lambda_\parallel = 2\pi/k_\parallel$ is non-zero and much larger than the perpendicular one $k_\parallel \ll k_\perp$.
- The fluctuations develop a spatiotemporal mode structure in the radial-azimuthal plane due to the periodic boundary conditions in the cylindrical geometry of VINETA.

A detailed investigation of the observed fluctuations unambiguously showed that the governing instability in VINETA is the drift-wave instability [30; 31]. The main experimental characteristics of the drift-wave instability are summarized in Fig. 4.5. In Figs. 4.5a and 4.5b, the radial frequency spectra profiles of plasma density and plasma potential fluctuations are shown. The background density profile $n_0(r)$ is superimposed as the white solid line. The spectra peak in the region where the density gradient $\nabla_r n_0(r)$ peaks, at a frequency of $\omega/2\pi = 6.5\,\text{kHz}$ and higher harmonics. The phase relation between plasma density and plasma potential fluctuations in the radial plasma density gradient

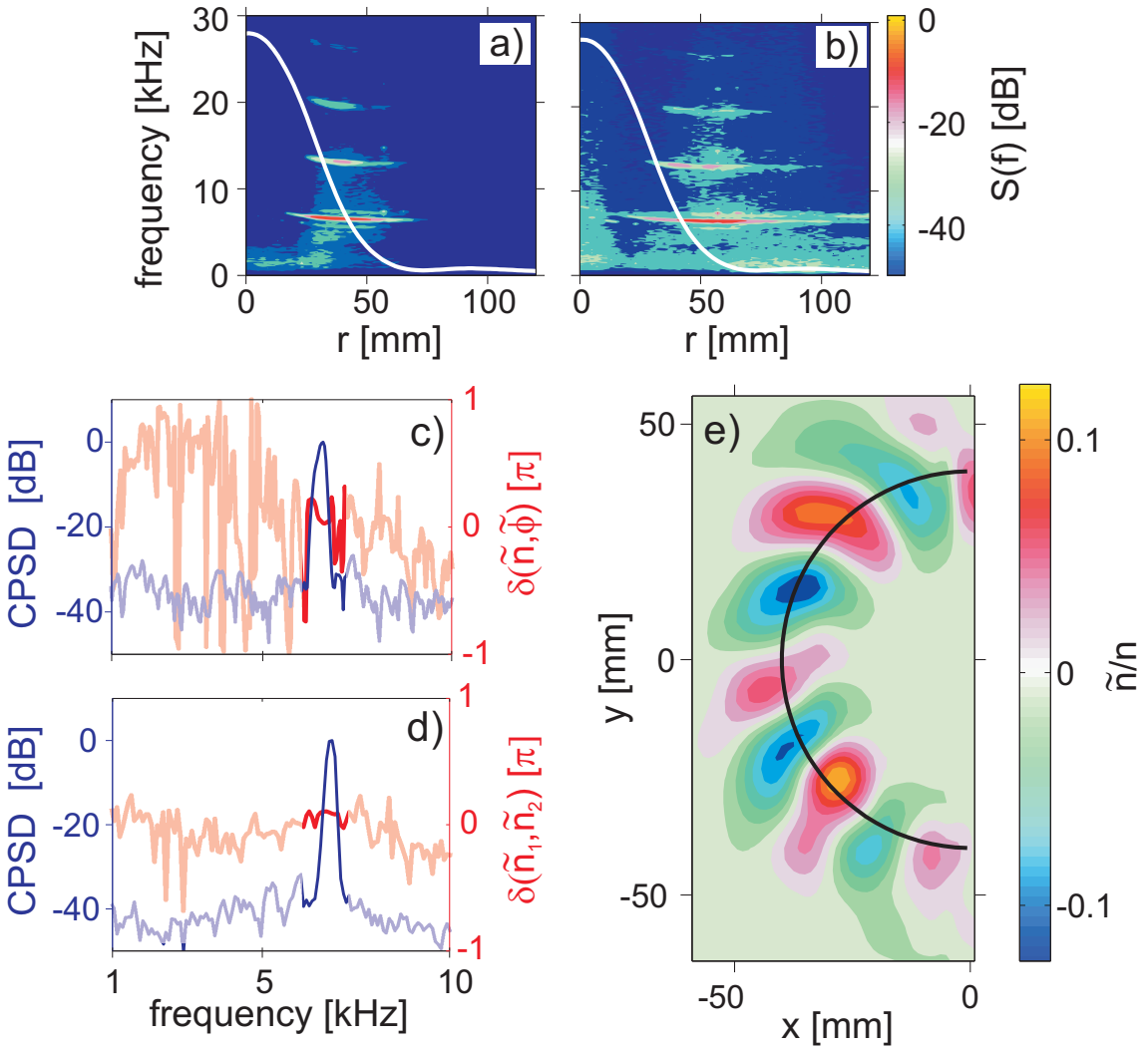

Figure 4.5: Experimental features of the drift-wave instability: Radial evolution of frequency spectra of density (a) and potential fluctuations (b). Cross-power spectrum (blue) and phase shift (red) between density and potential fluctuations (c). Estimation of the parallel wavelength by the cross-power (blue) and phase (red) spectrum of density fluctuations at two axial positions along the magnetic field (d). Spatial structure of a drift wave with azimuthal modenumber $m = 9$ in the (x, y)-plane (e). The maximum radial density gradient is indicated by the solid black circle.

region is shown in Fig. 4.5c. The cross-power spectrum (blue curve) peaks at the frequency of the drift wave. The phase spectrum $\delta(\tilde{n}, \tilde{\phi})$ (red curve) displays large variations in the frequency range 1-10 kHz but has a well defined value at the drift-wave frequency, where $\delta(\tilde{n}, \tilde{\phi}) \approx 0.1 - 0.15\,\pi$. The most important property to distinguish drift waves from Rayleigh-Taylor type instabilities that may also occur in the pressure gradient (flute modes), is the finite parallel wavelength $\lambda_\parallel = 2\pi/k_\parallel$. The wavelength is estimated from the phase $\delta[\tilde{n}(z_1), \tilde{n}(z_2)]$ between density fluctuations simultaneously measured at two axial positions z_1 and z_2 along the magnetic field. The axial separation is $\Delta z = z_2 - z_1 = 0.27$ m. The cross-power spectrum and phase spectrum $\delta[\tilde{n}(z_1), \tilde{n}(z_2)]$

are shown in Fig. 4.5d. At the drift-wave frequency the phase is constant and yields for the parallel wavelength $\lambda_\parallel = 2\pi\Delta z/\delta = 5.9 \pm 0.6$m. Detailed measurements in different parameter regimes revealed that the parallel wavelength $\lambda_\parallel$ is mainly determined by low multiples of the machine length [30]. The spatiotemporal structure of a drift wave with azimuthal mode number $m = 9$ is shown in Fig. 4.5e. For measurement reasons only half of the azimuthal plane is shown. The coherent part of the density fluctuations is extracted by applying the cross-correlation technique (cf. Sec. 3.2.4). The amplitude is renormalized to the relative fluctuation amplitude $\tilde{n}/n_0$. In Fig. 4.5e the result for correlation time lag $\tau = 0$ is shown. The $m = 9$ drift-wave mode is located in the plasma density gradient and propagates azimuthally counterclockwise in the direction of the electron diamagnetic drift $\boldsymbol{v}_{de}$. Details of the mode structure have been investigated, e.g. the radially sheared shape has been shown to be a consequence of the radial profiles of collision frequencies [31].

The potential fluctuations $\tilde{\phi}$ associated with a drift wave gives rise to an azimuthal electric field $\tilde{E}_\theta$, which is typically of the order $\tilde{E}_\theta \sim 10{-}20$ V/m. Due to the non-vanishing phase shift $\delta(\tilde{n}, \tilde{\phi})$ the resulting radial particle flux $\tilde{\Gamma} = \tilde{n}\tilde{E}_\theta/B$ has a non-zero mean value, even if the density and potential fluctuations are mean-free. Since the density perturbation $\tilde{n}$ is ahead of the potential perturbation $\tilde{\phi}$, the net radial particle flux associated with the drift mode is outwards directed.

4.4 Transition to weakly developed turbulence

In the previous section it was demonstrated that the governing instability in VINETA is the drift-wave instability, characterized by a spatiotemporal mode structure with azimuthal modenumber $m = k_\theta r$. The growth rate of a drift wave with modenumber m can be estimated from the linear dispersion relation (2.53) that depends on external control parameters such as neutral gas pressure p_0 (influencing the collisionality) and the magnetic field B. In the present section the transition from a single coherent drift-wave mode to weakly developed turbulence is characterized. The major control parameter is the ambient magnetic field. In contrast to a single coherent drift-wave mode, weakly developed turbulence is characterized by a broadened azimuthal wavenumber spectrum. Based on the linear dispersion relation (2.25) the influence of the magnetic field B on the growth rate of the drift waves is twofold: First, it enters the dispersion via the drift scale $\rho_s \sim 1/B$. With increasing magnetic field predominantly higher drift-wave modenumbers are destabilized. This is generally observed in VINETA [31]. The drift scale ρ_s is the typical spatial scale for the fluctuations. It decreases with increasing magnetic field. The azimuthal periodic boundary condition, imposed by the cylindrical geometry, allows

for higher modenumbers at smaller ρ_s on an azimuthal circumference. Second, the magnetic field strength enters the linear growth rate via the electron diamagnetic frequency $\omega^\star \sim \nabla_r \ln n_0/B$. For an increasing magnetic field the background density profile n_0 gets steeper (cf. Fig. 4.3), which releases more free energy to drive the drift-wave instability. However, this effect can be balanced by the factor $1/B$ in the definition of $\omega^\star$.

The spatiotemporal dynamics in the radial plasma density gradient, the frequency-modenumber spectrum, and the temporal evolution of the modenumber spectrum obtained from wavelet analysis are shown in Fig. 4.6 for increasing ambient magnetic field. All other external operational parameters are kept fixed (Argon neutral gas pressure $p_0 = 0.27\,\mathrm{Pa}$, *rf*-power $P_{rf} = 1.4\,\mathrm{kW}$). Spatiotemporal density fluctuations are measured with the azimuthal probe array Couronne (cf. Sec. 3.1.1) located in the maximum plasma density gradient at $r = 4\,\mathrm{cm}$.

At low magnetic field $B = 40\,\mathrm{mT}$ the plasma density fluctuations (normalized to standard deviation σ) reveal the presence of a coherent $m = 7$ drift wave mode that propagates in the direction of the electron diamagnetic drift (Fig. 4.6a). The corresponding frequency-modenumber spectrum (Fig. 4.6b) peaks at the azimuthal modenumber $m = 7$ and frequency $\omega/2\pi = 3.1\,\mathrm{kHz}$ (corrected for $\boldsymbol{E}\times\boldsymbol{B}$-Doppler shift). This is in good agreement with the linear dispersion relation $\omega_{\mathrm{lin}} = \omega^\star/(1 + (k_\theta\rho_s)^2)$ which yields

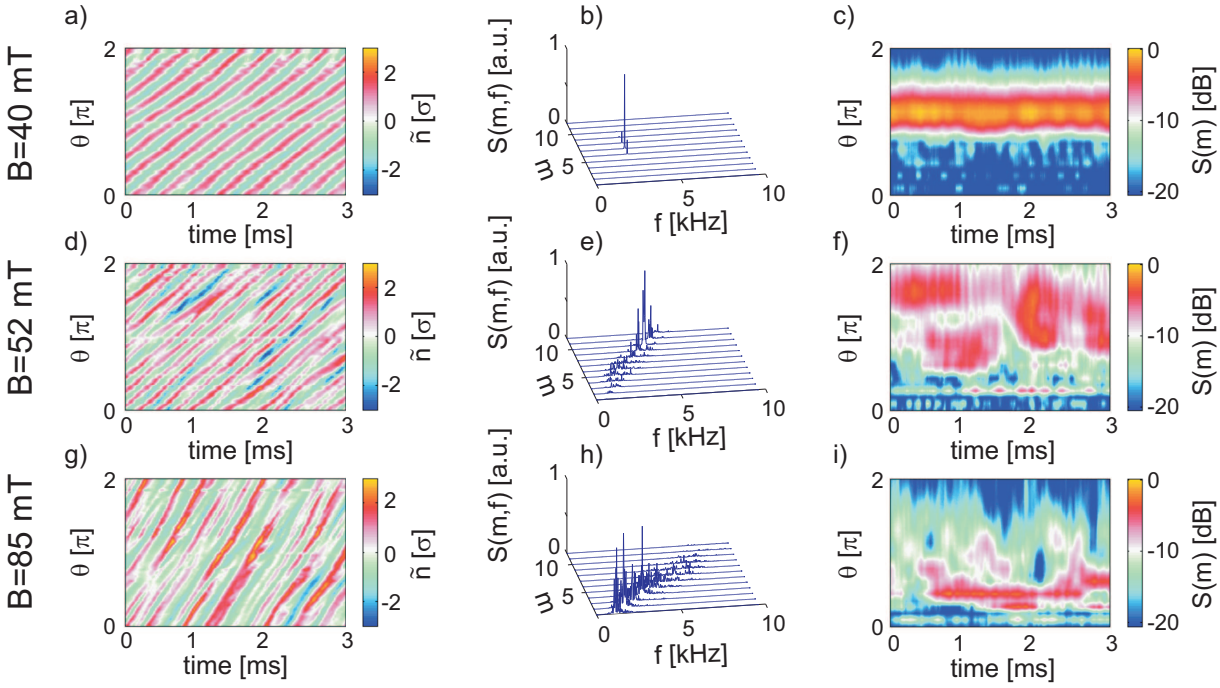

Figure 4.6: Spatiotemporal evolution of density fluctuations in the density gradient region for increasing magnetic field. Couronne measurement on the azimuthal circumference (left column), corresponding frequency-modenumber spectrum (middle column), and time-resolved azimuthal modenumber spectrum (right column).

$\omega_{\mathrm{lin}}/2\pi = 3.7\,\mathrm{kHz}$. The resulting phase velocity of the drift mode is $v_{ph} = \omega/k \approx 95\,\mathrm{m/s}$. The temporal evolution of the modenumber spectrum based on a wavelet decomposition (cf. Fig. 4.6c) confirms the high coherency of the $m = 7$ drift-wave mode.

For higher magnetic field, $B = 52\,\mathrm{mT}$, the dynamical state of the system is getting more complex. The spatiotemporal evolution of the density fluctuations in the density gradient (Fig. 4.6d) is characterized by rapid changes of the fluctuation amplitude and phase velocity. Moreover, no dominant coherent drift-wave mode can be identified. From the frequency-wavenumber spectrum (Fig. 4.6e) it is found that mainly drift waves with modenumbers $m = 6 - 10$ in the frequency range $\omega/2\pi = 3 - 5\,\mathrm{kHz}$ contribute to a broadened frequency and modenumber spectrum. From the temporally resolved modenumber spectrum (Fig. 4.6f) it is observed that, in contrast to the dynamics at $B = 40\,\mathrm{mT}$, not only the dominant modenumber itself, but also its energy changes in time. While the energy in the drift wave modenumber spectrum at $B = 52\,\mathrm{mT}$ is mainly concentrated at high modenumbers, the opposite behavior is observed if the magnetic field is further raised to $B = 85\,\mathrm{mT}$. The density fluctuations in the radial density gradient reveal strong modifications of the fluctuation amplitude and phase velocity similar to the situation for $B = 52\,\mathrm{mT}$ but with larger phase velocity (Fig. 4.6g). The frequency-modenumber spectrum shows contributions from the low-number drift-wave modes with $m = 1 - 4$ at frequencies $\omega/2\pi = 1 - 5\,\mathrm{kHz}$ (Fig. 4.6h). A similar behavior is observed in the temporally resolved modenumber spectrum (Fig. 4.6i). The $m = 3$ is the governing drift-wave mode that is present for a large fraction of the displayed time window. Co-existing drift-wave modes with $m = 2$ and $m = 4 - 7$ are observed as well.

In summary, the variation of the ambient magnetic field B is a robust external parameter to modify in a controlled way the dynamical state of the plasma fluctuations from single linear stable coherent modes (predominantly be found at lower magnetic fields), to a weakly turbulent state (at higher magnetic fields). The turbulent state is characterized by broad frequency and modenumber spectra around $m \leq 10$. The fluctuation energy is not equally distributed over the modenumber spectrum but dominant modes with small modenumbers are generally observed. The latter findings are consistent with experimental observations in the linear CSDX experiment presented recently in Ref. [119]. In the theoretical model (cf. Sec. 2.3), the energy transfer between drift-wave modes due to three-wave interaction is a specific property of the nonlinearity. However, the observation of coexisting drift-wave modes in the temporally resolved modenumber spectra is no proof of wave interaction because the linear growth rate for the various modes may change in time due to a modification of the background density profile n_0. Higher order spectra as the bicoherence analysis (cf. Sec. 3.2.3) allow for a direct investigation of mode coupling.

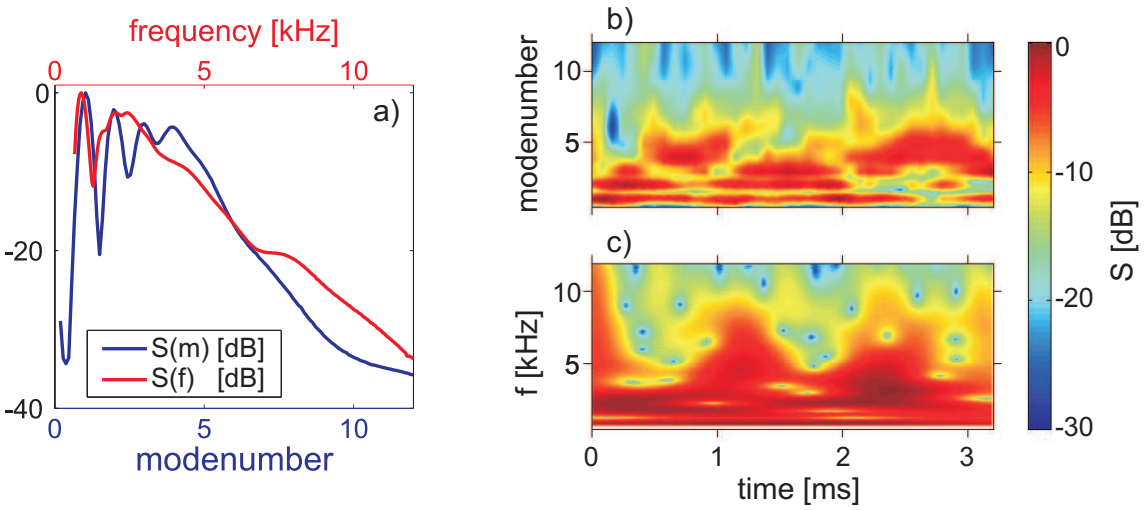

Figure 4.7: Time-averaged wavelet frequency (red) and modenumber (blue) spectra (a), and temporally resolved frequency (b) and modenumber spectra (c) for $B = 75\,\mathrm{mT}$, Argon neutral gas pressure $p_0 = 0.28\,\mathrm{Pa}$ and $P_{rf} = 1.4\,\mathrm{kW}$.

Mode coupling due to three-wave interaction is investigated in detail for a magnetic field strength of $B = 75\,\mathrm{mT}$, Argon neutral gas pressure $p_0 = 0.28\,\mathrm{Pa}$ and $P_{rf} = 1.4\,\mathrm{kW}$. Time-averaged wavelet frequency and wavenumber spectra measured in the maximum density gradient with the azimuthal probe array Couronne are shown in Fig. 4.7c. In the wavenumber spectrum, four distinct peaks at drift-wave modenumbers $m = 1 - 4$ are observed while the frequency spectrum shows only one pronounced peak at $f = 0.9\,\mathrm{kHz}$ and a broad hump in the frequency range $f = 1.5 - 3\,\mathrm{kHz}$. The temporally resolved wavenumber spectrum (cf. Fig. 4.7a) reveals that the $m = 1$ and $m = 2$ mode are present for a large fraction of the displayed time range while higher modenumbers are observed only occasionally. The temporal occurrence of modenumber $m = 4 - 5$ coincides with a decrease of the energy contained in the lower modenumbers, which already indicates the mode transition due to mode coupling. The fine structure of the modenumber spectrum is barely seen in the temporally resolved frequency spectrum (cf. Fig. 4.7b). The reason for that is that a frequency based analysis in the low frequency range of the fluctuations $f < 10\,\mathrm{kHz}$ requires long time intervals. Thus the frequency based analysis is not capable to detect mode coupling on a short time-scale with 0.1 ms typically. As a consequence, the frequency bicoherence barely exceeds the statistical noise level [91; 120]. The mode coupling is investigated by applying a wavenumber based bicoherence analysis. Details of the analysis can be found in Ref. [120]. The temporal evolution of the summed bicoherence is shown in Fig. 4.8a. The statistical noise level is indicated by the dashed line and the total bicoherence b_m^2 always exceeds the noise level. The modenumber bicoherence displays large variations in time, characterized by short bicoherence

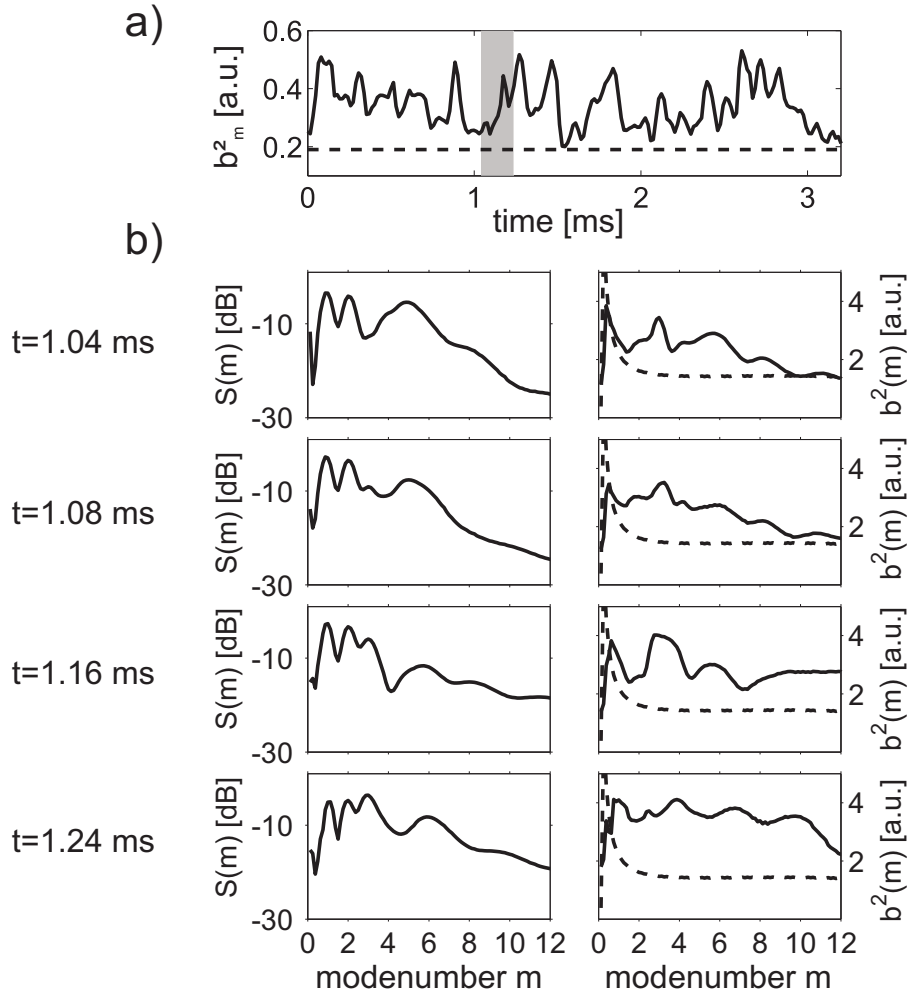

Figure 4.8: (a) Temporal evolution of the total bicoherence b_m^2 for the time displayed in Fig. 4.7b. (b) Modenumber (left) and bicoherence (right) spectra for four discrete times spanning over $t = 1.04 - 1.24$ ms. The time interval is indicated in a) by the gray shaded box.

increases on time scales of typically 0.1 ms, which is much shorter than the typical frequency of the fluctuations (Fig. 4.7b). The shaded box in Fig. 4.8a indicates the time interval $t = 1.04 - 1.24$ ms for which mode coupling is investigated in detail. At the beginning of the bicoherence increase the modenumber spectrum is dominated by modes $m = 1, 2, 5$ (Fig. 4.8, $t = 1.04$ ms). The modenumber bicoherence shows a peak at $m = 3$ that does not exist in the modenumber spectrum at this time. The resonance condition ${}^1k_\theta + {}^2k_\theta = {}^3k_\theta$ yields that the peak in the modenumber bicoherence is either based on coupling between $m = 1$ and $m = 2$ or $m = 2$ and $m = 5$. For subsequent times the modenumber bicoherence still peaks at $m = 3$ and also a peak at $m = 3$ in the modenumber spectrum evolves. In other words, from the bicoherence spectrum at $t = t_0$ it can be derived how the modenumber spectrum at $t = t_0 + \Delta t$ evolves. After the modenumber bicoherence at $m = 3$ reaches its maximum value at $t = 1.16$ ms the $m = 3$ drift-wave

mode becomes the dominant peak in the modenumber spectrum at $t = 1.24\,\mathrm{ms}$. Thus mode coupling is a possible mechanism to explain the sporadic occurrence of spatiotemporal structures associated with drift-wave modes. However the presented bicoherence analysis is not capable to give direct insight into the direction of the energy transfer, since several drift-wave modes are present that allow a variety of coupling scenarios that fulfill equally well the resonance condition.

5

Intermittent transport events

Already the early investigations of the drift-wave instability and drift-wave turbulence were motivated by the related fluctuation-induced transport. The principle of the transport mechanism is schematically illustrated in Fig. 5.1. A density perturbation (blue) and potential perturbation (red) are oriented perpendicular to the ambient magnetic field B. The electric field associated with the potential perturbation gives rise to an $\boldsymbol{E}\times\boldsymbol{B}$-rotation of the potential eddy (counterclockwise in this representation). If density and potential perturbations are in phase $\delta(\tilde{n},\tilde{\phi}) = 0$ (Fig. 5.1a), as in the case of adiabatic electron response, the density advected by the potential eddy to the left equals the density advected by the potential eddy to the right such that the resulting net radial particle flux is zero. For a non-zero phase shift $\delta(\tilde{n},\tilde{\phi}) \neq 0$ an imbalance of plasma density advected by the eddy occurs and higher plasma density is advected to the left than to the right in Fig. 5.1b resulting in a net radial particle flux with a maximum for $\delta(\tilde{n},\tilde{\phi}) = \pi/2$.
As shown in Sec. 4.3 a coherent drift wave has a small phase shift ($\delta(\tilde{n},\tilde{\phi}) \approx 0.1-0.15\pi$) and the density perturbation is ahead of the potential perturbation. Consequently, the net radial particle flux is directed radially outwards down the radial plasma density gradient.

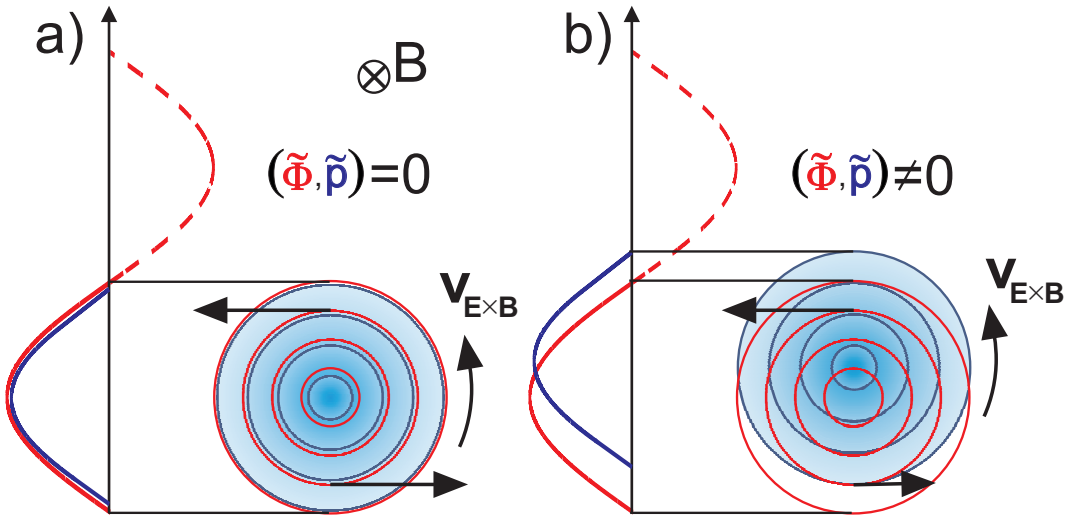

Figure 5.1: Schematic illustration of fluctuation induced transport.

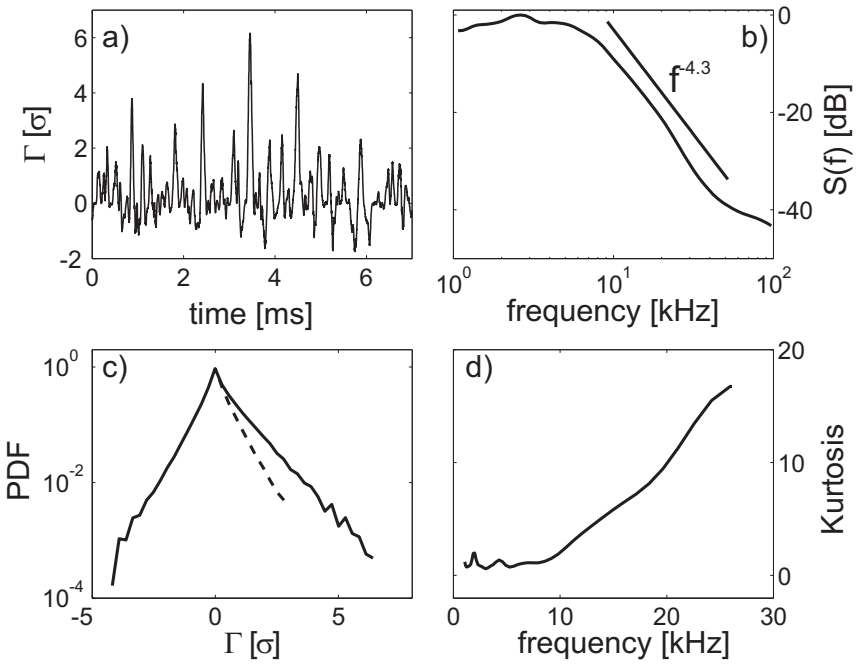

Figure 5.2: (a) Time-series of the fluctuation-induced radial particle flux $\tilde{\Gamma}$ normalized to standard deviation σ (positive amplitudes correspond to a flux directed radially outwards), (b) corresponding wavelet frequency spectrum, (c) probability distribution function (PDF) and (d) evolution of the kurtosis for increasing frequency.

The fluctuation-induced particle flux, written in Fourier representation [121] as

$$\tilde{\Gamma} = \frac{1}{B}\tilde{n}\tilde{E}_\theta = 2k_\theta|\tilde{n}_k||\tilde{\phi}_k|\sin\left(\frac{\delta(\tilde{n},\tilde{\phi})}{B}\right) \tag{5.1}$$

can be experimentally measured using a triple probe (cf. Sec. 3.1.1). The main characteristics of the measured particle flux $\tilde{\Gamma}$ in weakly developed drift-wave turbulence in VINETA are compiled in Fig. 5.2. The time series of the radial particle flux $\tilde{\Gamma}$ in the maximum plasma density gradient normalized to standard deviation σ is shown in Fig. 5.2a, where positive values correspond to a particle flux directed radially outwards. The particle flux is strongly asymmetric. It has a non-zero positive mean and is characterized by short positive bursts with high amplitudes reaching $\tilde{\Gamma} \approx 6\,\sigma$. The wavelet frequency spectrum (Fig. 5.2b) shows remnants of drift-wave modes in the frequency range $f = 2 - 4\,\mathrm{kHz}$. A $f^{-\alpha}$-decay for higher frequencies ($f > 8\,\mathrm{kHz}$) is observed with a spectral exponent of $\alpha = 4.3$. The observation of asymmetric fluctuations of the radial particle flux $\tilde{\Gamma}$ is confirmed by the PDF (Fig. 5.2c). The PDF is peaked and skewed towards positive amplitudes of $\tilde{\Gamma}$ with skewness $s = 1.26$ and kurtosis $K = 8.3$. Note that the non-Gaussian distribution of $\tilde{\Gamma} = \tilde{n}\tilde{E}_\theta/B$ is not necessarily related to a non-Gaussian distribution of

either $\tilde{n}$ or $\tilde{E}_\theta$ [122]. Even if the fluctuations of plasma density $\tilde{n}$ and poloidal electric field $\tilde{E}_\theta$ are Gaussian-distributed (where $K = 0$ and $s = 0$) the product $\tilde{\Gamma} = \tilde{n}\tilde{E}_\theta/B$ may exhibit a peaked distribution with a kurtosis

$$K = 3\frac{3 + 14\gamma^2 + 3\gamma^4}{(1+\gamma^2)^2} - 3 > 0, \tag{5.2}$$

where γ is the cross-correlation amplitude of $\tilde{n}$ and $\tilde{E}_\theta$. For the present data the maximum cross-correlation amplitude is $\gamma = 0.3$ resulting in a calculated kurtosis of $K = 7.7$, which is close to the experimentally observed value of $K = 8.3$.

The sporadic occurrence of high amplitude bursts of the radial particle flux $\tilde{\Gamma}$ is usually considered as intermittency. As outlined in Ch. 1, for an intermittent signal the kurtosis is expected to grow without bound for increasing frequency. A wavelet decomposition of the particle flux for the spectral range of the drift-wave fluctuations ($f < 30\,\text{kHz}$) has been done and the kurtosis K for increasing frequency is shown in Fig. 5.2d. Its value increases from $K \approx 1$ at $f = 1\,\text{kHz}$ to $K \approx 17$ at $f = 28\,\text{kHz}$. This behavior demonstrates that the fluctuation-induced transport is indeed intermittent and characterized by sporadic high-amplitude transport events.

5.1 Formation and propagation of spatiotemporal turbulent structures

In the weakly-developed drift-wave turbulence on VINETA the character of the plasma density fluctuations changes across the radial plasma density profile. While in the radial plasma density gradient quasi-coherent oscillations of the plasma density are observed, which are related to remnants of drift-wave modes, the plasma density fluctuations in the plasma edge region are governed by intermittent positive density bursts with high amplitudes similar the fluctuating radial particle flux (cf. Fig. 5.2a). In the following sections it is demonstrated that the density bursts in the plasma edge are associated with spatiotemporal turbulent structures originating in the density gradient region and propagating radially outwards with typical radial velocities of $10\,\%\, c_s$ in agreement with observations in other linear plasma devices [123].

5.1.1 Time-averaged profiles and temporal evolution of plasma density fluctuations

The (time-averaged) radial plasma density and plasma potential profiles are shown in Fig. 5.3a. Both have a Gaussian shape but with different $1/e$–folding lengths (46 mm for the plasma density and 169 mm for the plasma potential profile). Fig. 5.3b shows the modulus of the azimuthal $\boldsymbol{E}\times\boldsymbol{B}$-drift $v_{\mathrm{E\times B}} \sim -\nabla_r\phi$ and the electron diamagnetic drift $v_{d,e} \sim \nabla_r \ln n$ as calculated from the exponential fits to the profiles. The electron diamagnetic drift velocity $v_{d,e}$ has a peak value of 2.1 km/s in the region of maximum plasma density gradient at $r = 61$ mm and decreases towards plasma edge and center. Due to the different shapes of the density and potential profiles, the electron diamagnetic drift dominates over the $\boldsymbol{E}\times\boldsymbol{B}$-drift in the plasma bulk. At a certain radial position ($r = 82$ mm) the $\boldsymbol{E}\times\boldsymbol{B}$-drift exactly balances the electron diamagnetic drift, such that the effective drift velocity is zero (note that both drift-velocities are in opposite directions). In the far plasma edge, only the $\boldsymbol{E}\times\boldsymbol{B}$-drift contributes significantly to the total drift. The $\boldsymbol{E}\times\boldsymbol{B}$-drift velocity has a maximum value of 1.5 km/s at $r = 124$ mm and decreases towards smaller and larger radii.

Three main regions can be distinguished (Figs. 5.3a and 5.3b): Region A is in the density gradient region, where the electron diamagnetic drift dominates. Region B is the plasma edge, where the density drops down to below 7 % of the peak density and the effective drift almost vanishes. In the far plasma edge C, the time-averaged density further decreases to below 4 % of the peak density and the drift is governed by the $\boldsymbol{E}\times\boldsymbol{B}$-velocity. For a characterization of the temporal evolution of turbulent density fluctuations measurements were done at positions A, B, and C. The results are depicted in Fig. 5.4. Shown are the density fluctuation time series normalized to standard deviation $\tilde{n}/\sigma$, the prob-

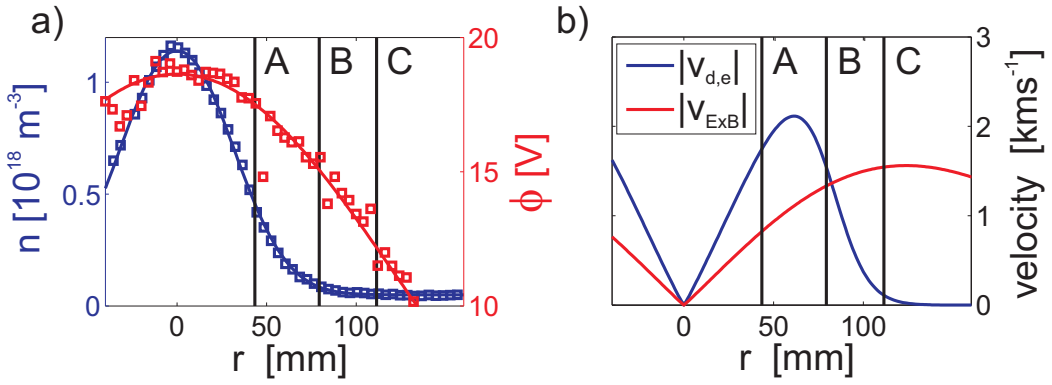

Figure 5.3: (a) Radial plasma density (blue) and plasma potential (red) profile. (b) Modulus of the perpendicular drift velocities electron diamagnetic drift (blue) and $\boldsymbol{E}\times\boldsymbol{B}$-drift (red) as calculated from the fits to the data shown in (a).

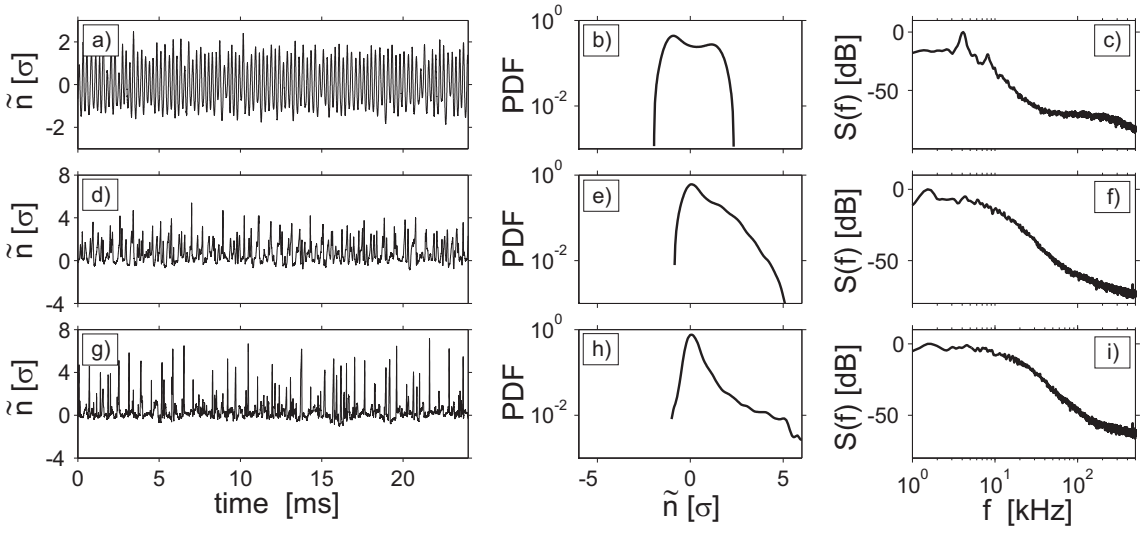

Figure 5.4: Time series of density fluctuations, probability distribution function (PDF) and frequency power spectra at radial positions A (a-c), B (d-f) and C (g-i) as indicated in Fig. 5.3a.

ability distribution function (PDF), and frequency power spectra $S(f)$. The statistical character of the plasma density fluctuations changes significantly across the radial plasma density profile: In the region of maximum density gradient (position A, Fig. 5.4a-c), coherent density fluctuations with relatively low amplitude ($\tilde{n}/\sigma \leq 2$) are observed. This is confirmed by the frequency power spectrum, which peaks at a frequency of $4.1\,\mathrm{kHz}$; for higher frequencies ($f > 8\,\mathrm{kHz}$) a power-law decrease is observed. The PDF is symmetric and double-humped, as expected for sinusoidal fluctuations. The density fluctuations in the plasma edge (position B, Fig. 5.4d-f) have an intermittent character with positive density bursts of peak amplitudes $\tilde{n}/\sigma \sim 5$. The fluctuations are asymmetric, and the peaked PDF has a pronounced positive tail. This is quantified by the PDF skewness $s = 1.1$ and kurtosis $K = 1$. The frequency power spectrum is broader and no pronounced peak is observed. However, the occurrence of the positive density bursts is not completely random in time but is centered around a characteristic time scale, which results in a broadened small peak at $f = 1.3\,\mathrm{kHz}$. The intermittent character of the density fluctuations further increases towards the far edge (position C, Fig. 5.4g-i). Here the time-averaged density almost vanishes. Positive density bursts are observed with normalized amplitudes up to $\tilde{n}/\sigma \sim 7$. The corresponding PDF is asymmetric and strongly peaked with skewness $s = 2.9$ and kurtosis $K = 11$. The frequency power spectrum shows a power law decrease for frequencies $f \geq 10\,\mathrm{kHz}$ and no pronounced peaks are observed.

Comparing the amplitudes of the density fluctuations at positions A and B (Fig. 5.5), it is found that although the fluctuation level is considerably higher, the positive density bursts in the plasma edge region have a similar amplitude as the density fluctuations in the region of maximum plasma density gradient. This is already a strong indication that

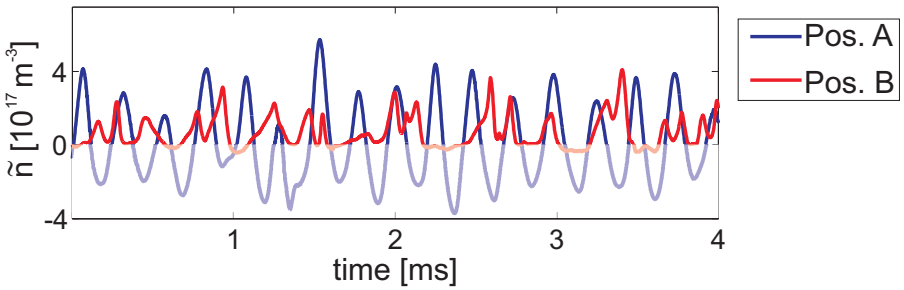

Figure 5.5: Absolute amplitude of density fluctuations in the radial plasma gradient region (Pos. A) and plasma edge region (Pos. B).

the density bursts observed in the plasma edge actually originate from the radial density gradient region and propagate radially outwards (downwards the density gradient).
As already mentioned, the frequency spectra measured at position B shows a peak at $f = 1.3\,\mathrm{kHz}$ (cf. Fig. 5.4f). To relate the occurrence of the density events to the frequency spectrum, the temporal distribution of events in the density fluctuation time series at the plasma edge (position C) is determined by detecting the time instant of each fluctuation peak that meets a predefined amplitude condition (an amplitude window of 5% is imposed to increase the number of detected events). After averaging over the time delay between two consecutive events one obtains a burst "frequency", related to the respective amplitude condition. Fig. 5.6 shows the so-obtained burst frequency for increasing amplitude condition $p = 1 - 5\,\sigma$. The error bars represent the standard deviation of the frequency distributions. For smaller amplitudes $p \leq 1\,\sigma$, noise-like small amplitude fluctuations contribute dominant to the measured frequencies, leading to a wide spread of frequencies and thereby to large error bars. However, the occurrence of large-amplitude bursts ($p \geq 1\sigma$) is not completely random but corresponds to a characteristic frequency range of 0.5-1 kHz. This is particularly evident for the largest amplitude bursts, for which the error bars are mainly determined by the relatively small numbers of detected events (only 40

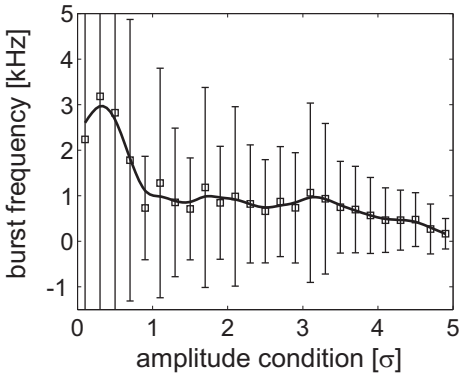

Figure 5.6: Frequency of positive density bursts in the far plasma edge (pos. C in Fig. 5.3a).

detected events for an amplitude condition of $p = 3\,\sigma$) and not by a larger velocity spread.

5.1.2 Spatiotemporal evolution of plasma density fluctuations

To understand the relation between radial fluctuation-induced convective particle flux and turbulent structure propagation across the axial magnetic field, measurements of density fluctuations in the entire azimuthal cross-section have been performed. The reconstruction of the spatiotemporal density fluctuations in the azimuthal plane is done by applying the conditional average (CA) method described in Sec. 3.2.4. Two reference positions are located in the maximum density gradient region (position A in Fig. 5.3) and in the plasma edge (position B in Fig. 5.3). The result of the CA analysis for the reference probe located in the maximum density gradient region (position A) is shown in Fig. 5.7 for three different time lags τ, spanning over the range $\tau = -104 \ldots 4\,\mu$s.

A quasi-coherent $m = 1$ drift wave mode dominates the conditional average density fluctuations. The peak fluctuation amplitude of the mode is located in the maximum gradient region. The mode propagates purely azimuthally in the direction of the electron diamagnetic drift (clockwise in Fig. 5.7). No radial component for the mode propagation is observed. The azimuthal phase velocity of the mode is $v_{ph} \approx 0.9\,$km/s, a factor of 1.2 smaller than the $\boldsymbol{E}\times\boldsymbol{B}$ Doppler-shifted electron diamagnetic velocity. The linearized drift-wave dispersion relation as derived from the Hasegawa-Mima model (2.25)

$$\omega = \omega^\star/(1 + (k_\perp \rho_s)^2)$$

yields for the observed $m = 1$ mode with $k_\perp = 0.29\,\mathrm{cm}^{-1}$ and $\rho_s = 1.86\,$cm a mode frequency of $\omega_{(m=1)} = \omega^\star/1.3$, which is in excellent agreement with the observations.

In addition to the actual drift mode structure, a specific event is observed for the time lag

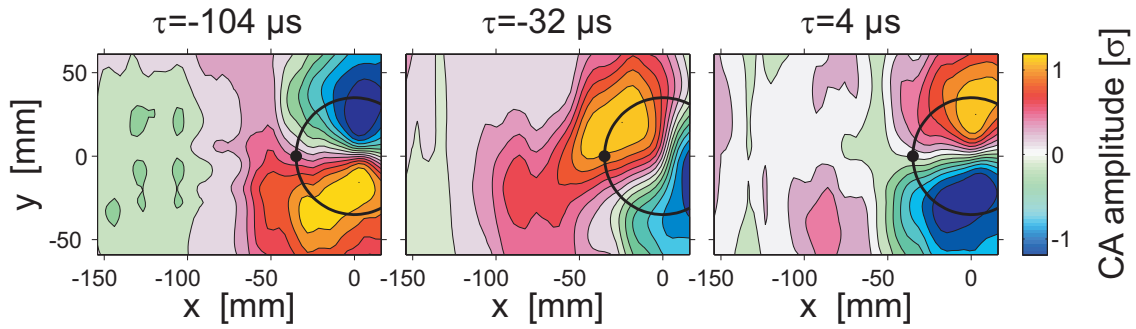

Figure 5.7: Conditionally averaged (CA) density fluctuations in the azimuthal plane for three different time lags τ . The reference probe (indicated by a black dot) is located in the maximum density gradient region. The amplitude condition was chosen to be $p = \sigma/2$. The CA amplitude is normalized to standard deviation σ. The black circle denotes the purely azimuthal direction.

τ=-32 μs. A turbulent density fluctuation structure peels radially off the drift mode structure and propagates into the plasma edge. The turbulent structure propagates opposite to the $m = 1$ drift mode, due to the local dominance of the $\boldsymbol{E}\times\boldsymbol{B}$-velocity over the electron diamagnetic drift velocity (cf. Fig. 5.3b). Since the reference signal is located at the drift mode structure the turbulent structure must be coherently related. The turbulent structure is azimuthally distorted with an azimuthal extent of $\Delta y \approx 60\,\mathrm{mm}$ and a radial extent of $\Delta x \approx 50\,\mathrm{mm}$. With $0.8\,\sigma$ its peak amplitude is slightly smaller than the mode structure amplitude. Note that the formation process of the turbulent structure occurs in a region where the azimuthal velocity has a strong radial shear (cf. Fig. 5.3b).

To investigate specifically the spatiotemporal dynamics of the turbulent structure, the CA procedure is repeated with the reference signal recorded in the plasma edge (position B in Fig. 5.3). The result is shown in Fig. 5.8 for four different time lags $\tau = 40 \ldots 40\,\mu$s. The CA amplitude condition is now chosen to be $p = 3\,\sigma$ in order to extract the positive high-amplitude density fluctuations. A propagating coherent turbulent structure is clearly observed in the plasma edge. Its amplitude exceeds six times the time average density, indicating a strong transport event. In contrast to the coherent $m = 1$ mode (Fig. 5.7), the turbulent structure propagates in $\boldsymbol{E}\times\boldsymbol{B}$-drift direction, opposite to the the electron diamagnetic drift. The correlation length is estimated from a cross-correlation analysis. One obtains $l_{\mathrm{corr,pol}} \approx 70\,\mathrm{mm}$ in azimuthal direction and $l_{\mathrm{corr,rad}} \approx 50\,\mathrm{mm}$ in radial direction. An analysis of the correlation time τ_c of the turbulent structure turned out to be not possible due to the spatial limitation of the measurement in the azimuthal plane. From the results shown in Fig. 5.8, only a lower limit of $\tau_c > 150\,\mu$s could be estimated. However, the trajectory of the structure is not anymore purely azimuthal (indicated by the dashed circle in Fig. 5.8) but has a significant radial component. The azimuthal and radial propagation velocities are analyzed in detail by tracking the turbulent structure over the two-dimensional

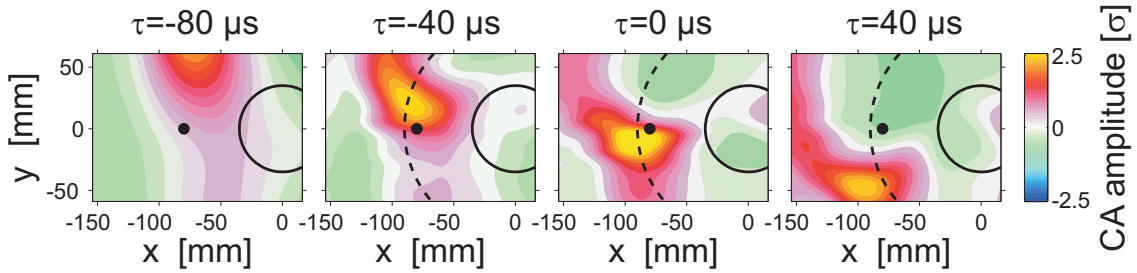

Figure 5.8: Conditionally averaged density fluctuations for four different time lags τ in the azimuthal plane. The amplitude condition for the reference probe which is located in the plasma edge (r=-80 mm, indicated by the black dot), was chosen to $p = 3\,\sigma$. The CA amplitude is normalized to standard deviation. The black solid circle corresponds to the one in Fig. 5.7. The black dashed line indicates the azimuthal direction.

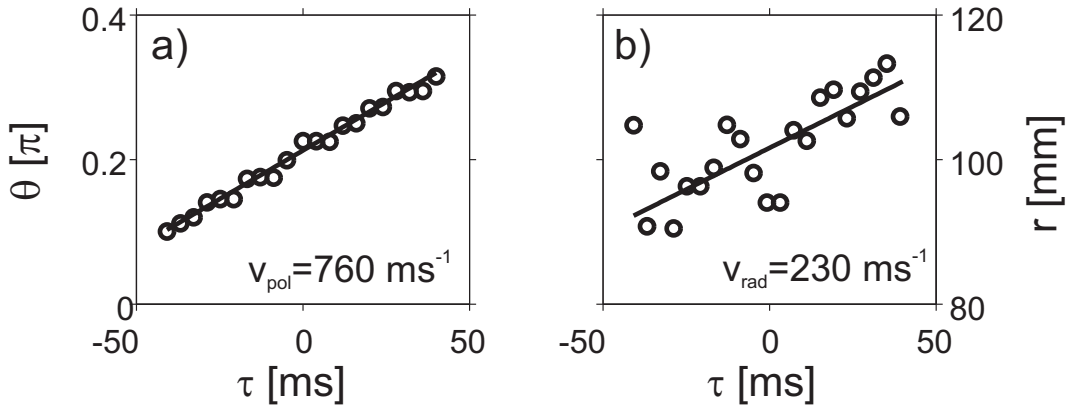

Figure 5.9: Azimuthal (a) and radial velocity (b) of the turbulent coherent structure observed in Fig. 5.8.

domain for time lags $\tau = -40 \ldots 40\,\mu$s in steps of $\Delta\tau = 4\,\mu$s. Only the high-amplitude area of the structure with amplitudes exceeding $80\,\%$ of the peak value is considered. The center-of-mass position of this area is tracked through the domain and the resulting positions are decomposed in azimuthal angle θ and radial displacement r. The result of the tracking is shown in Fig. 5.9. It yields the azimuthal and radial structure velocities, $v_{\mathrm{pol}} = \Delta\theta/\Delta\tau$ and $v_{\mathrm{rad}} = \Delta r/\Delta\tau$, respectively. The averaged velocities are obtained from a linear fit to the azimuthal and radial positions. A constant azimuthal velocity of $v_{\mathrm{pol}} = 760\,$m/s is found for all analyzed time instants in Fig. 5.9.a. This corresponds to a rotation frequency of $f_{\mathrm{pol}} = 1.35\,$kHz, which is in good agreement with the burst frequency of the high-amplitude density fluctuations (cd. Fig. 5.6). The estimated azimuthal velocity v_{pol} is roughly $50\,\%$ of the local $\boldsymbol{E}\times\boldsymbol{B}$-velocity $\boldsymbol{v}_{E\times B} = 1.42\,$km/s. A possible explanation for this deviation is a non-negligible contribution of the electron diamagnetic drift-velocity, which lowers the effective azimuthal velocity to $v_{\mathrm{pol,eff}} = 572\,$m/s, which agrees roughly with the experimental value $v_{\mathrm{pol}} = 760\,$m/s.

Although the scatter in the radial velocities (Fig. 5.9b) is larger, an averaged radial structure velocity of $v_{\mathrm{rad}} = 230\,$m/s can be obtained, corresponding to $\approx 10\%\, c_s$ (with c_s being the local ion sound speed). Note that v_{rad} is a factor of 3.5 smaller than v_{pol} and the structure performs a "spiral" motion in the azimuthal plane. During propagation the structure is distorted and develops a tail in the plasma edge ($x \leq -130\,$mm), which lags behind the actual structure. The distortion is the direct result of the radial shear of the $\boldsymbol{E}\times\boldsymbol{B}$-drift in the far plasma edge (cf. Fig. 5.3b). Consequently, the tail propagates with a smaller azimuthal velocity and the structure smears out to form a spiral. It is worthwhile to note that the radial velocity of the turbulent structure of $v_{\mathrm{rad}} = 230\,$m/s corresponds to a radial displacement of $\Delta r = 17\,$cm during one azimuthal turn, such that every turbulent structure is detected only once within the azimuthal plane covered by the diagnostics.

More insight must be gained into first the driving mechanism of the turbulent structure's peel-off process from the quasi-coherent drift-wave mode in the maximum plasma density gradient region and second the radial propagation of the turbulent structure in the plasma edge. For that measurements of the space-time history of the potential fluctuations that are associated with the density structure have been done. The result of the CA analysis (reference probe located in the radial plasma density gradient, position A) is shown in Fig. 5.10a for a discrete time lag $\tau = -60\,\mu$s. The conditionally averaged density fluctuations $R_{CA}(\tilde{n}, \tilde{n})$ are shown color-coded. For simplicity only the positive potential fluctuations $R_{CA}(\tilde{n}, \tilde{\phi} > 0)$ are superimposed as contour lines. Since the quasi-coherent $m = 1$ drift mode propagates clockwise (cf. Fig. 5.7) the potential perturbation lags behind the density perturbation. An azimuthal cut through the positive potential and density perturbation along a chosen trajectory (indicated by the dashed line in Fig. 5.10a) is shown in Fig. 5.10c, where θ_0 is the azimuthal position of the maximum density perturbation. The azimuthal displacement of the density and potential structure corresponds to a phase shift of $\delta(\tilde{n}, \tilde{\phi}) \approx \pi/2$. This phase shift results in a radially outwards directed

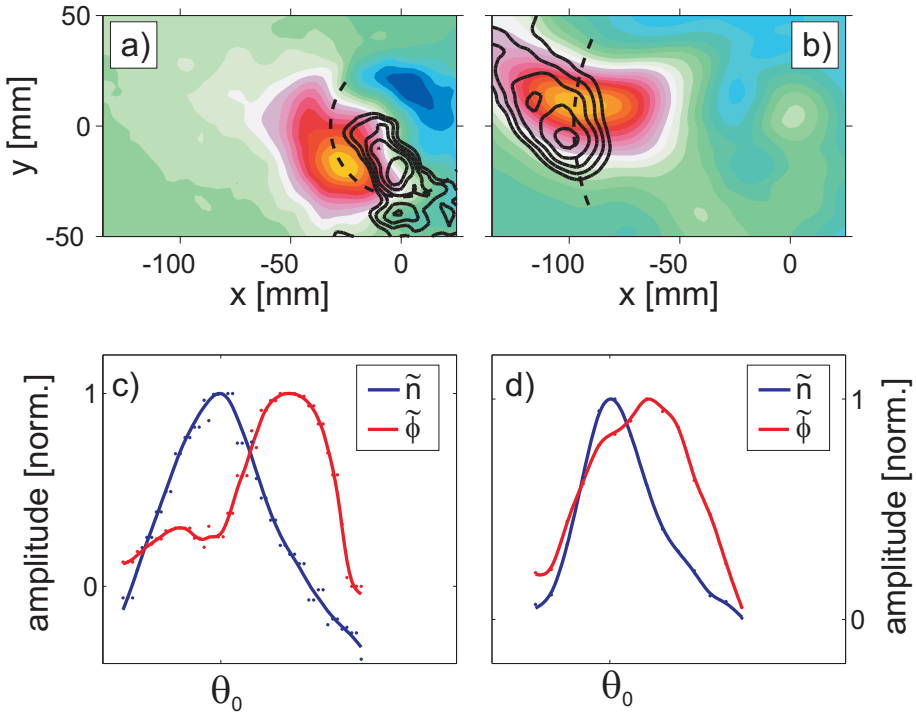

Figure 5.10: CA amplitude of plasma density fluctuations $R_{CA}(\tilde{n}, \tilde{n})$ (color-coded) and positive plasma potential fluctuations $R_{CA}(\tilde{n}, \tilde{\phi} > 0)$ (superimposed as contour lines) for the reference probe located in the radial plasma density gradient (position A). (b) Same as (a) but for the reference located in the plasma edge (position B). (c, d) Cut through the normalized $\tilde{n}$ and $\tilde{\phi} > 0$ structures along the azimuthal trajectory in terms of angle θ for the situation depicted in (a) and (b). The cut is indicated in (a) and (b) as dashed line.

particle flux $\tilde{\Gamma}$. Hence, the positive density perturbation is advected radially outwards, which is in agreement with the peel-off process of the turbulent structure from the quasi-coherent $m = 1$ drift-wave mode, as observed in Fig. 5.7.

The conditionally averaged density fluctuations $R_{CA}(\tilde{n}, \tilde{n})$ (color-coded) and positive potential fluctuations $R_{CA}(\tilde{n}, \tilde{\phi} > 0)$ (superimposed as contour lines) for the reference probe located in the plasma edge (position B) are shown in Fig. 5.10b. Density and potential perturbation are phase-shifted, but in contrast to the maximum density gradient region, the potential perturbation is ahead of the density perturbation since the propagation in the plasma edge is determined by the $\boldsymbol{E}\times\boldsymbol{B}$-drift, corresponding to a counter-clockwise azimuthal propagation (cf. Fig. 5.8). However, the associated fluctuating electric field $\tilde{E}_\theta$ leads to a $\tilde{E}_\theta \times B$-drift, which is directed radially outwards. An azimuthal cut through the density and potential structure along a chosen trajectory (indicated in Fig. 5.10b by the dashed black line) is shown in Fig. 5.10d. Due to the broad distribution of the potential perturbation, a quantitative analysis of the phase shift is difficult to do, but the bounds $0 < \delta(\tilde{n}, \tilde{\phi}) < \pi/2$ are observed for the central part of the density perturbation.

Based on the cut along the azimuthal trajectory of the turbulent structure in the plasma edge (Fig. 5.10d), the fluctuation-induced advection velocity $\tilde{v}_{E\times B}$ can be estimated. The result is shown in Fig. 5.11. The normalized density perturbation $\tilde{n}$ associated with the turbulent structure is shown as a red line and the phase-shifted positive potential perturbation $\tilde{\phi}$ as a blue line. The radial $\boldsymbol{E}\times\boldsymbol{B}$-velocity $\tilde{v}_{E\times B} = -\nabla_\theta \tilde{\phi}/B$ as calculated from the azimuthal profile of the potential perturbation is shown as the black line. Note that $\tilde{v}_{E\times B} > 0$ corresponds to a drift directed radially outwards. The main fraction of the density perturbation is advected radially outwards. A quantitative comparison with the

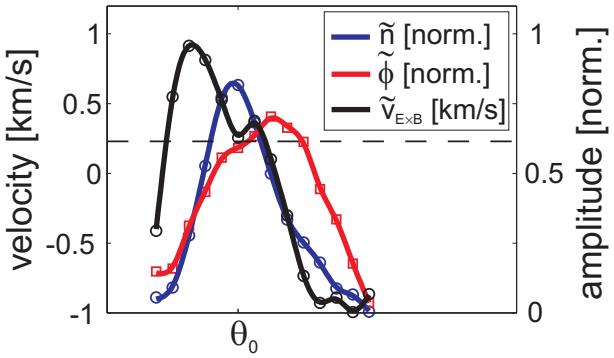

Figure 5.11: Normalized plasma density fluctuations $\tilde{n}$ (blue) and normalized positive plasma potential perturbations $\tilde{\phi}$ (red) associated with the turbulent structure in the plasma edge along the azimuthal cut shown in Fig. 5.10b as dashed line. The advection velocity $\tilde{v}_{E\times B}$ calculated from the azimuthal run of the potential is shown as the black line, where positive values correspond to a radial outward propagation. For comparison the dashed line shows the radial velocity of the turbulent structure as obtained from structure tracking (Fig. 5.9).

radial velocity of the turbulent structure (Fig. 5.9) yields excellent agreement: The experimentally observed radial velocity of the turbulent structure is $v_{\rm rad} = 230\,$m/s (indicated in Fig. 5.11 by a dashed line) and the calculated radial advection velocity approaches the same value in the region where the amplitude of the density perturbation peaks. However, the advection velocity $\tilde{v}_{E\times B}$ exhibits large variations across the density perturbation. If the position of the $1/e$ amplitude of the density perturbation is considered as the reference, the value of the advection velocity $\tilde{v}_{E\times B}$ varies between $-400\,$m/s and $910\,$m/s.
The fluctuation-induced perpendicular particle flux $\tilde{\Gamma}_{\perp}^{\rm burst} =< n_{\rm burst}\, v_{\rm rad} >$, caused by large-amplitude turbulent structures with $\tilde{n}_{\rm burst}/\sigma > 3$, can be compared to the parallel particle flux $\Gamma_{\parallel} =< n_0\, c_s >$ towards the end plate at $x = -90\,$mm. One finds that the parallel flux still dominates the transport by several orders of magnitude, $\tilde{\Gamma}_{\perp}^{\rm burst}/\Gamma_{\parallel} \approx 6{\cdot}10^{-4}$. Thus the radially propagating fluctuation structures are strongly damped by parallel transport and do not contribute to a significant broadening of the time-averaged plasma density profile.

5.2 Limiter operation

The analysis of the space-time history of fluctuating structures in weakly developed drift-wave turbulence, as presented in the previous sections, revealed the existence of a quasi-coherent $m = 1$ drift-wave mode propagating in the maximum radial density gradient region. To drive the plasma into a fully developed drift-wave turbulence state, one approach is to increase the radial density gradient, i.e., to decrease the radial density gradient length $L_{\perp} = |\nabla \ln n_0|^{-1}$. The density gradient length enters directly into the growth rate of the drift-wave modes via the the electron diamagnetic drift (2.53). To achieve this an azimuthally symmetric limiter (annulus) was introduced into the VINETA plasma. A schematic illustration of the limiter operation is shown in Fig. 5.12. It shadows the entire azimuthal cross-section of the magnetized plasma column, except for a circular area with radius $r_l = 2\,$cm. The limiter extends 20 cm and is aligned parallel to the magnetic field.

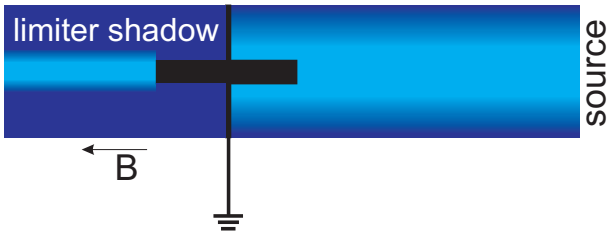

Figure 5.12: Schematic illustration of the annulus limiter operation which shadows the entire azimuthal plasma crosssection.

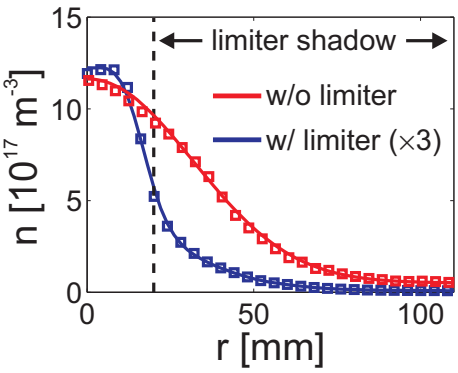

Figure 5.13: Radial profiles of plasma density with and without limiter operation. The profile without limiter is the same as shown in Fig. 5.3a. The dashed line corresponds to the edge of the annulus limiter.

The limiter length is larger than the mean free path of ionizing collisions of the neutral Argon atoms $\lambda_{\text{ion}} = v_{th,0}/n \langle \sigma_{ion} v_{th,e} \rangle = 10\,\text{cm}$ for the present plasma parameters.
A comparison of the radial plasma density profiles with and without applied limiter is shown in Fig. 5.13. With limiter, the peak plasma density in the center is $4 \cdot 10^{17}\,\text{m}^{-3}$, much smaller than without limiter. However, the density gradient length decreases from $L_\perp = 0.02\,\text{m}^{-1}$ without limiter to $L_\perp = 0.009\,\text{m}^{-1}$ with limiter. The increased drive of the drift waves in limiter operation is partly compensated by a systematic decrease of the peak electron temperature ($T_e \approx 3\,\text{eV}$ without limiter and $T_e \approx 2\,\text{eV}$ with limiter).
A comparison of the modenumber spectra at the position of the maximum radial density gradient with and without limiter is shown in Fig. 5.14. The temporally resolved wavelet modenumber spectrum shown in Fig. 5.14a corresponds to the discharge without limiter, analyzed in Sec. 5.1. In good agreement with the results of the previous section, the quasi-coherent $m = 1$ drift-wave mode turns out to be the dominant mode. Occasionally higher modenumbers $m = 2$ and $m = 3$ occur, but typically with significantly smaller energy. The situation changes in the limiter operation (Fig. 5.14b): The $m = 1$ drift

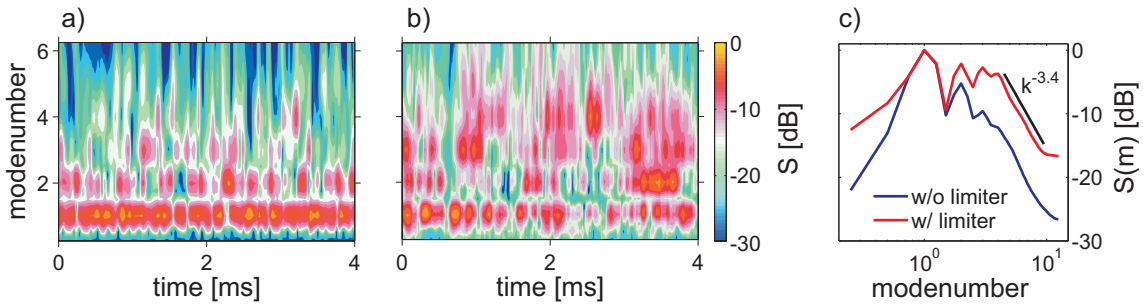

Figure 5.14: (a) Temporally resolved wavelet modenumber spectra in the radial density gradient without limiter and (b) with limiter. Time-averaged modenumber spectra for both situations are shown in (c).

wave is still the dominant mode but its coherency drops significantly. The $m = 1$ mode appears on typical time scales of $0.2\,\text{ms}$ but then its energy decreases and at the same time the energy of higher modenumbers with $m = 2, 3, 4, 5$ increases. An estimate of the correlation time of the density fluctuations in the maximum density gradient region yields the value $\tau_c = 220\,\mu\text{s}$, which is in agreement with the typically observed duration of the $m = 1$ drift-wave mode. The corresponding time-averaged modenumber spectra for both regimes are shown in Fig. 5.14c. They are consistent with the above findings, i.e., more energy is contained in the higher modenumbers if the limiter is introduced. In both cases, the power spectrum decays for modenumbers $m > 5$ with a spectral index of $\alpha = 3.4$ is observed, which agrees well with numerical simulations of drift-wave turbulence ($\alpha \approx 3$, cf. Sec. 2.4). In summary, the introduced limiter allows one to steepen the radial density gradient. As a result the coherency of the turbulent fluctuations can be significantly reduced, indicating a more developed turbulence due to the stronger drive.

5.2.1 Temporal evolution of plasma density fluctuations

Fig. 5.15 shows the temporal behavior of the density fluctuations measured at three different radial positions, corresponding to the maximum density gradient region (position A, $r = 20\,\text{mm}$), the plasma edge (position B, $r = 50\,\text{mm}$) and the far plasma edge (position C, $r = 80\,\text{mm}$). In the maximum plasma density gradient region (Fig. 5.15a) turbulent fluctuations with peak amplitudes of $3\,\sigma$ are observed. The PDF is symmetric almost Gaussian with skewness $s = 0.3$ and kurtosis $K = -0.15$. In the frequency spectrum (Fig. 5.15c) no pronounced peaks are observed and for $f > 11\,\text{kHz}$ the spectrum follows

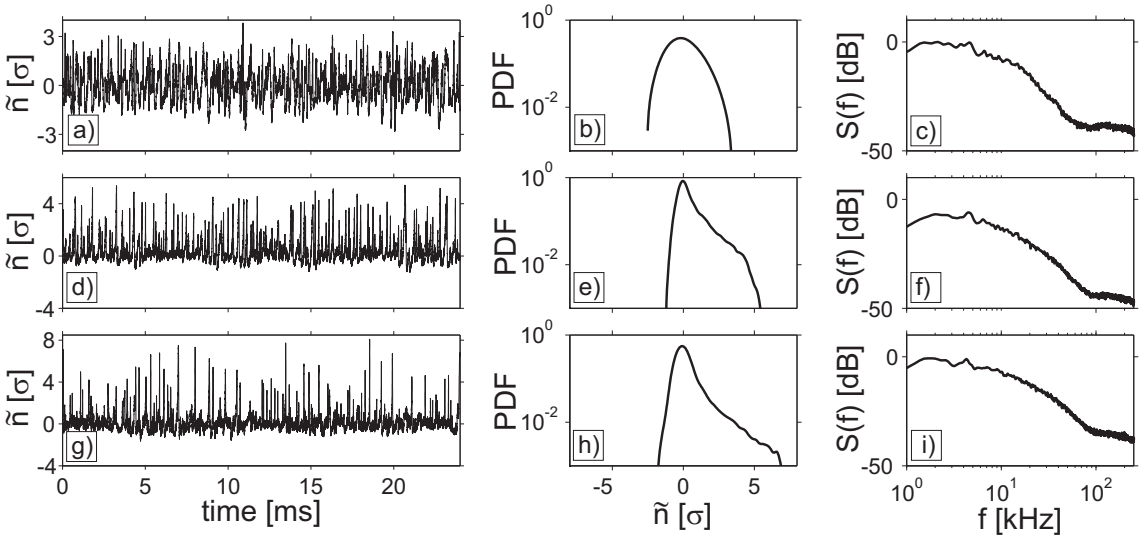

Figure 5.15: Time series of density fluctuations, probability distribution function (PDF) and frequency power spectra at radial positions A (a-c), B (d-f) and C (g-i).

a power-law decay. This is different from the case without limiter, in which the coherent drift mode dominates (see above). The plasma density fluctuations in the plasma edge (Fig. 5.15d-f) and in the far plasma edge (Fig. 5.15g-i) exhibit the same intermittent features as discussed previously in Sec. 5.1.1: Positive density bursts occur with amplitudes $> 7\,\sigma$ leading to non-Gaussian PDFs, skewed towards positive density fluctuations with skewness $s = 1.8$ and kurtosis $K = 3.4$ in the plasma edge at position B and $s = 2.6$ and $K = 10.2$ in the far plasma edge at position C, respectively.

The direct comparison between the two different experiments with and without limiter (Fig. 5.4) shows that the plasma fluctuation dynamics in the maximum density gradient region is strongly affected by the limiter, whereas the dynamics in the plasma edge remains essentially unchanged. In particular, if the limiter is introduced, a more broadband, fully developed turbulence situation is achieved.

5.2.2 Spatiotemporal evolution of plasma density fluctuations

An analysis of the space-time fluctuation dynamics has been done using the CA technique, similar to Sec. 5.1.2 for the experiments without limiter. However, a less developed probe array was used, with lower spatial resolution. The array consists of 9 probe pins with a vertical spacing of $\Delta y = 4\,\mathrm{mm}$. As above the array is moved across the radial plasma density profile. Reference probes are placed at positions A and B.

In the maximum density gradient region the dynamics of structures is not much changed by the limiter. The coherent part of the fluctuations is dominated by a $m = 1$ drift mode, propagating in direction of the electron diamagnetic drift. Also peel-off structures from the drift mode and their radial propagation are observed. These results were published in a research paper [124]. The result of the CA analysis with the reference probe located in

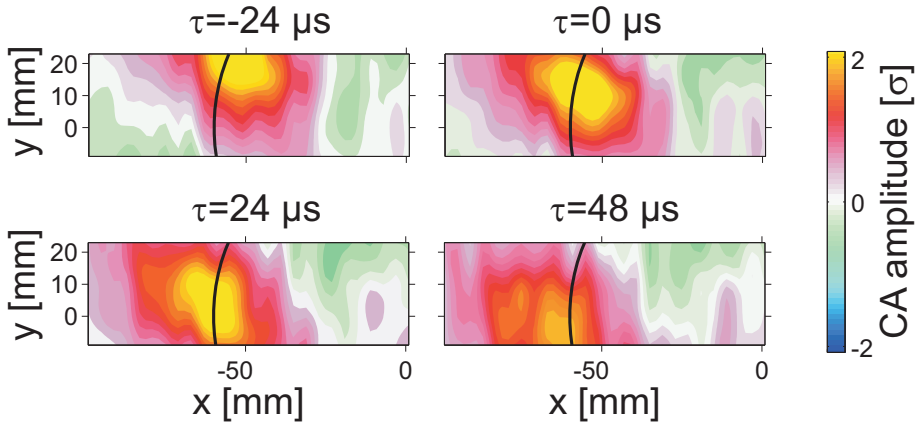

Figure 5.16: CA amplitude for the reference probe located in the plasma edge at position B. The CA amplitude condition is chosen to be $p = 2\,\sigma$. The CA amplitude is normalized to standard deviation σ. The black line indicates azimuthal direction.

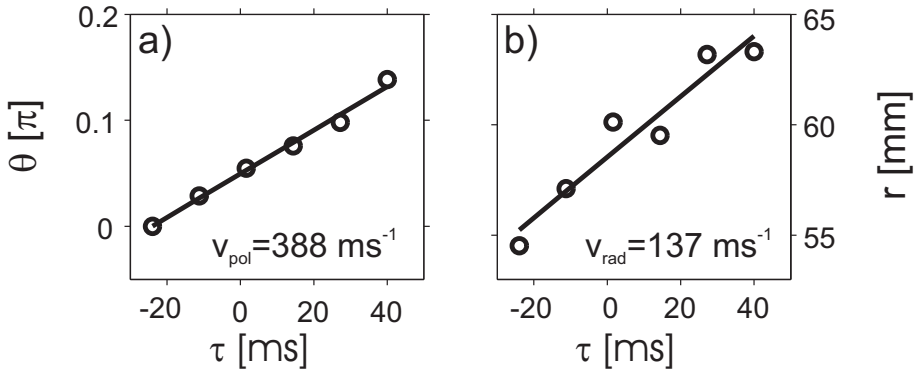

Figure 5.17: Azimuthal (a) and radial (b) velocity of the turbulent coherent structure observed in Fig. 5.16.

the plasma edge at position B is shown in Fig. 5.16 for four different time lags between $\tau = -24 \ldots 48\,\mu$s. Similar to Fig. 5.8, a turbulent structure is observed, propagating counterclockwise in the direction of the background $\boldsymbol{E}\times\boldsymbol{B}$-drift. A cross-correlation analysis yields maximum radial and azimuthal correlation lengths of $l_{rad} = 35\,$mm and $l_{pol} = 40\,$mm. The structure propagates not purely azimuthally but exhibits also a radial velocity component. The azimuthal and radial velocity of the turbulent structure is obtained by applying the same tracking technique as in Sec. 5.1.2. The result is shown in Fig. 5.17. The azimuthal velocity of the structure is $v_{\mathrm{pol}} = 388\,$m/s. The radial velocity of the structure is $v_{\mathrm{rad}} = 137\,$m/s, much less than without limiter. It corresponds to $7\,\%$ of the local ion sound speed (for $T_e = 1.8\,$eV) and is similar to the situation without limiter on a normalized scale.

In summary, introducing a poloidal limiter into the plasma column is an efficient way to destabilize drift waves in the density gradient, which leads to stronger developed turbulence. The plasma fluctuations in the edge region, however, exhibit the same intermittent features as in without limiter, i.e., turbulent structures are observed to propagate azimuthally in the $\boldsymbol{E}\times\boldsymbol{B}$-drift direction and radially outwards. The radial velocities are similar in dimensionless units $v_{\mathrm{rad}} \approx 5 - 10\,\%\, c_s$ for both cases.

6

Numerical simulations

In this chapter numerical simulations with the global three-dimensional CYTO code are discussed. The input parameters are chosen to be close to the experimental situation of VINETA (Ch. 5). The key issue of the present chapter is the comparison of weakly-developed drift-wave turbulence between experiment and simulation. In particular the formation and propagation of turbulent structures is investigated. The numerical simulation yields fluctuation time series for single spatial positions as well as for two-dimensional fields, which are evaluated in exactly the same way as the experimental data. The high spatial resolution of the simulation data at each time instant provides a more detailed insight into the formation and propagation mechanism of turbulent structures.

6.1 Simulation initialization and basic fluctuation characteristics

The model of the CYTO code was already outlined in Sec. 2.5. The chosen plasma and operational input parameters used for the CYTO run discussed in the following sections are compiled in Tab. 6.1. The normalized collisional parameters are $\nu_{\parallel} = 10.8$, $\nu_{en} = 4.81$, $\nu_{in} = 0.05$ and the density gradient length of the Gaussian source profile is $\kappa_n^{-1} = 1.3$. The equations of the CYTO code are numerically solved in a cylindrical co-ordiante system on a grid with $32 \times 64 \times 16$ points in radial, azimuthal and parallel direction, respectively. Two-dimensional fields of the plasma density and the plasma potential are recorded with a sampling frequency of $0.8\,\mathrm{MHz}$.

A time trace of the total fluctuation energy of the run is shown in Fig. 6.1. In the phase of linear growth the fluctuation energy increases exponentially. This region can clearly be distinguished from the phase of nonlinear growth saturation, starting at $t \approx 2.5\,\mathrm{ms}$. From here on the fluctuation energy remains essentially constant. Snapshot profiles of the background density and density fluctuations in the radial-azimuthal plane are shown in Fig. 6.2 for two simulation time instants, representing the linear and the nonlinearly

parameter	value
electron temperature T_e [eV]	3
ion temperature T_i [eV]	0.1
peak density n [10^{17} m^{-3}]	4.6
magnetic field B [mT]	60
Argon neutral gas pressure p_0 [Pa]	0.15
Argon neutral gas temperature T_0 [K]	400
density gradient length $L_\perp^{-1}$ [m^{-1}]	50

Table 6.1: Plasma and operational input parameters for the CYTO code.

saturated phase, respectively (the time instants are indicated in Fig. 6.1 by a red and a blue line). The density fluctuations are obtained by subtracting the azimuthally averaged density. In the linear phase, the density profile is given by the Gaussian source profile $S \sim \exp\left(-(r\kappa_n)^2\right)$. The density fluctuations are governed by a $m = 3$ drift mode with relatively small amplitude ($3\,\%$ of the peak density amplitude), which propagates in electron diamagnetic drift direction (upwards in Fig. 6.2). With increasing simulation time the amplitude of the $m = 3$ mode decreases and the plasma develops a weakly turbulent state, characterized by incoherent fluctuations. Due to nonlinear interactions, the energy is transferred towards both larger and smaller scales, which leads to a broadened modenumber spectrum. Fig. 6.3a shows the temporally resolved modenumber spectrum in the maximum density gradient region, obtained by wavelet analysis. The plasma is in the nonlinearly saturated phase (a similar diagram for the experiment was shown in Fig. 5.14a). An incoherent drift mode with mode number $m = 1$ dominates but strong contributions from $m = 2$ are observed as well, especially during the decrease of energy of the $m = 1$ mode. This already indicates a direct energy transfer from the $m = 1$ mode to higher modenumbers. The same is observed for the $m = 3$ mode, which has less energy and occurs preferentially if the lower modenumbers vanish. A comparison between two time-averaged modenumber spectra in weakly-developed drift-wave turbulence is shown

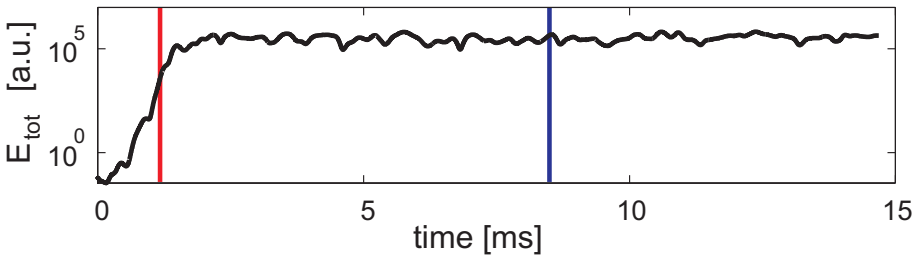

Figure 6.1: Time trace of the total fluctuation energy.

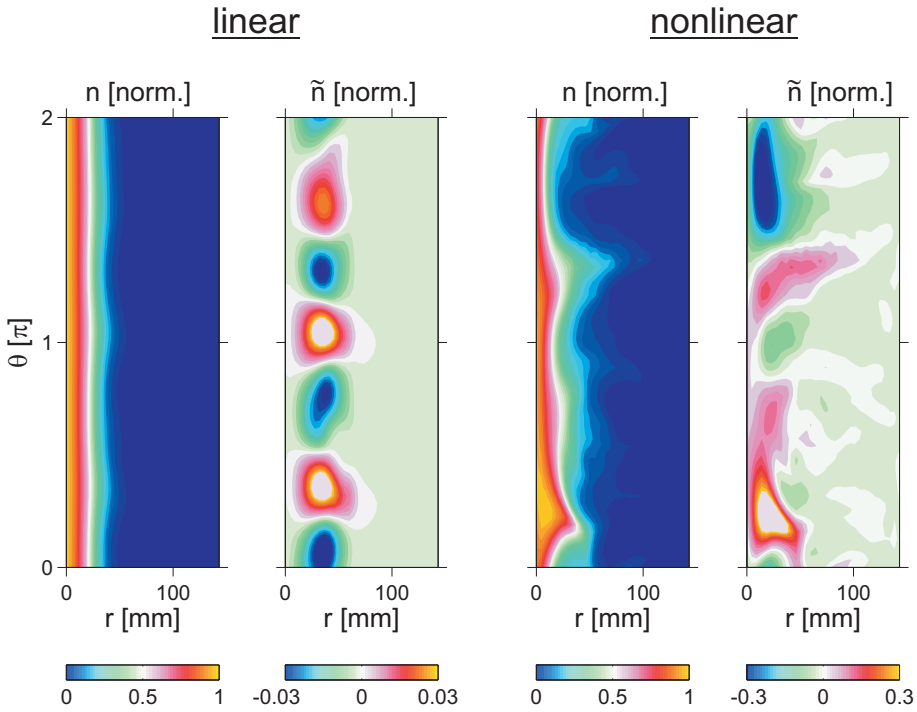

Figure 6.2: Snapshot of the radial-azimuthal profiles of density n and density fluctuations $\tilde{n}$ in the linear phase at simulation time $t = 1.2\,\mathrm{ms}$ (left column) and in the nonlinear saturated phase at simulation time $t = 8.49\,\mathrm{ms}$ (right column). The points in simulation time are indicated in Fig. 6.1.

in Fig. 6.3b. One is obtained for experimental data (red line) and the other from the CYTO code data (blue line). Both spectra exhibit similar features: $m = 1 - 3$ are the dominant drift modes and the power-law decay for higher modenumbers follows approximately the same spectral index ($\alpha = 3.4$ experimental and $\alpha = 4.2$ numerical).

In the nonlinearly saturated phase, the amplitude of the density fluctuations reaches $30\,\%$

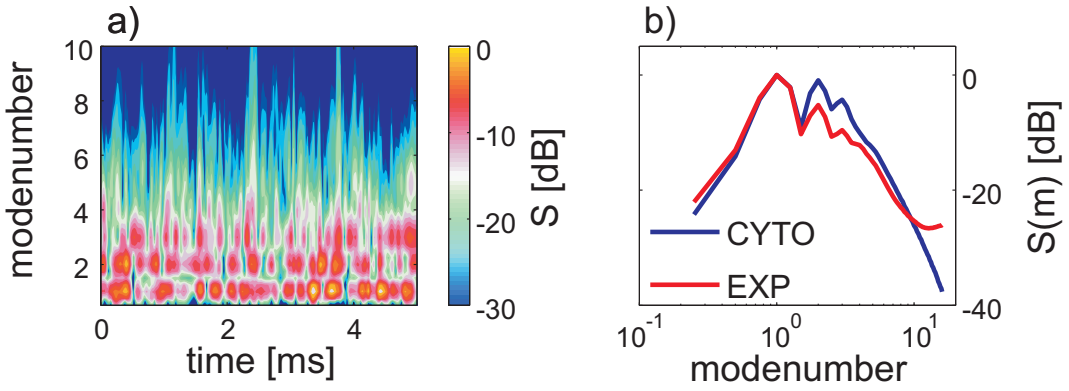

Figure 6.3: Temporal evolution of the wavelet modenumber spectrum in the radial plasma density gradient (a) and the corresponding time-averaged modenumber spectrum (b). For comparison, the experimental modenumber spectrum of weakly-developed drift-wave turbulence is shown as a red line in (b).

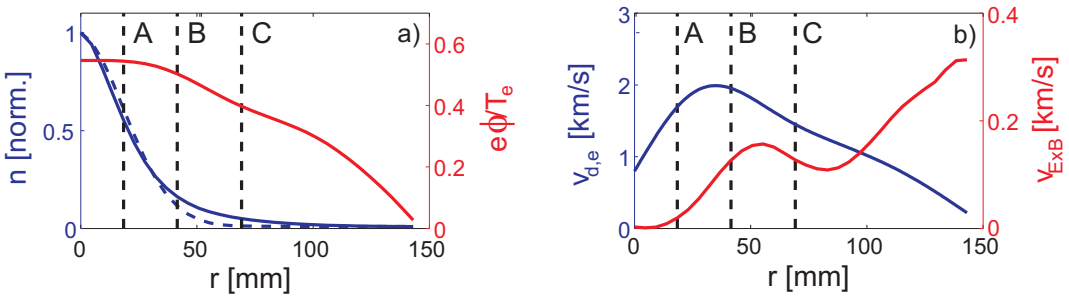

Figure 6.4: Time-averaged radial profiles of plasma density and potential (a) and corresponding perpendicular drift-velocities $\boldsymbol{v}_{E\times B}$ and $v_{d,e}$ (b). The dashed line in (a) indicates the source profile.

of the peak density and thus strongly modifies the density profile. As a consequence, the time-averaged radial density profile is broadened due to fluctuation-induced transport (Fig. 6.4a). In the plasma center the density profile still has mainly the Gaussian shape given by the source profile, but for $r > 35$ mm it strongly deviates from the source profile and develops a shoulder. The self-consistent plasma potential, which develops in response to the sheath-boundary conditions, is positive and has a convex shape (Fig. 6.4a), again in agreement with the experimentally observed potential profiles. The corresponding perpendicular drift velocities $\boldsymbol{v}_{E\times B}$ and $v_{d,e}$ are shown in Fig. 6.4b. The electron diamagnetic drift peaks in the maximum density gradient region at a value of $v_{d,e} \approx 2$ km/s and decreases towards the plasma edge. For the entire density profile the $\boldsymbol{E}\times\boldsymbol{B}$-velocity is smaller than the electron diamagnetic drift, $\boldsymbol{v}_{E\times B} < 400$ m/s.

6.1.1 Temporal evolution of plasma density fluctuations

The time history of the density fluctuations across the radial plasma density profile is analyzed at three different positions (for the corresponding experimental data cf. Fig. 5.4). The selected positions A, B and C are indicated in Fig. 6.4. Position A and B are in the maximum density gradient region ($r = 20$ mm and $r = 41$ mm) and position C is in the plasma edge ($r = 70$ mm). Fig. 6.5 shows the density fluctuation time series normalized to standard deviation $\tilde{n}/\sigma$, the respective probability distribution function (PDF), and frequency power spectra $S(f)$. The density fluctuations in the maximum density gradient region (Fig. 6.5a) are quasi-coherent with typical amplitudes of $1-2\,\sigma$ but they are asymmetric. The asymmetry is caused by sporadically occurring density bursts with peak amplitudes $\approx 3\sigma$. These bursts lead to a skewed PDF (Fig. 6.5b) with skewness $s = 0.75$ and kurtosis $K = 0.45$. In the frequency spectrum (Fig. 6.5c) there is a frequency peak at $f = 3.2$ kHz. For frequencies $f > 10$ kHz the spectral energy decreases following a power-law decay with spectral index $\alpha = 4.6$. For larger radii the intermittent character of the density fluctuations systematically increases. At position B the coherency in the time

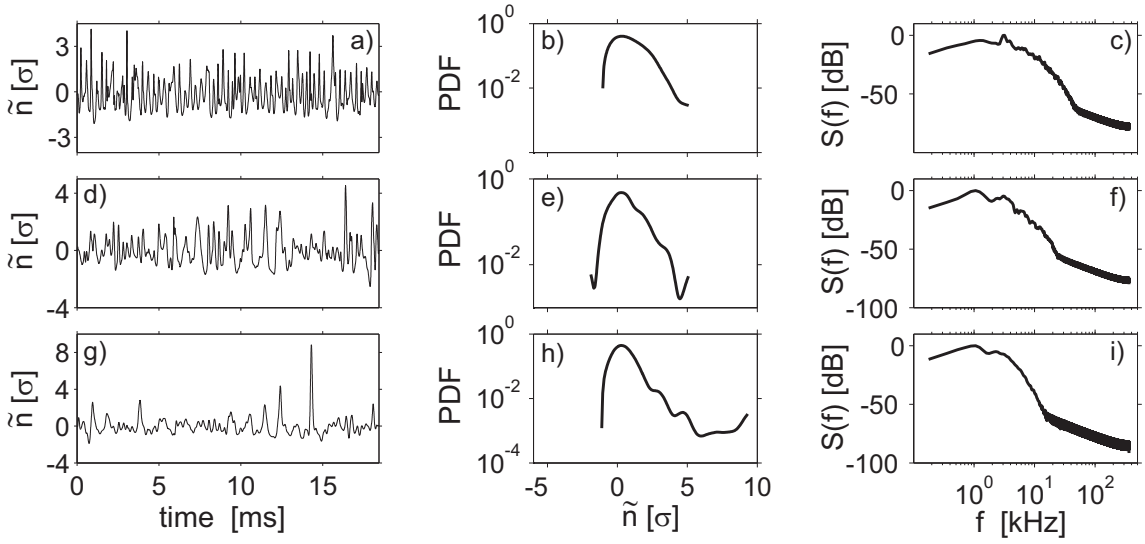

Figure 6.5: Time series of density fluctuations, probability distribution function (PDF) and frequency power spectra at radial positions A (a-c), B (d-f) and C (g-i) as indicated in Fig. 6.4.

series is completely lost. Density bursts with amplitudes of $3-4\,\sigma$ govern the time series. The bursts occur on a typical time scale of ≈ 1 ms. The contribution of the density bursts to the fluctuation spectrum is seen in the broadened hump at a frequency of $f \approx 1$ kHz (Fig. 6.5f). The skewness and kurtosis of the PDF are both increased ($s = 0.86$ and $K = 1.17$). In the plasma edge (Fig. 6.5g) the non-Gaussian character of density fluctuations further increases, indicated by a highly skewed and peaked PDF (Fig. 6.5h, $s = 3.4$ and kurtosis $K = 21$). The frequency spectrum (Fig. 6.5i) is flat for $f < 10$ kHz but a broadened small hump at $f \approx 1$ kHz is observed as well, indicating the only sparse contribution of the occasional density bursts to the total spectral energy.

A comparison of the fluctuation time series in the plasma edge (Fig. 6.5e) with the two-dimensional plot of the density fluctuations in the nonlinearly saturated phase (Fig. 6.2) already suggests that the density bursts in the plasma edge are associated with turbulent structures, propagating downwards the radial plasma density gradient. This picture is supported by a detailed study of the the radial particle flux $\tilde{\Gamma}$ that is calculated from the density and the potential fluctuations. The time-averaged radial particle flux $< \tilde{\Gamma} >$ plotted across the plasma density profile is shown in Fig. 6.6a. The particle flux is positive at all radii, corresponding to outward directed flux, and peaks in the maximum density gradient region.

The time series of the particle flux at the maximum density gradient region (Fig. 6.6b) shows that $\tilde{\Gamma}$ is strongly asymmetric and intermittent, characterized by high-amplitude transport bursts with $\tilde{\Gamma} \approx 5\,\sigma$. This is in agreement with the positive mean flux observed in Fig. 6.6a. The intermittent character is further confirmed by the increase of the kurtosis

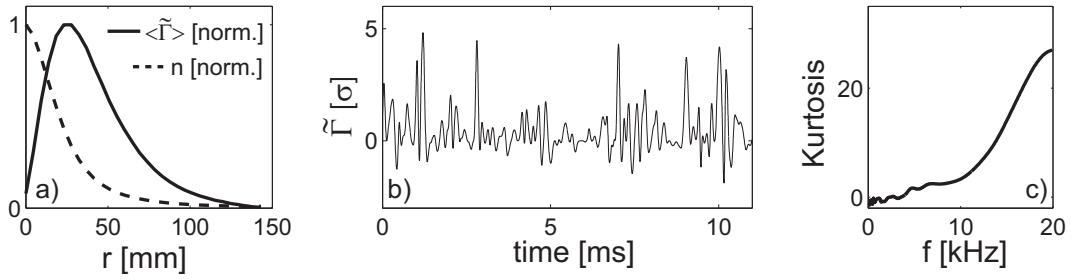

Figure 6.6: Time-averaged radial particle flux $< \tilde{\Gamma} >$ and background density profile n (a), time series of $\tilde{\Gamma}$ obtained in the radial plasma density gradient (b), and evolution of kurtosis for increasing frequency obtained from wavelet decomposition (c).

for increasing signal frequency, as obtained from wavelet decomposition (Fig. 6.6c).

6.1.2 Space-time analysis

On VINETA, the formation and propagation of turbulent structures was investigated by applying statistical techniques (cross-correlation or conditional averaging). The main advantage of numerical simulations is that structure formation can be directly observed at each time instant and the dynamics of each single fluctuation event can be obtained. An example of the time evolution of a turbulent structure is shown in Fig. 6.7, for six discrete simulation time instants in a range $t = t_0 \ldots t_0 + 55\,\mu$s. For all displayed time lags an azimuthally distorted $m = 1$ drift mode is observed in the maximum density gradient region ($r \approx 20 - 40\,$mm). The mode propagates in direction of the electron diamagnetic drift, which is upward in the representation of Fig. 6.7. Its phase velocity is approximately $v_{ph} = 585\,$m/s. This is in rough agreement with the linear dispersion relation (2.25), which yields for $k_\perp = 0.67\,\mathrm{cm}^{-1}$, $\rho_s = 1.86\,$cm, and a Doppler-corrected electron diamagnetic drift velocity of $v_{d,e} = 1.9\,$km/s (cf. Fig. 6.4) a phase velocity of $v_{m=1} = 748\,$m/s.

At $t = t_0$ and $t = t_0 + 11\,\mu$s the positive potential perturbation $\tilde{\phi} > 0$ is azimuthally phase-shifted against the positive density perturbation, thereby causing a radial flux of the positive density perturbation. Consequently, the density perturbation is radially elongated and extends into the plasma edge ($r \approx 60\,$mm) at $t = t_0 + 22\,\mu$s. Due to the azimuthal propagation of the drift mode, the turbulent structure peels-off the $m = 1$ mode for $t > t_0 + 22\,\mu$s and propagates azimuthally in direction of the background $\boldsymbol{E}\times\boldsymbol{B}$-drift (downwards) and radially outwards.

A detailed analysis of the average propagation speeds of the turbulent structures is difficult to obtain, since the structures strongly change their amplitude and shape during propagation. Therefore, and for the purpose of a comparison with the experimental findings, a statistical analysis using the conditional-average technique is chosen. The CA analysis has

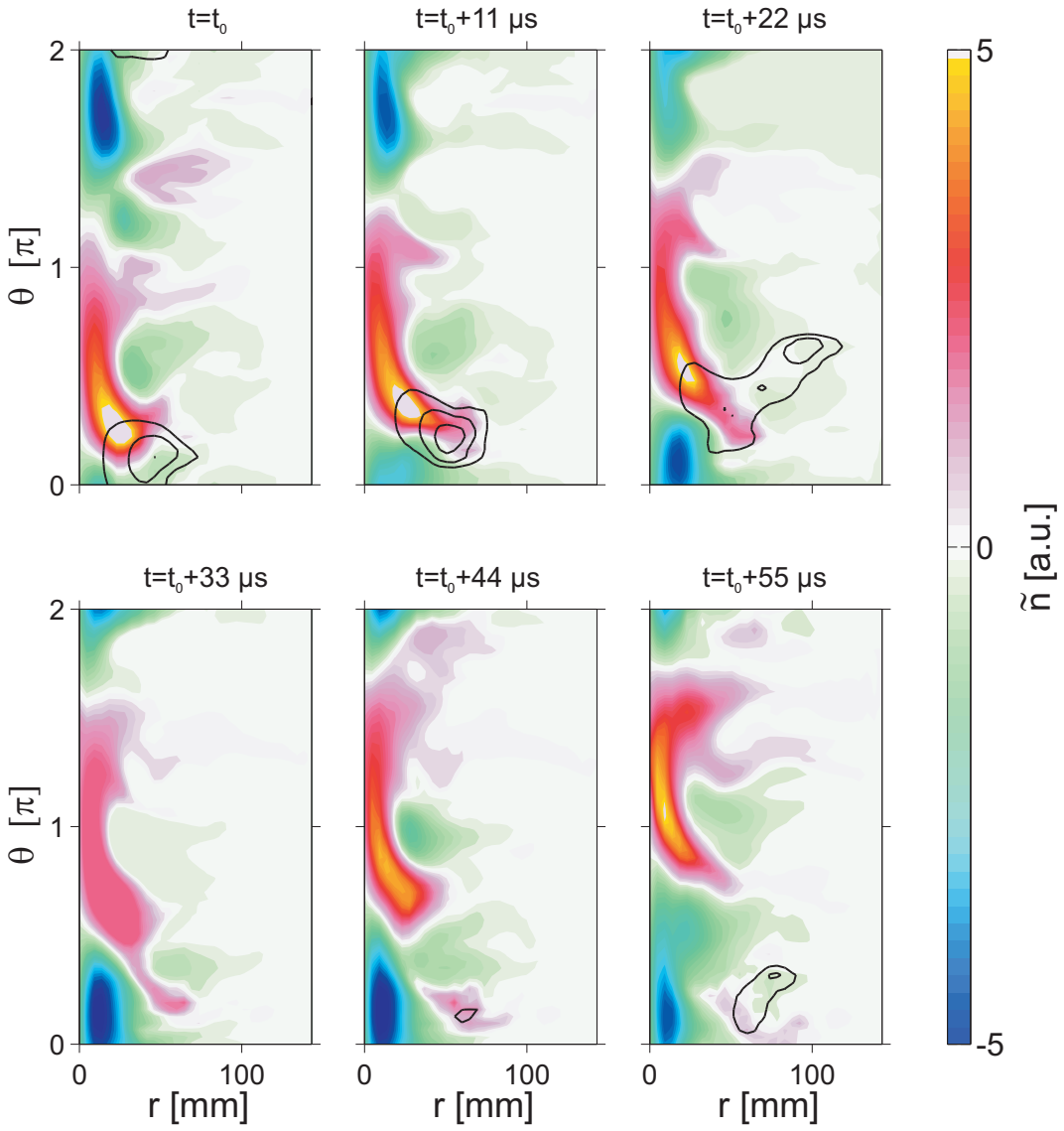

Figure 6.7: Density fluctuations in the radial-poloidal plane for six discrete simulation times $t = t_0 \ldots t_0 + 55\,\mu$s. The positive potential fluctuations $\tilde{\phi} > 0$ are superimposed as contour lines. The ambient magnetic field points out of the plane.

been applied for two reference positions. The resulting CA amplitude for the reference position $r = 54$ mm in the peel-off region of the turbulent structure is shown in Fig. 6.8. The amplitude condition was chosen to be $p = 1\,\sigma$. For the direct comparison with the experimental results, the fluctuations are mapped to a cartesian co-ordinate system. For the three time lags $\tau = -140 \ldots 120\,\mu$s (Fig. 6.8) a $m = 1$ drift mode relict propagates azimuthally counter-clockwise in $v_{d,e}$-drift direction. The positive density perturbation of the drift mode exhibits a radial velocity component. At time lag $\tau = 120\mu$s, a density portion peels radially off the drift mode, consistent with the observations in Fig. 6.7. A magnified view of the spatial phase between density and positive potential perturbations (obtained from the CA analysis of density fluctuations $R_{CA}(\tilde{n}, \tilde{n})$ and positive potential

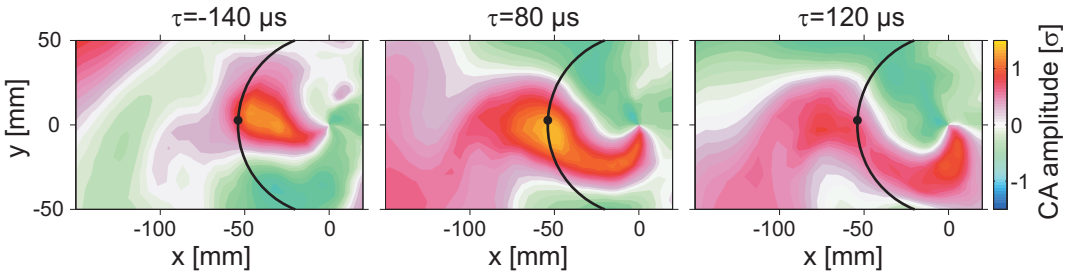

Figure 6.8: Conditionally averaged (CA) density fluctuations for three different time lags τ in the azimuthal plane. The reference probe is located in the peel-off region ($r = 54$ mm) of the turbulent structures from the drift mode (indicated by a black dot) and the amplitude condition was chosen to be $p = 1\,\sigma$. The CA amplitude is normalized to standard deviation σ. The black circle denotes azimuthal direction. The ambient magnetic field points out of the plane.

fluctuations $R_{CA}(\tilde{n}, \tilde{\phi} > 0)$) is shown in Fig. 6.9 for time lag $\tau = 140\,\mu$s. The potential perturbation lags behind the density perturbation with an azimuthal phase shift of $\approx \pi/2$. The phase shift results in a maximum fluctuation induced transport $\tilde{\Gamma}$ that is directed radially outwards but has an azimuthal component, due to the radial displacement of the positive potential perturbation.

The result for the conditionally averaged density fluctuations for the reference probe located in the plasma edge at $r = -84$ mm is shown in Fig. 6.10 for four time lags in the range $\tau = -345 \ldots 415\,\mu$s. The amplitude condition was chosen to be $p = 2\,\sigma$. A turbulent structure is observed, which propagates mainly clockwise in background $\boldsymbol{E}\times\boldsymbol{B}$-drift direction but exhibits also a significant radial velocity component. The driving mechanism is the same as for the peel-off process: An azimuthally phase-shifted potential causes an electric field $\tilde{E}_\theta$ and the resulting fluctuation induced $\tilde{v}_{E\times B}$-velocity propels the turbulent structure radially outwards. The spatial phase relation between the density and the poten-

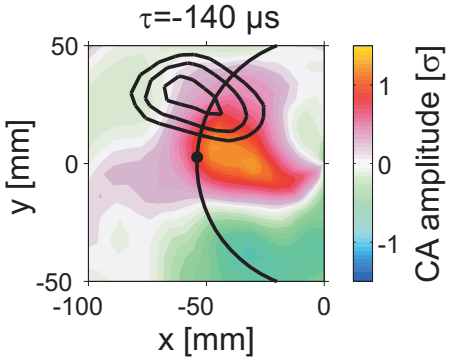

Figure 6.9: Conditionally averaged (CA) density fluctuations $R_{CA}(\tilde{n}, \tilde{n})$ and positive potential perturbations $R_{CA}(\tilde{n}, \tilde{\phi} > 0)$ superimposed as contour lines for time lag $\tau = -140\,\mu$s. The black dot indicates the reference probe and the black circle indicates azimuthal direction. The CA amplitude is normalized to standard deviation σ.

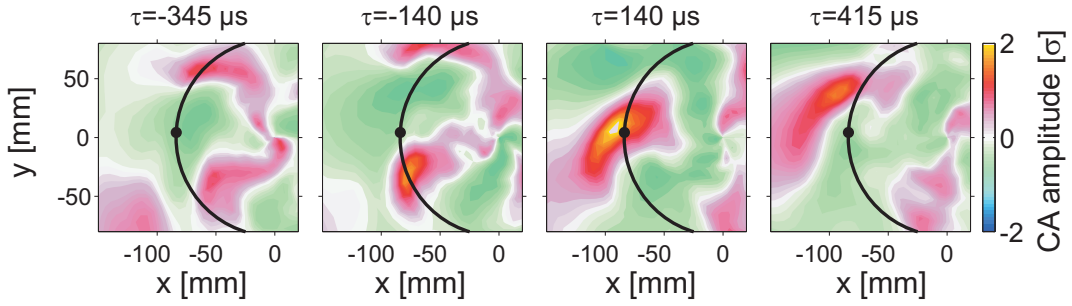

Figure 6.10: Conditionally averaged (CA) density fluctuations for three different time lags τ in the azimuthal plane. The reference probe is located in the plasma edge at $r = -84$ mm (indicated by a black dot) and the amplitude condition was chosen to be $p = 2\sigma$. The CA amplitude is normalized to standard deviation σ. The black circle denotes the purely azimuthal direction.

tial of the turbulent structure is shown in Fig. 6.11. The phase shift is similar if compared to the peel-off region (cf. Fig. 6.9). The propagation speeds of the turbulent structure are obtained by applying a tracking routine similar to the one used for the experimental case (Sec. 5.1.2). The structure was tracked for a range $\tau = -200 \ldots 400\,\mu$s and the respective center-off-mass positions are shown in Fig. 6.12. The velocities are obtained from linear fits to the data.

The turbulent structure propagates with approximately constant azimuthal velocity of $v_{\mathrm{pol}} = 133$ m/s, which is in agreement with the background $\boldsymbol{E}\times\boldsymbol{B}$-drift velocity at the position of the turbulent structure ($\boldsymbol{v}_{E\times B} = 150$ m/s at $r = 90$ mm, Fig. 6.4b). The radial velocity exhibits two different scaling regions (Fig. 6.12b). For $r \approx 80-90$ mm the structure propagates with a radial velocity of $v_{\mathrm{rad}} = 111$ m/s. For larger radii $r \approx 90-100$ mm the radial velocity of the structure decreases to $v_{\mathrm{rad}} = 40$ m/s. The decrease of the radial

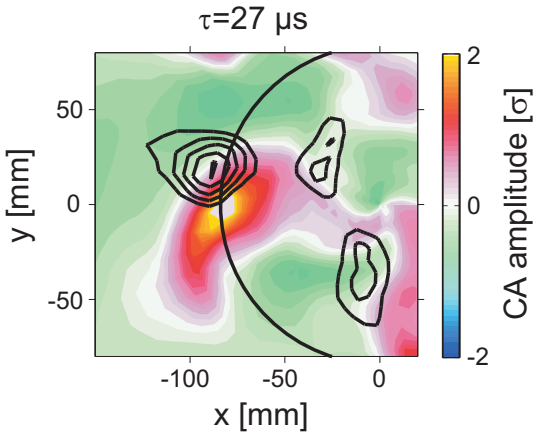

Figure 6.11: Conditionally averaged (CA) density fluctuations $R_{CA}(\tilde{n},\tilde{n})$ and positive potential perturbations $R_{CA}(\tilde{n},\tilde{\phi}>0)$ superimposed as contour lines for time lag $\tau = 0\,\mu$s. The black dot indicates the reference probe and the black circle indicates azimuthal direction. The CA amplitude is normalized to standard deviation σ.

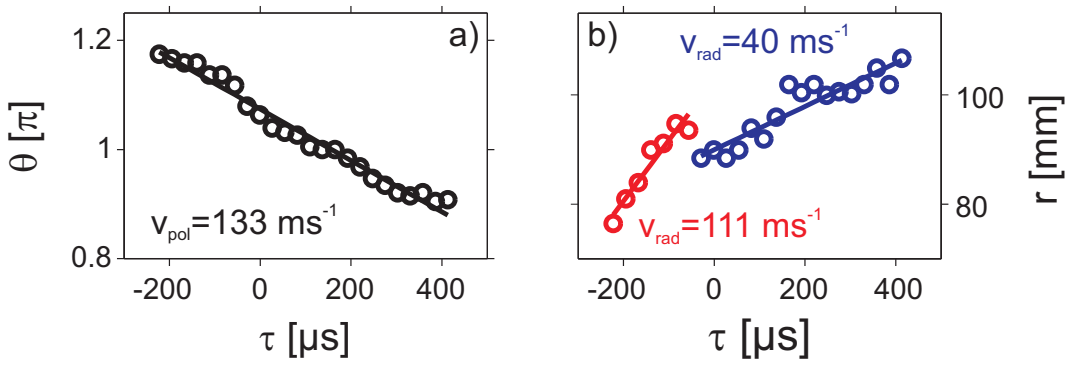

Figure 6.12: Azimuthal (a) and radial velocity (b) of the turbulent coherent structure observed in Fig. 6.10.

structure velocity is caused by a change of the spatial phase $\delta(\tilde{n}, \tilde{\phi})$ and by a decreasing amplitude of the related electric field $\tilde{E}_\theta$, which drops from $12-14$ V/m at $r \approx 80-90$ mm to $5-7$ V/m at larger distance. For two representative time lags, $\tau = -175\,\mu$s and $\tau = 350\,\mu$ (corresponding to the two scaling regions of the radial velocity) an azimuthal cut through the density and positive potential perturbation is shown in Fig. 6.13. Here θ_0 is the azimuthal position of the maximum density perturbation. The normalized density perturbation $\tilde{n}$ associated with the turbulent structure is shown as a blue line and the phase-shifted positive potential perturbation $\tilde{\phi} > 0$ as a red line. The radial $\boldsymbol{E}\times\boldsymbol{B}$-velocity $\tilde{v}_{E\times B} = -\nabla_\theta \tilde{\phi}/B$ calculated from the azimuthal profile of the potential perturbation is shown as a black line. At $\tau = -175\,\mu$s the phase shift is greater than $\pi/2$ and for the

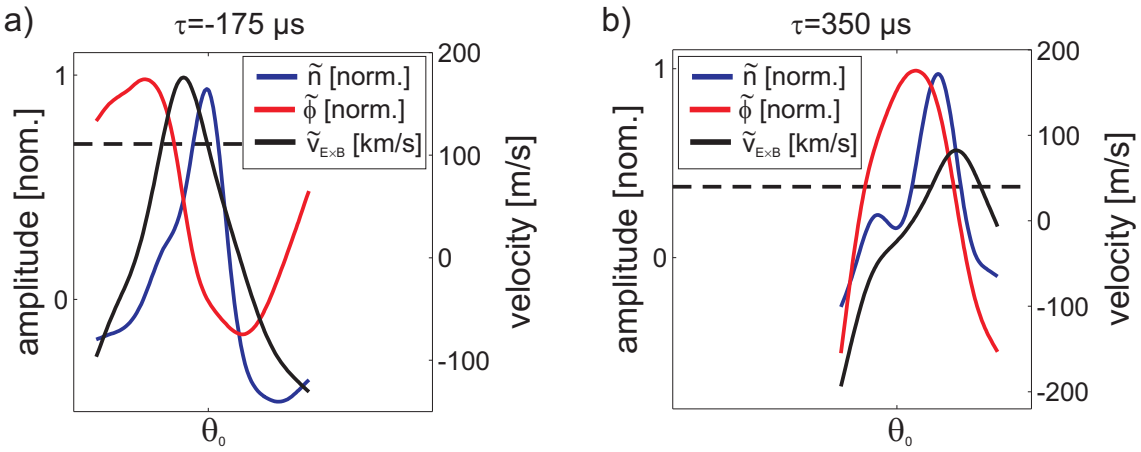

Figure 6.13: Normalized plasma density fluctuations $\tilde{n}$ (blue) and normalized positive plasma potential perturbations $\tilde{\phi} > 0$ (red) associated with the turbulent structure in the plasma edge along its azimuthal trajectory. The different time lags shown in (a) and (b) correspond to the two scaling regions of the radial structure velocity (Fig. 6.12b). The advection velocity $\tilde{v}_{E\times B}$ as calculated from the azimuthal profile of the potential perturbation is shown as black line, where positive values correspond to a radial outward propagation. For comparison the dashed lines shows the radial velocities of the turbulent structure obtained from the structure tracking (Fig. 6.12b).

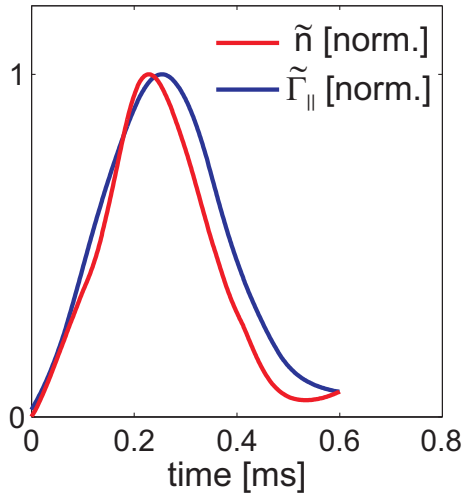

Figure 6.14: Single-point time trace of the density perturbation (red) and corresponding parallel flux (blue) of a turbulent structure in the plasma edge.

peak density perturbation the advection velocity $\tilde{v}_{E\times B}$ is in good agreement with the result of the tracking routine $v_{\mathrm{rad}} = 111\,\mathrm{m/s}$ (indicated in Fig. 6.13a as dashed line). At $\tau = 345\,\mu\mathrm{s}$ the phase shift is much smaller (Fig. 6.13b). This, together with the decreased amplitude of the fluctuating electric field, lowers the advection velocity to $\tilde{v}_{E\times B} \approx 50\,\mathrm{m/s}$ for the peak density perturbation, which is again in good agreement with the result of the tracking routine $v_{\mathrm{rad}} = 40\,\mathrm{m/s}$.

In the last section it has been reasoned that the driving mechanism of the radial structure propagation in the plasma edge is caused by the self-consistent electric field. The formation of the electric field can be explained by the three-dimensional structure of the density perturbation: Shown in Fig. 6.14 is a time trace of a positive density fluctuation, associated with a turbulent structure, at a single point in the azimuthal plane. The corresponding parallel particle flux $\tilde{\Gamma}_{\parallel} = \tilde{n}(\tilde{v}_{\parallel} - \tilde{u}_{\parallel})$ is shown as blue line. Here $\tilde{v}_{\parallel}$ and $\tilde{u}_{\parallel}$ are the parallel velocities of electrons and ions, respectively. The density perturbation is followed by a slightly phase-shifted parallel particle flux. Due to the fast electron response along the magnetic field the flux is non-zero and consequently a positive space-charge results. Having in mind that the turbulent structure propagates azimuthally with $\boldsymbol{E}\times\boldsymbol{B}$-velocity during the charge build-up process, a spatial phase shift is obtained (Fig. 6.13). This process is similar to the drift-wave mechanism (cf. Sec.2.1). For a deeper analysis of the space-time evolution of the fluctuating electric field the development of the density perturbation must be considered as an isolated event. However, because of the self-consistent formation of the density perturbation as a result of fluctuation-induced radial transport this cannot be studied.

6.2 Comparative discussion of experimental and numerical simulation results

The experimental observations on the space-time evolution of turbulent fluctuations (Ch. 5) and the numerical simulations are both focused on the topic formation and propagation of turbulent structures. To be able to perform a close comparison between experiment and simulation the input parameters of the CYTO code (Gaussian density source profile, collisionalities and geometrical parameters) are chosen to resemble the plasma and operational parameters of the experiment.

A key result of the CYTO code is already the observation of coherent drift-wave modes in the nonlinearly saturated phase, similar to what was observed in the experiment. We note here that this has never accomplished in for Hasegawa-Wakatani-like simulation runs. In experiment the azimuthal modenumber m of the drift wave increases with increasing magnetic field [30]. The same behavior is observed in the CYTO simulations (Fig. 2.5). While in the experimental situation a transition to a weakly developed drift-wave turbulence state is observed for increasing magnetic field at reduced collisionality, in the numerical simulation such a transition is mainly controlled by the ion-neutral collision frequency and ion viscosity. At low ion-neutral collision frequency and ion viscosity, their stabilizing influence in the linear dispersion relation is reduced and the plasma develops a weakly developed turbulent state. In the nonlinearly saturated phase the energy of the linear mode is transferred to larger and smaller scales due to nonlinear interaction. Both in experiment and simulation results the weakly-developed turbulent state is governed by a $m = 1$ drift-wave mode, which has the largest spatial scale. The mode is located in the maximum density gradient region and propagates in direction of the electron diamagnetic drift. The phase velocity of this mode agrees in both cases with the linear drift-wave dispersion relation. The time-averaged modenumber spectra show a good agreement for low modenumbers $m < 4$. For higher modenumbers the fluctuation energy decreases following a power-law decay both with spectral indices $\alpha = 3.4$ in the experiment and $\alpha = 4.2$ in numerical simulation. The deviation can be attributed to the numerical dissipation of the CYTO code at high modenumbers. The density perturbation of the $m = 1$ mode exhibits a potential perturbation, which lags behind the density perturbation with a phase shift of $\delta(\tilde{n}, \tilde{\phi}) \approx \pi/2$. The resulting azimuthal electric field gives rise to a radial $\tilde{v}_{E\times B}$-drift, which propels plasma particles radially outwards. This peel-off process is observed in the conditionally averaged fluctuations as obtained from experimental data and from numerical simulation data. The same is observed for single fluctuation events in the simulation data. The erratic occurrence of these transport events leads to the prominent intermittent behavior of the radial particle flux. It is dominated

by high-amplitude positive events, which cause an average outward particle flux $< \tilde{\Gamma} >$. When a turbulent structure peels-off the drift mode, it propagates azimuthally with the background $\boldsymbol{E}\times\boldsymbol{B}$-drift and radially outwards, driven by the self-consistent electric field. These structures strongly contribute to the fluctuation-induced radial transport. However, the velocities of the turbulent structures are different in experiment and in simulation. Both velocity components, the azimuthal and the radial ones, are higher in the experiment by a factor of 2-5. The deviation in the azimuthal velocity component is caused by the differences in the background potential profile, which is the main difference between the experiment and numerical simulation. In both cases it has a convex shape but with steeper radial gradients in the experiment, which leads to higher $\boldsymbol{E}\times\boldsymbol{B}$-velocity. A direct consequence is, that the high-amplitude density bursts in the plasma edge occur less frequently in the simulation. The potential profile in the CYTO code results self-consistently from the parallel sheath-boundary conditions. Discharge physics and its effect on the balance of electron and ion fluxes are neglected and for the density drive a Gaussian profile is imposed. In helicon wave heated discharges (as the VINETA device) the plasma heating due to an energy transfer from the wave to the plasma particles is known to be non-local [125]. This creates local heating and ionization sources, which may strongly modify the particle fluxes.

The radial advection velocity $\tilde{v}_{E\times B}$ of the turbulent structures is controlled by the amplitude of the self-consistent azimuthal electric field $\tilde{E}_\theta$, associated with the potential perturbation of the turbulent structure. $\tilde{E}_\theta$ is typically $20 - 30\,\mathrm{V/m}$ in the experiment, slightly larger than in the numerical simulation ($\tilde{E}_\theta \lesssim 14\,\mathrm{V/m}$). However, the resulting radial velocity of the turbulent structures also depends on the spatial phase $\delta(\tilde{n}, \tilde{\phi})$, which is slightly smaller in the simulation data than in the experiment. This leads to a lower radial velocity of the turbulent structures.

7

Intermittent transport events in the edge plasma of fusion devices

The experimental results presented in the previous section were obtained in a linear magnetized plasma column. Here the plasma is confined only perpendicular to the magnetic field. The plasma dynamics parallel to the magnetic field is governed by the plasma sheath at the end plates. The perpendicular particle flux across the magnetic field is rather convective than diffusive and is dominated by radially propagating, large-scale coherent structures that develop out of drift-wave turbulence. The driving force for this fluctuation-induced transport can be solely attributed to the self-consistent formation of poloidal electric fields that are associated with the turbulent structures. The latter give rise to a radially outwards directed $\boldsymbol{E}\times\boldsymbol{B}$-drift. As expected in magnetic geometries with open magnetic field lines the parallel transport exceeds the fluctuation-induced transport by orders of magnitude.

The cross-field transport in toroidal magnetic confinement devices is particularly important since it affects entirely the radial evolution of the plasma profiles and is a main cause for the degradation of the plasma confinement. However, the convective transport of plasma particles and energy across the confining magnetic field can also exceed the parallel transport [97; 126]. The experimental observation of high cross-field transport has been the subject of research during the last two decades [127; 23; 24; 128; 129]. Fluctuation induced transport is also referred to as "anomalous" diffusion, although it is a convective process. The observed perpendicular diffusion coefficients $D_\perp = \tilde{\Gamma}_\perp/\nabla_\perp n_0$ are orders of magnitudes higher than those predicted by classical or neo-classical diffusion theory. In a magnetic fusion device there are two distinct regions: the plasma core (confined region) and the scrape-off layer (SOL). In Fig. 7.1 a poloidal cross-section of a tokamak device is schematically shown. In the plasma core the magnetic flux surfaces are closed and radial transport is the only mechanism of plasma loss towards the material surfaces. In the SOL, the magnetic lines are intersected by material boundaries (end plates, limiters or the vacuum vessel). Here the plasma is strongly transported along the

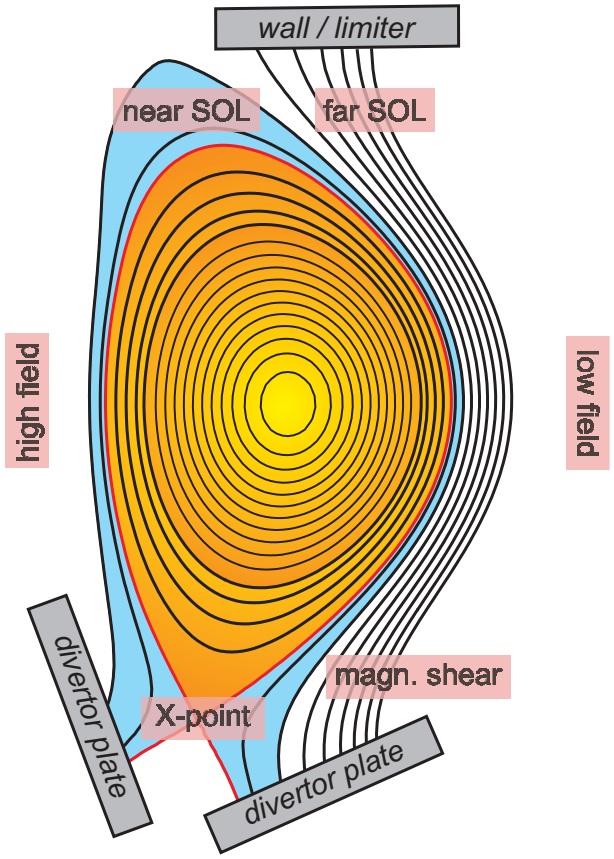

Figure 7.1: Poloidal cross-section of a tokamak with lower signal null configuration.

magnetic field to material surfaces. The last closed flux surface (LCFS) separates these two regions. The region close to the LCFS but in the confined region is referred to as the plasma edge. The SOL extends from the LCFS to the wall or limiter shadow. Similar to linear magnetic geometry, the radial plasma gradients in the plasma edge (Fig. 7.4) act as a source of free energy to drive instabilities, in particular the drift-wave instability. Due to the rather complex magnetic field topology of fusion devices, several other instabilities exist in the plasma edge. For example curvature driven instabilities as the trapped electron mode (TEM) and the ion temperature gradient mode (ITG) are expected to be largely responsible for anomalous cross-field heat transport of electrons and ions, respectively [130]. Numerical simulations revealed that drift-wave turbulence is dominant in the plasma edge region [131] while in the SOL a transition to the interchange instability is observed [132]. The fluctuation dynamics in the plasma edge is strongly influenced by the magnetic shear [133], X-point geometry [134], or flow shear layers generated by radial electric fields [135]. In contrast to the plasma edge, any fluctuation dynamics in the SOL is strongly affected by the parallel boundary conditions. In particular the plasma sheath at the end plates. The enhanced perpendicular particle flux across the magnetic field does not only lead to an unwanted broadening and flattening of radial density and tempera-

ture profiles but affects key fusion issues like first wall recycling of plasma particles or first wall heat load [126]. Although plasma fluctuations are generally considered to be of electromagnetic nature, the transport contribution due to fluctuations in the magnetic field (the so-called magnetic flutter transport) has been shown to be negligible when compared to the electrostatic $\boldsymbol{E}\times\boldsymbol{B}$-transport [127; 24] .

Regardless of the specific magnetic field topology, edge turbulence in toroidal fusion devices is characterized by intermittent fluctuations of the density, potential, and transport. Intermittent fluctuations are characterized by a non-Gaussian probability distribution function (PDF). It was observed in major tokamak devices as DIII-D [27], Alcator C-MOD [26], and MAST [136], in stellarators as W7-AS [137] and reversed field pinches as RFX [138; 139]. The intermittent bursts occur predominantly in the SOL and can be ascribed to large-amplitude self-organized coherent structures - called 'blobs' - that propagate radially outwards through the SOL with a velocity of less than one tenth of the ion sound speed typically [28]. Blobs are localized in the poloidal plane perpendicular to the ambient magnetic field but they are strongly elongated along the magnetic field thereby forming extended filaments with $k_\perp >> k_\parallel$ [29].

Recently it was demonstrated that approximately $50\,\%$ of the perpendicular turbulent transport in the SOL is carried by blobs [140]. Although blob propagation seems to be an universal phenomenon, important details of blob formation and radial propagation are far from being well understood.

Different model descriptions have been proposed to specifically describe the radial propagation of blobs. In the two-dimensional interchange model developed by Garcia *et al.* [141], both the formation and the self-consistent radial propagation of blobs are considered. Another model approach is to neglect the turbulent origin of the blobs and to focus on the radial propagation mechanism of the detached blob in the SOL [142; 143; 144]. The radial blob propagation in those models is not necessarily connected with the turbulent formation process of blobs. In the next sections these two model approaches are briefly outlined with particular attention to the radial blob propagation. In a later section the experimental results of a study on the radial blob propagation in the edge of the National Spherical Torus Experiment (NSTX) are presented and the results are compared with the model predictions.

7.1 Interchange instability

The interchange instability is the plasma analogon of the Rayleigh-Taylor instability that is observed in neutral fluids when a heavy fluid is supported against gravity by a lighter fluid. Since in a plasma gravitational effects usually can be neglected, the gravitational

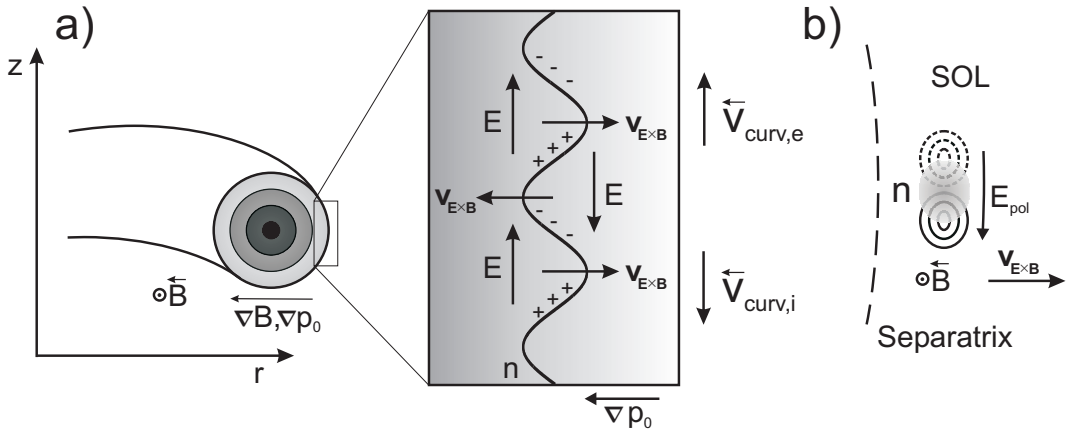

Figure 7.2: Schematic illustration of the interchange instability for the unfavourable curvature region (low-field side) of a toroidal fusion device (a) and the formation of poloidal electrid fields associated with a localized density perturbation in the SOL due to the interchange mechanism in the absence of a background plasma (b).

force is replaced by the net force due to the curvature of the magnetic field in toroidal devices. In contrast to configurations with homogeneous magnetic field like the VINETA device, where the diamagnetic current is incompressible, $\nabla \cdot \boldsymbol{J}_d = 0$, the curvature and gradient of the magnetic field in toroidal devices result in a compressible diamagnetic current

$$\nabla \cdot \boldsymbol{J}_d = \nabla \cdot (n_0 \boldsymbol{v}_d) = \frac{1}{B} \left(\nabla \times \boldsymbol{b} + \boldsymbol{b} \times \nabla \ln \boldsymbol{B} \right) \cdot \nabla p_0 \neq 0, \tag{7.1}$$

where $\boldsymbol{b} = \boldsymbol{B}/B$ is the unit vector along the magnetic field [145]. Note that only the compressible part of the diamagnetic current describes a collective motion of plasma particles, which corresponds in the single particle picture to the center drifts, $\nabla \boldsymbol{B}$-drift and curvature drift [48]

$$\boldsymbol{v}_{\nabla B} + \boldsymbol{v}_{curv.} = \frac{2T}{q} \frac{\boldsymbol{B} \times \nabla \boldsymbol{B}}{B^3}. \tag{7.2}$$

The mechanism of the interchange instability is schematically illustrated in Fig. 7.2a for the so-called unfavourable curvature region, in which the magnetic field gradient $\nabla \boldsymbol{B}$ is in parallel to the plasma pressure gradient ∇p_0. Consider a pressure perturbation orientated perpendicular to the background plasma pressure gradient ∇p_0. The curvature and $\nabla \boldsymbol{B}$ drifts lead to charge separation and consequently an electric field $\tilde{E}$, which gives rise to a radial $\boldsymbol{E} \times \boldsymbol{B}$-drift and amplifies the initial perturbation. The spatial phase shift between the density and potential perturbation is $\delta(\tilde{n}, \tilde{\phi}) = \pi/2$, which leads to a maximum radial particle flux $\tilde{\Gamma}$ (cf. Ch. 5). If the gradients of magnetic field and plasma pressure are anti-parallel initial perturbations are damped and the plasma is stable. In fusion devices the magnetic field strength scales with the major radius as $B \sim 1/R$. Thus, the unfavourable curvature region is located on the low-field side, while the favourable curvature region

is located on the high-field side. The interchange mode mechanism is basically a two-dimensional one and the parallel wavelength is infinite ($k_\parallel = 0$). However, due to the rotational transform of the magnetic field, the favourable and unfavourable regions are connected along the magnetic field [54], which leads to a three-dimensional structure of interchange modes, the so-called ballooning modes with $k_\parallel \neq 0$. The interchange mechanism is not only crucial for the amplification of small perturbations in the plasma edge region but also for the formation of electric fields associated with a density perturbation. The latter situation is depicted in Fig. 7.2b for a blob in the SOL in the absence of a background plasma. Due to the charge-dependent curvature drift, a dipolar potential vortex develops. The resulting poloidal electric field then causes a radial $\boldsymbol{E}\times\boldsymbol{B}$-drift of the blob.

7.2 Scaling of radial blob velocity

The model approaches addressing the radial blob propagation are either based on a fully self-consistent interchange model or on isolated structure propagation models. A common feature of all descriptions is the mechanism of the radial blob propagation, which was outlined in the last section. The poloidal electric field, which develops due to charge dependent curvature and $\nabla\boldsymbol{B}$-drift, determines the radial $\boldsymbol{E}\times\boldsymbol{B}$-velocity of the blob. The charge polarization of the blob acts as a current source and the closure of this current path is determined by the current along and perpendicular to the ambient magnetic field. A parallel current along the open magnetic field lines to the end plates can inhibit the formation of poloidal electric fields and thus inhibit radial propagation of a blob [132]. For each closure of the current path, a specific scaling of the radial blob velocity is obtained from the model descriptions. In the simplest approach, the influence of parallel currents on the blob dynamics is neglected. This is the case in the self-consistent model description of Garcia *et al.* [141; 146; 145], which addresses both the formation and radial propagation of blobs across the SOL. In this model the obtained radial blob velocity scales as

$$v_r = c_s \left(\frac{2a_b}{R} \frac{\tilde{n}}{n} \right)^{1/2}, \tag{7.3}$$

with a_b being the spatial scale of the blob and R the major radius. The effect of parallel currents is retained in this model as sheath dissipation that linearly damps predominantly large-scale fluctuations. Retaining the sheath dissipation in the model equations, it has been shown that the radial blob velocity significantly drops with increasing dissipation [145], but a clear scaling of the radial blob velocity has not been given.

In contrast, in the model description derived by Krasheninnikov, Myra and D'Ippolito [142; 143; 144; 147; 148] the formation process of the blob is ignored and the blob is

treated as an isolated structure in the SOL. In this model the effect of parallel currents is explicitly considered in the current path.

Parallel plasma resistivity $\eta = m\nu_{ei}/ne^2 \sim 1/T_e^{3/2}$ can prevent the current from flowing to the plasma sheath of material boundaries. For low parallel plasma resistivity the blob is connected to the plasma sheath and the parallel current $J_\parallel$ is determined by the sheath-boundary conditions [59]

$$J_{sheath} = -enc_s \left[1 - \exp\left(-\frac{e\phi}{T}\right)\right] \hat{\boldsymbol{n}} \cdot \boldsymbol{b}, \tag{7.4}$$

where $\hat{\boldsymbol{n}}$ is the surface unit normal vector and $\boldsymbol{b} = \boldsymbol{B}/B$ is the magnetic-field unit vector. The parallel boundary conditions determine the blob potential ϕ and consequently affect the resulting radial blob velocity. For high plasma resistivity η the blob is disconnected from the end plates and the dynamics of the blob is solely determined by the interchange dynamics (ballooning). This process holds especially in the divertor region where the electrons are cooled by refueled neutrals. The disconnection of the blobs from the sheath with increasing parallel plasma resistivity has been observed in numerical simulations [149; 132]. In regions with a specific magnetic field topology as e.g. X-points, where the flux tubes become long elongated fans, cross-field current is greatly eased [150; 132; 148]. In these regions the parallel current associated with the blob can be short-circuited by any process that can provide a perpendicular current $J_\perp$, for instance electron-ion collisions, ion viscosity or ion polarization drifts.

The discussed possible closures of the parallel current are schematically illustrated in Fig. 7.3. The curvature drift is the current source J_C and for low parallel resistivity η the blob is connected with the sheath and the parallel current $J_\parallel$ is determined by the sheath-current J_{sheath}. In the X-point region with its specific magnetic field topology, the parallel current can be short-circuited by a cross-field current, as the ion polarization cur-

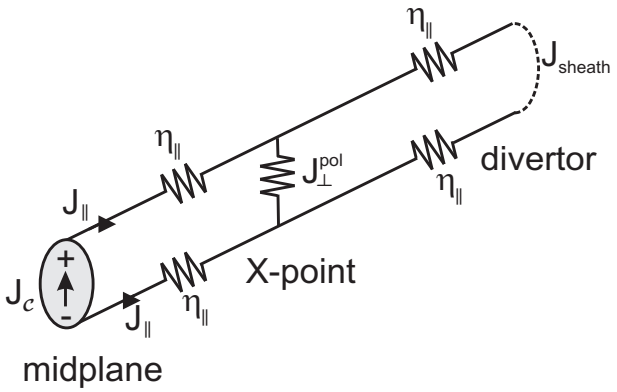

Figure 7.3: Possible closures of the current loop associated with a blob.

blob instability regime	normalized radial blob velocity v_r
2D sheath-connected	$c_s q \rho_s^2 / a_b^2$
3D disconnected (X-point)	$q^{2/3} c_s \rho_s^{1/3} \nu_{ei}^{1/3} / a_b^{1/3} \Omega_{ce}^{1/3}$
3D ideal ballooning	$c_s a_b^{1/2} / R^{1/2}$

Table 7.1: Scaling of the radial blob velocity v_r in the various instability regimes, where $q = L_\parallel / R$ is the safety factor, $L_\parallel$ is the parallel connection length, R is the major radius and a_b is the blob scale size (nominal blob radius).

rent $J_\perp^{pol}$. For high plasma resistivity the blob is disconnected from material boundaries. Each instability regime of the blob, sheath-connected, resistive X-point and resistive ballooning, obeys characteristic scaling properties of the blobs radial velocity [147] which are compiled in Tab. 7.1. Note that the blob velocity scaling given in Tab. 7.1 is for isolated blobs in the absence of a background plasma [147]. In the presence of a background plasma the scaling must be modified to f/a_b, where $f \sim \tilde{n}/n$ denotes the relative density perturbation of the blob. In the disconnected ballooning regime the radial blob velocity is proportional to the square-root of the blob radius a_b, while in the other regimes smaller blobs are expected to propagate faster than larger blobs. Regardless of the scaling predictions for the radial blob velocity, the minimum blob velocity occurs in the sheath-connected regime, where the current associated with the blob is free to flow along the field lines [148]. The scaling obtained in the self-consistent interchange model of Garcia *et al.* [141] corresponds to the ballooning regime in Tab. 7.1.

Within the framework of the present thesis, experimental data from the National Spherical Torus Experiment (NSTX) [151] has been obtained. Optical imaging of plasma edge turbulence in a two-dimensional plane perpendicular to the magnetic field has been analyzed with respect to the scaling of the radial blob velocity in order to compare the findings with the scaling predictions of the various models. The applicability of the different blob instability regimes is mainly determined by geometrical parameters and external control parameters, as magnetic field strength and magnetic field topology, but also by plasma parameters, as collisionality that vary across the SOL. A detailed analysis for NSTX edge plasma parameters [148] reveals that the governing blob instability regimes are the X-point regime and the sheath-connected regime, where larger blobs are expected to propagate faster than smaller blobs. In the following sections a detailed comparison of this prediction with experimental observations is done.

7.3 Turbulent structure propagation in the edge and SOL of NSTX

NSTX is a medium-sized spherical tokamak experiment with major radius $R = 0.85\,\mathrm{m}$ and minor radius $a = 0.68\,\mathrm{m}$. The device is located at the Princeton Plasma Physics Laboratory, New Jersey (USA). For a general overview of NSTX the reader is referred to Ref. [151]. As a spherical tokamak, NSTX has a very low aspect ratio of $A = R/a = 1.3$; a typical tokamak has $A \approx 3$. This allows for operations at high plasma pressure since

$$\beta = \frac{p}{B_t^2/2\mu_0} \sim \frac{I_p}{aB_t} \sim \frac{1}{Aq}, \tag{7.5}$$

where I_p is the plasma current and B_t is the toroidal magnetic field. The limit is at $\beta_{max} \approx 40\,\%$. The measurement results presented here are obtained from 11 similar L-mode discharges (shot numbers #113733-#113744), heated by neutral beam injection (NBI) of power $P_{\mathrm{NBI}} = 2-4\,\mathrm{MW}$, toroidal magnetic field on axis of $B = 0.3\,\mathrm{T}$ with near double-null configuration, a plasma current of $I_p = 800\,\mathrm{kA}$ and $\beta = 10\,\%$. The magnetic configuration is shown in Fig. 3.9a. Radial profiles of the electron density and electron temperature are measured with Thomson-scattering along the outer midplane. The profiles are shown in Fig. 7.4a. In the plasma core the peak electron density and temperature are $n_e \approx 3 \cdot 10^{19}\,\mathrm{m}^{-3}$ and $T_e \approx 0.6\,\mathrm{keV}$, respectively, while in the SOL the values drop to $n_e \approx 0.2 - 2 \cdot 10^{19}\,\mathrm{m}^{-3}$ and $T_e \approx 3 - 50\,\mathrm{eV}$.

The turbulent edge and SOL fluctuations are measured using the Gas Puff Imaging technique (GPI) [78; 28], which records the visible D_α line emission from a localized deu-

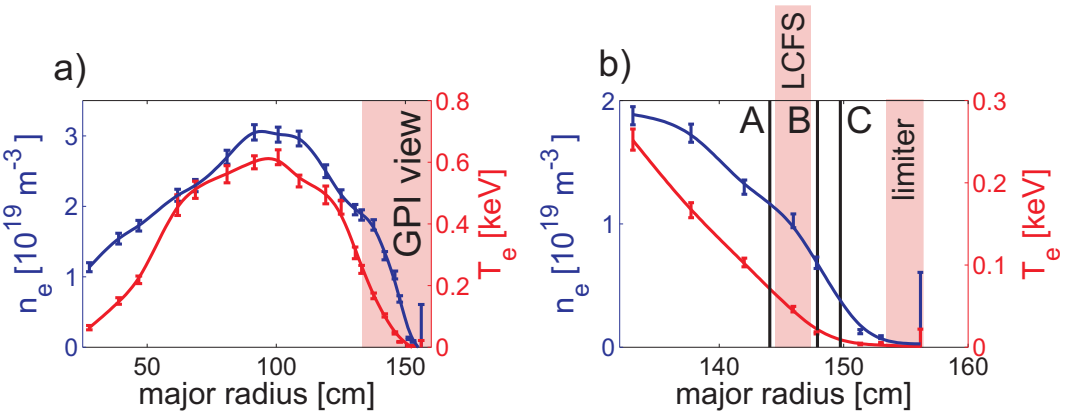

Figure 7.4: (a) Radial profiles of electron density and temperature for NSTX shot #113737 at time $t = 176.7\,\mathrm{ms}$ in the shot obtained from Thomson-scattering along the outer midplane. The red shaded box indicates the radial localization of the GPI view. (b) Magnified radial profiles of n_e and T_e for the GPI field-of-view. The positions of the LCFS and the limiter shadow are indicated as red boxes.

parameter	LCFS	SOL ($r - r_{sep} = 5\,\text{cm}$)
electron density n [$10^{19}\,\text{m}^{-3}$]	0.7	0.05
electron temperature T_e [eV]	20	3
drift scale ρ_s [mm]	1.5	0.58
ion sound speed c_s [km/s]	44	17

Table 7.2: NSTX parameters derived from Thomson scattering measured along the outer midplane. r_{sep} is the radial position of the LCFS obtained from the free boundary equilibrium reconstruction code LRDFIT.

terium gas puff at the outer midplane. Complementary to the two-dimensional GPI diagnostics, an array of fast diode D_α views is arranged radially and poloidally within the GPI field-of-view. This spectroscopic diagnostic is described in detail in Sec. 3.1.4. Although the D_α emission intensity is a nonlinear function electron density and temperature, the contribution of temperature fluctuations can be neglected for $T_e \gtrsim 10\,\text{eV}$. Therefore the D_α intensity fluctuations are being taken as proportional to density fluctuations. The two-dimensional GPI field-of-view (cf. Fig. 3.9c) is oriented tangentially to the local magnetic field in order to resolve the radial and poloidal structure of the plasma fluctuation structures propagating perpendicular to the ambient magnetic field. It spans a range from $r = 133.5 - 160.4\,\text{cm}$ radially and $z = 9 - 31\,\text{cm}$ poloidally, covering the plasma edge region and the entire SOL. The radial localization of the GPI view is indicated in Fig. 7.4a by the red shaded box. The radial profiles of the electron density and temperature within the GPI field-of-view for the discharges under consideration are shown in Fig. 7.4b. The uncertainty of the position of the LCFS is indicated by the red shaded area. Typical plasma parameters for the edge and SOL region are compiled in Tab. 7.2.

7.3.1 Temporal evolution of fluctuations across the SOL

The first step is the characterization of the temporal evolution of the fluctuations in the plasma edge and SOL. Single-point measurements at three positions A, B, and C as measured with the D_α diodes are shown in Fig. 7.5 (the positions A, B and C are indicated in Fig. 7.4b). Position A corresponds to the plasma edge region inside the LCFS ($r - r_{sep} \approx -2\,\text{cm}$), while position B is outside the LCFS in the near SOL ($r - r_{sep} \approx 2\,\text{cm}$). Position C is in the mid-SOL region ($r - r_{sep} \approx 4\,\text{cm}$). Shown are the fluctuation time series normalized to standard deviation σ, the corresponding PDFs and frequency power spectra. Regardless of the confined or unconfined region (inside or outside the LCFS), the density fluctuations close to the LCFS exhibit the same characteristics (Figs. 7.5a and

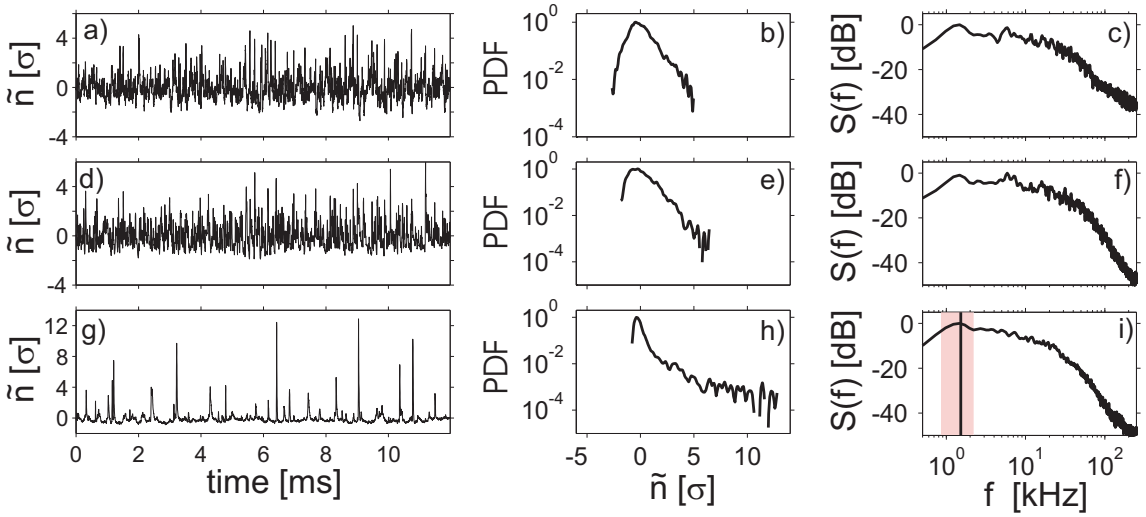

Figure 7.5: Time series of density fluctuations, probability distribution function (PDF) and frequency power spectra at radial positions A (a-c), B (d-f) and C (g-i) as indicated in Fig. 7.4b for NSTX shot #113734.

7.5d) with a non-Gaussian distribution of the fluctuation amplitude and sporadic density bursts at relatively large amplitudes $\tilde{n} \sim 4\,\sigma$. This behavior is confirmed by the PDFs (Figs. 7.5b and 7.5e) showing pronounced positive tails. The skewness and kurtosis of the PDF increase from $s = 0.97$ and $K = 1.9$ (position A) to $s = 1.1$ and $K = 1.9$ (position B). The frequency power spectra are flat in the low frequency range $f < 30\,\text{kHz}$ (Figs. 7.5c and 7.5f) . For higher frequencies ($f > 30\,\text{kHz}$) the spectral power drops following a power law $S \sim f^{-\alpha}$. The spectral index is lower inside the LCFS with $\alpha = 2.5$ compared to the near SOL region with $\alpha = 5$. The density fluctuations in the mid-SOL are characterized by intermittent bursts with amplitudes $\tilde{n} > 12\,\sigma$ (Fig. 7.5g), which leads to a highly non-Gaussian PDF (Fig. 7.5h) with skewness $s = 5.8$ and kurtosis $K = 47.5$. The frequency of the bursts with amplitudes $\tilde{n} > 3\,\sigma$ is $f_b = 1.52 \pm 0.6\,\text{kHz}$. It is indicated in the frequency spectrum (Fig. 7.5i) as a black vertical line. The red shaded box corresponds to the (estimated) uncertainty. At this particular frequency a small hump is found in the spectra, not only here but also close to the LCFS.

7.3.2 Spatiotemporal evolution of fluctuations across the SOL

The space-time evolution of plasma fluctuations are measured with a Princeton Scientific Instruments (PSI5) camera with frame rate of 250 kHz and 300 frames memory. Thus, the total acquisition time is $1.2\,\text{ms}$. The pre-processing of the raw camera images includes bandpass filtering with passband $f_1 < f < f_2$, $f_1 = 1\,\text{kHz}$ and $f_2 = 115\,\text{kHz}$, respectively, to remove the contribution of the background emission. To reduce the random pixel noise, mainly due to the neutron/gamma background, a two-dimensional median fil-

tering over 3 pixel and a two-dimensional singular value decomposition are done for each frame. A sequence of six pre-processed camera images is shown in Fig. 7.6. In total the structure was tracked for $120\,\mu$s, corresponding to 30 camera frames (in this sequence a time of $100\,\mu$s is covered). The position of the LCFS and the limiter shadow are indicated as solid and dashed line, respectively. A turbulent structure is observed that propagates poloidally downwards in the direction of the ion diamagnetic drift and radially outwards from the LCFS into the limiter shadow, across the entire SOL. When the structure emerges at the LCFS, it is slightly elongated with $k_\theta < k_r$ but approaches a circular shape during propagation. The amplitude of the structure increases while propagating into the SOL. For larger radii, however, the amplitude decreases and a strong drop in amplitude occurs in the limiter shadow. The decrease of the amplitude in the region close to the limiter shadow is a self-consistent feature of the turbulent structures. It cannot be explained by the evolution of the time-averaged emission profile (Fig. 3.9c) and it is likely to be caused by the parallel plasma flow to material boundaries.

The poloidal wavenumber spectrum $S(r, k_\theta)$ is investigated using wavelet transform of the camera images. Fig. 7.7a shows the radially resolved poloidal wavenumber spectrum $S(r, k_\theta)$ averaged over all camera frames. Large-scale structures with $k_\theta \approx 1\,\mathrm{cm}^{-1}$ corresponding to a scale size of approximately $6\,$cm are predominant in the near SOL. The contribution of small-scale structures to the spectrum has a maximum close to the LCFS and decreases for larger radii. For the radial position indicated in Fig. 7.7a by a dashed line the temporally resolved poloidal wavenumber spectrum was calculated. It is shown

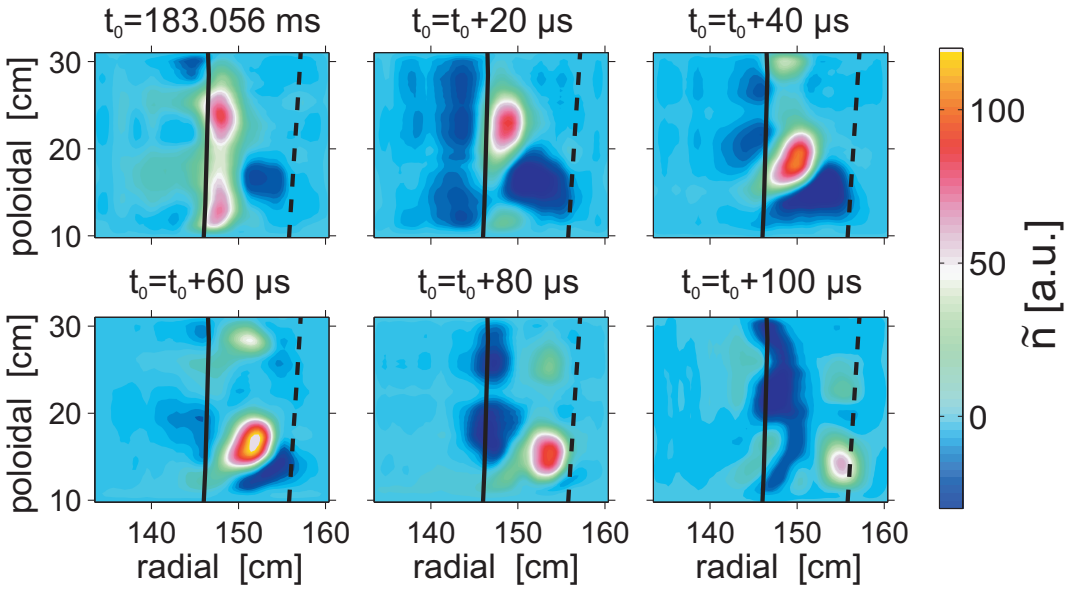

Figure 7.6: Pre-processed raw images of the PSI5 camera (shot #113734). A coherent structure propagates from the LCFS region (indicated by the solid black line) across the SOL towards the limiter shadow (indicated by the dashed black line).

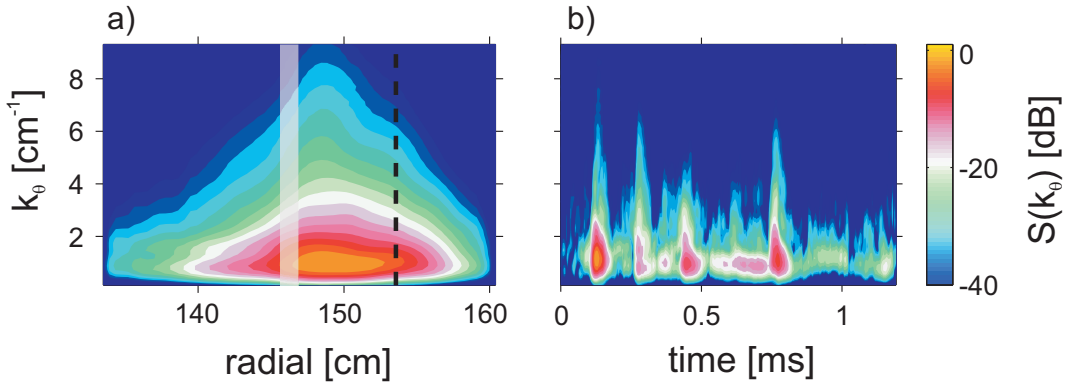

Figure 7.7: (a) Radially resolved poloidal wavenumber spectrum of density fluctuations for NSTX shot #113734. The shaded area corresponds to the position of the LCFS. (b) Temporally resolved poloidal wavenumber spectrum of D_α fluctuations in the SOL at the radial position indicated in (a) as dashed line.

in Fig. 7.7b. The occurrence of fluctuation events with $k_\theta \approx 1\,\mathrm{cm}^{-1}$ is sporadic and resembles the occurrence of large-amplitude fluctuations in the time series of Fig. 7.5g. The poloidal scale of the occasionally occurring structures is not uniform but typically centered around $k_\theta \sim 0.5 - 1.5\,\mathrm{cm}^{-1}$.

7.3.3 Propagation of individual structures

In the context of fluctuation-induced transport, the investigations on the propagation and the amplitude evolution of structures are of major importance. For this purpose individual fluctuation structures are tracked over their lifetime and their specific properties (propagation speeds, sizes and amplitudes) are evaluated.

After the data pre-processing step, the camera images are decomposed using an amplitude and area threshold condition to extract localized structures. The condition for the amplitude was set to one standard deviation of each pixel time series, and the condition for the total area was set to five pixel, which corresponds to a spatial area of $0.7\,\mathrm{cm}^2$. All identified objects in each frame are labeled and the individual properties (area, amplitude, center of mass position, position of maximum, bounding box, orientation) are extracted from the data. The actual spatial area of a structure is defined as the area, in which the amplitude of the structure exceeds $20\,\%$ of the local time-averaged D_α intensity. Structures are considered as being related to each other in consecutive frames if the center of a structure in frame $i+1$ is found in the bounding box of a structure in frame i. This criterion implies an upper limit for the structure velocity of $4 - 5\,\mathrm{km/s}$ for small scale structures ($5\,\mathrm{cm}^2$), $5 - 6\,\mathrm{km/s}$ for medium scale structures ($10\,\mathrm{cm}^2$) and $\sim 7 - 10\,\mathrm{km/s}$ for large scale structures ($25\,\mathrm{cm}^2$). Typical structure velocities in the SOL region are $\leq 5\,\mathrm{km/s}$ in poloidal and $1\,\mathrm{km/s}$ in radial direction [81]. However, turbulent small-scale

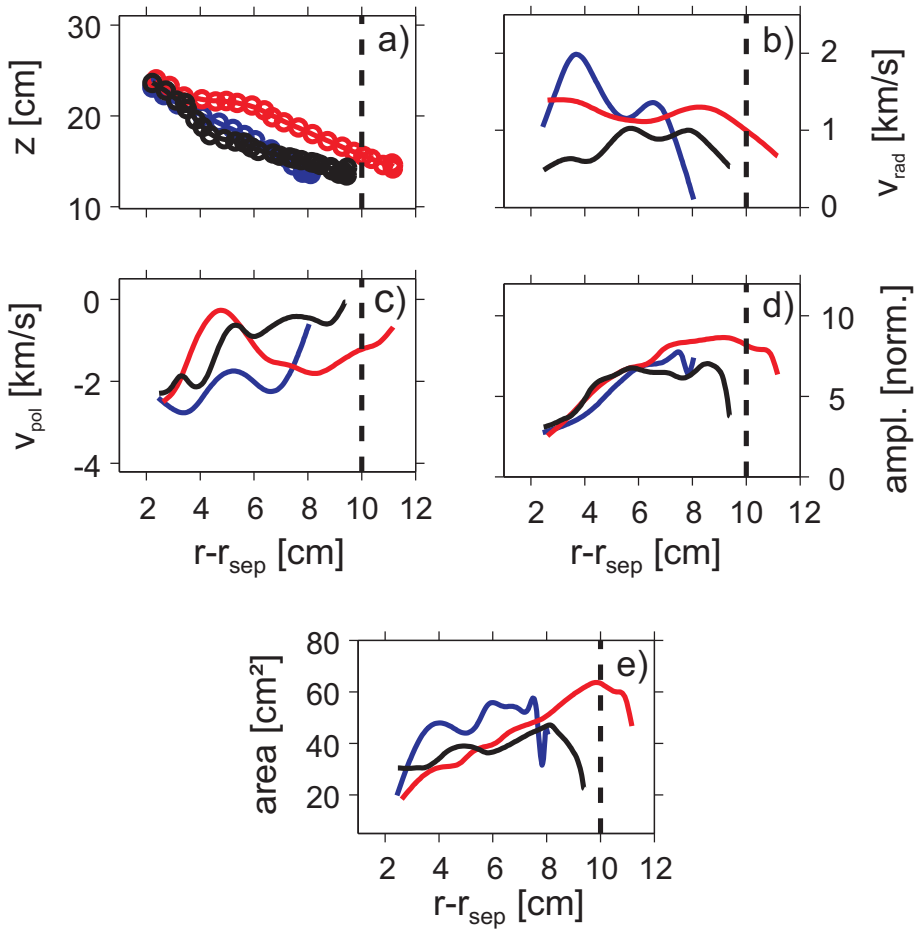

Figure 7.8: Specific properties for three long living individual structures propagating from the plasma edge to the limiter shadow across the SOL. Shown are the structure trajectory (a), the radial (b) and poloidal (c) structure velocities and the evolution of the relative structure amplitude normalized to the time-averaged background D_α emission (d) as well as the structure area (e). The dashed black line corresponds to the minimum radial position of the limiter edge.

structures propagating with a high poloidal or radial velocity are not taken into account in the analysis. The radial evolution of the specific properties of three long-living events is shown in Fig. 7.8.

The structures are detected at $r - r_{sep} \approx 2 \ldots 3\,\mathrm{cm}$ and can be tracked over a radial distance of $6 \ldots 9$ cm. In Fig. 7.8a the trajectories are shown. All structures propagate downwards in the direction of the ion diamagnetic drift and simultaneously radially outwards. The evolution of the radial velocity of the structures with increasing distance to the LFCS is shown in Fig. 7.8b. A positive radial velocity corresponds to a structure propagation radially outwards. Although all structures have approximately the same spatial origin a relatively large spread of the radial velocities in the range 0.5-2 km/s is observed. The radial velocity decreases while the structure propagates into the far-SOL. This is a general feature and has also been reported by other authors [27; 148]. A similar spread is observed in the poloidal velocities of the structures shown in Fig. 7.8c. The poloidal

velocities peak closely behind the LCFS ($r - r_{sep} \approx 3\,\text{cm}$) at a value of $2 - 3\,\text{km/s}$ and decrease towards the limiter shadow to $0 - 1\,\text{km/s}$. Negative poloidal velocities correspond to a downward propagation of the structures.

The radial evolution of the structure amplitudes, normalized to the time-averaged background D_α emission is shown in Fig. 7.8d. The relative amplitudes generally increase while the structures propagate through the SOL and decrease close to and in the limiter shadow. The relative amplitude increases due to the radial evolution of the background radial D_α emission profile (cf. Fig. 3.9c) but also the absolute structure amplitude increases while propagating from the LCFS to the mid-SOL (cf. Fig. 7.6). The decrease of the amplitudes in the limiter shadow region is not a result of the background D_α emission profile but is most likely caused by a strong damping of the structures, due to plasma flow to the limiter. Note that the connection lengths parallel to the magnetic field are considerably reduced in this region. The radial evolution of the structure area (Fig. 7.8e) exhibits almost the same characteristics as the normalized amplitude of the structures.

The analysis of the three individual structures reveals that there is no clear correlation between their radial velocities and specific structure properties. In contrast to the model predictions for structure propagation, the radial velocity is not entirely determined by their relative fluctuation amplitudes and sizes. It must be taken into account, however, that the present analysis is based on three individual events. To investigate the dependence on a statistical solid basis, the same kind of analysis must be done for a large ensemble of events. This is done in the next section.

7.4 Statistical analysis of the radial structure velocities

To gain a better picture of the scaling statistics of the radial structure velocity with respect to the structure amplitude and structure area, a large number of events has been collected, that satisfy the imposed amplitude and area conditions. 11 shots (#113733-#113744) with similar plasma conditions have been analyzed. For the statistical analysis, all extracted structures with a minimum lifetime of $\tau \geq 40\mu\text{s}$ (corresponding to 10 frames) are taken into account. The scaling properties of the blobs radial velocities are investigated in detail for two different radial segments of the PSI5 camera field-of-view.

The first segment ($r - r_{sep} = -3 \ldots 2\,\text{cm}$) corresponds to the LCFS and near SOL, the second segment covers the remaining SOL and limiter shadow ($r - r_{sep} = 2 \ldots 8\,\text{cm}$). All structures detected in those two regions are extracted with respect to an area and amplitude threshold. The radial and poloidal velocities are calculated for two consecutive frames, respectively. In this way, 338 structures contribute to the statistics in the plasma edge and 1980 structures in the SOL region. The resulting probability distribution function (PDF)

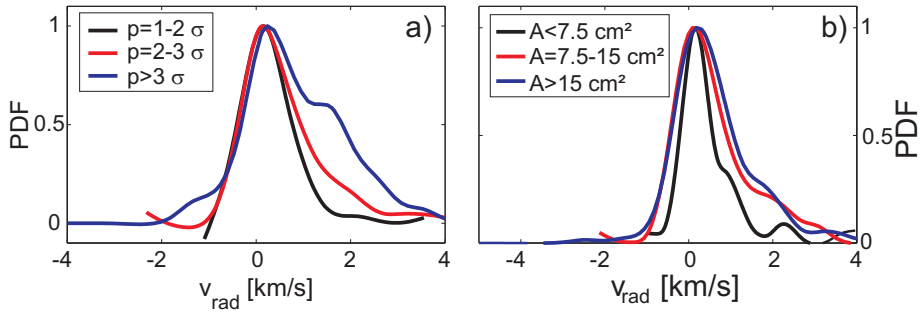

Figure 7.9: Normalized probability distribution functions (PDF) of the radial structure velocity in the range $r - r_{sep} = -3 \ldots 2\,\mathrm{cm}$ for structures with various amplitudes (a) and areas (b).

of the radial structure velocity in the range $r - r_{sep} = -3 \ldots 2\,\mathrm{cm}$ is shown in Fig. 7.9 for three different amplitude and area threshold conditions. In general the PDFs of the radial structure velocity confirm the findings from the individual structure analysis (see above). The distributions are broad with a large spread in the velocity. For structures with high amplitudes $p > 2\,\sigma$, the PDF is asymmetric and skewed towards positive radial velocities (directed radially outwards). The same holds when considering the area dependence of the radial structure velocity in Fig. 7.9b. While the mean value of the radial structure velocity is approximately constant, the PDFs are non-Gaussian and are strongly skewed towards positive radial structure velocities. The resulting PDFs of the radial structure velocity for propagation in the SOL are shown in Fig. 7.10, taking various structure amplitude and structure area conditions. Compared to the plasma edge (Fig. 7.9) the PDFs are generally much more symmetric. However, the widths of the PDFs are significantly larger, corresponding to a larger spread in radial velocities. In contrast to the edge and near SOL, the center-of-mass position of the PDFs are shifted towards higher radial velocities if either the structure amplitude or size increases. This means, on average, higher amplitude structures propagate faster in the SOL. The results for the area dependence of the radial structure velocity in the SOL are not as clear as in the plasma edge (Fig. 7.9b). But a

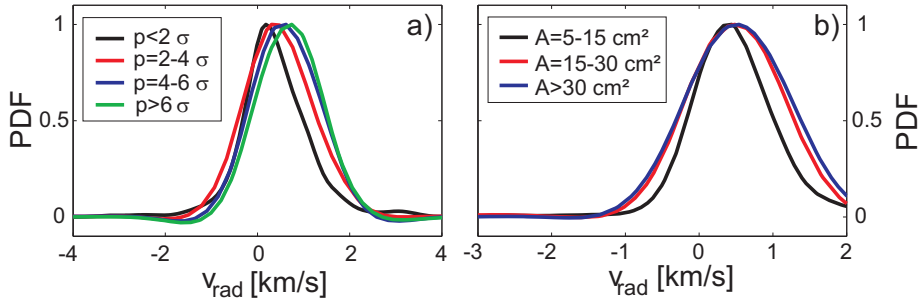

Figure 7.10: Normalized probability distribution functions (PDF) of the radial structure velocity in the range $r - r_{sep} = 2 \ldots 8\,\mathrm{cm}$ for structures with various amplitudes (a) and areas (b).

similar dependence as for the structure amplitude is observed.

7.5 Discussion of NSTX results

In the previous section it has been demonstrated that the convective cross-field transport in the SOL, observed in NSTX L-mode discharges, is governed by large-scale turbulent structures. Typical poloidal wavenumbers normalized to the ion gyroradius are $k_\theta r_{ci} \approx 0.1 - 0.3$ (assuming $T_i = T_e$). This scaling has also been observed in other fusion devices [23; 129; 152]. The structures propagate poloidally in the direction of the ion diamagnetic drift and radially outwards, crossing the SOL and drifting towards the limiter shadow. Typical poloidal structure velocities are $2 - 4\,$km/s in the plasma edge and $0 - 2\,$km/s in the SOL. Estimated radial velocities are $0.5 - 2\,$km/s (corresponding to approximately $1 - 10\,\%$ of the local ion sound speed). Previous studies of GPI data from NSTX mainly confirm the results presented here [28; 81]. In contrast to the results presented here, in those studies the structure velocities are analyzed using two-point cross-correlation techniques. The observed radial blob velocity is in agreement with observations made in other toroidal machines [27; 153; 29]. The radial propagation of structures from the LCFS position into the far SOL causes the intermittent behavior of density fluctuations in the SOL, which is also observed in the fluctuation time series. A statistical analysis of the scaling of the radial structure velocity with structure amplitude and area for long-living structures with lifetimes $\tau \geq 40\,\mu$s reveals that structures with larger amplitudes propagate faster in the SOL than smaller ones. Also a scaling of the radial structure velocity with the spatial size of the structures has been observed. However, the distributions are broad and a detailed quantitative analysis is difficult to achieve.

Different model descriptions addressing the formation and radial propagation of the structures have been developed. They usually rely on an interchange-type polarization of the structure due to curvature and $\nabla \boldsymbol{B}$-drifts (Fig. 7.2b). The resulting poloidal electric field then gives rise to a radial $\boldsymbol{E}\times\boldsymbol{B}$-drift of the structure. The radial velocity of the structure in the SOL is strongly influenced by parallel currents along the magnetic field. They balance the electric field and can inhibit a radial propagation of the structure. It is evident that the magnetic field topology and the plasma resistivity both affect the parallel current. Different instability regimes addressing these effects have been proposed (Tab. 7.1). Each instability regime makes a distinct scaling prediction for the radial structure velocity.
The experimental findings of the present work are consistent with a velocity scaling as predicted in the so-called ballooning regime, where the structure is not connected along the magnetic field lines with the sheaths at the end plates. This is caused by high plasma

resistivity. This velocity scaling, in which the turbulent origin of the structure is neglected, is identical to the scaling predicted by the interchange model, developed by Garcia *et al* [141]. That model considers both the formation and the radial propagation of the structure. One may conclude that the radial propagation of the structure in the SOL is a self-consistent feature of the structure and is not associated with the actual formation process out of the turbulence. However, it has been observed that the amplitude of the structures strongly decreases in the far-SOL and limiter shadow. This cannot be explained by the profiles of the background D_α emission intensity but is most likely due to a parallel flow to the material boundaries. This yields evidence that the parallel dynamics must be retained in the model descriptions. Indeed, in the two-dimensional interchange model, a decrease of the radial structure velocity is observed if the parallel currents are explicitly taken into account as a dissipation mechanism. The three-dimensional models which consider this effect (the X-point and sheath-connected instability regime) are expected to be valid for NSTX edge plasma parameters [148], but they predict a scaling law for the radial blob velocity, which is not observed here.

In Ref. [148] GPI data of NSTX L-mode shots has been analyzed and was found to be consistent with the theoretical predictions of the X-point and sheath-connected instability regime. In particular it was observed that smaller structures propagate in the SOL faster than larger structures. These different conclusions are mainly caused by the subtle definition of the structure area. It is based here on the amplitude of the structure, normalized to the time-averaged D_α emission. In Ref. [148] the background D_α emission intensity profiles and radial profiles of the electron density and temperature (measured with Thomson scattering) are used to obtain directly the density fluctuations. These are nonlinearly coupled to the D_α emission intensity. However, it has been demonstrated recently by numerical simulations of the self-consistent structure dynamics in the SOL (based on the interchange instability [154]), that the propagation models compiled in Tab. 7.1 are not sufficient to describe the structure propagation across the SOL. In these models the structures are treated as isolated structures. It was found that the interaction of background poloidal flows with the structures due to radial electric fields strongly affect their dynamics. Fluctuations in the density, potential and vorticity fields act as a noise that randomly varies the structure dynamics and thereby broadens the distributions of the radial blob velocity.

8

Summary and conclusion

In the present thesis intermittent plasma fluctuations and their relation to the spatiotemporal dynamics of turbulent structures have been investigated. During the last few years experimental observations in the edge and scrape-off layer (SOL) of fusion devices with toroidal geometry revealed that turbulent transport across the confining magnetic field is dominated by large-scale coherent structures - called ”blobs” - that form in the steep radial pressure gradient region close to the last closed flux surface and propagate radially outwards. Different model approaches have been proposed for the explanation of the radial blob propagation. They predict a scaling of the radial blob velocity based with specific blob parameters as amplitude (relative to the background) and scale size. Two-dimensional fluctuation data obtained from fast-framing camera recordings on the NSTX device has been discriminated against those parameters. The analysis of fluctuation events reveals a large spread of the radial blob velocity with a nearly Gaussian probability distribution function. The results clearly demonstrate that the radial velocity is not entirely controlled by the above mentioned blob parameters. Various effects as dissipation, magnetic field geometry and large-scale flows, which are intuitively expected to influence the blob dynamics, are not properly taken into account in the established model descriptions. Furthermore an evaluation has been made for events that occur at nearly identical parameters, which strongly suggests that the actual blob propagation is significantly influenced by the small-scale turbulent fluctuations. This leads to the observed statistical spread. We note that small-scale turbulent fluctuations have not yet been included in the blob models. However, the general trends of radial velocity scaling as obtained from the measurements are roughly along the line of the model predictions.

Intermittent fluctuations have also been reported in linearly magnetized plasmas. Their origin has been experimentally investigated in the VINETA device. In addition three-dimensional global numerical simulations with the CYTO code were done. A major advantage of VINETA is the good control of the governing instability, the density gradient driven drift-wave instability. Both in experiment and computer simulation a transition from single coherent drift modes to a weakly-developed turbulent state is observed if ex-

ternal control parameters are varied, as e.g. the magnetic field, that controls the ratio of the pressure gradient scale length to the drift wave scale $L_\perp/\rho_s$. The observation of saturated coherent drift wave modes and the clear demonstration of the role of the ratio $L_\perp/\rho_s$ in the simulation (in agreement with the experiment) is a novel observation and has never been reported for Hasegawa-Wakatani-like simulations. The transition to weakly developed turbulence is accompanied by nonlinear coupling of drift modes. In particular the development of drift modes by three-wave interaction has been investigated using bicoherence analysis. In the turbulent state two different spatial regions must be distinguished: The maximum radial density gradient region is dominated by quasi-coherent drift mode remnants and in the plasma edge an intermittent behavior of turbulent fluctuations is observed. They are characterized by high-amplitude density bursts. A causal connection between the turbulent structures and the quasi-coherent drift-wave mode could be established in experiment and simulation. The formation of the turbulent structures in the maximum density gradient region is caused by an increase of the phase shift $\delta(\tilde{n}, \tilde{\phi})$ between the density and the potential perturbations, associated with the quasi-coherent drift mode. While the phase shift is small for single coherent drift modes, in the turbulent state $\delta(\tilde{n}, \tilde{\phi}) \approx \pi/2$ is observed. Consequently the radially outwards directed fluctuation-induced transport is strongly increased. As a result, plasma density peels-off the quasi-coherent drift mode and further propagates radially outwards. This picture is supported by the observation that the density bursts in the plasma edge have a similar amplitude as the quasi-coherent drift mode in the maximum pressure density region. After the structures peeled-off the drift mode, their radial propagation in experiment and simulation is determined by the self-consistent electric field perturbation $\tilde{E}_\theta$ that leads to a radial $\tilde{E}_\theta \times B_z$-drift. The simulation results show that the development of $\tilde{E}_\theta$ is due to the three-dimensional structure and not caused by interactions with neutrals, as suggested by Krasheninnikov [155] and concluded by Carter [123]. The azimuthal velocity of the turbulent structures is mainly given by the background $E_r \times B_z$-velocity. In simulation the turbulent structures propagate azimuthally exactly with $E_r \times B_z$-velocity, whereas in the experiment their azimuthal velocity is a factor of two smaller than the $E_r \times B_z$-velocity. This is probably an artifact introduced by uncertainties in the measurement of the radial potential profile. A contribution of the electron diamagnetic drift to the azimuthal velocity of the turbulent structures would explain the difference, but this is not expected since the structures are disconnected from the drift mode. Different from the SOL of fusion devices, the azimuthal velocity of the turbulent structures is by a factor of $2-3$ higher than their radial velocity, which leads to a spiral motion in the azimuthal plane. A comparison between the azimuthal velocity and the typical burst frequency as observed in single-point measurements leads to the conclusion that each observed density burst is related to a propagating turbulent structure.

As a result the fluctuation-induced transport leads to an intermittent behavior of the particle flux in the maximum density gradient region. Quantitatively, however, the parallel losses dominate over the perpendicular transport and hence no significant broadening of the plasma density profile is found. This is again very much different from the SOL of fusion devices, in which the perpendicular fluctuation-induced transport is of the same order as the parallel loss. This results in increased plasma pressure (shoulders).
The detailed comparison between experiment and simulation has revealed a significant element of the formation and the propagation mechanism of large turbulent structures that form in region of steepest plasma density gradient and then propagate radially outwards. Laboratory experiments, observations in a fusion device and computer simulation form together a consistent physical picture.

Bibliography

[1] O. Reynolds. An experimental investigation of the circumstances which determine whether the motion of water shall be direct or sinuous, and of the law of resistance in parallel channels. *Phil. Trans.*, 174 (1883).

[2] M. Van Dyke. *An album of fluid motion*. The Parabolic Press, Stanford, CA (1982).

[3] U. Frisch. *Turbulence: The Legacy of A. N. Kolmogorov*. Cambridge University Press (1995).

[4] G. L. Brown and A. Roshko. Density effects and large structure in turbulent mixing layers. *J. Fluid Mech.*, 64(JUL24), 775 (1974).

[5] H. Hasegawa, M. Fujimoto, T. D. Phan, *et al.*. Transport of solar wind into Earth's magnetosphere through rolled-up Kelvin-Helmholtz vortices. *Nature*, 430(7001), 755 (2004).

[6] P. F. Winkler and K. S. Long. Far-flung filaments of ejecta in the young supernova remnant G292.0+1.8. *Astronomical Journal*, 132(1), 360 (2006).

[7] C. L. M. H. Navier. Memoire sur les lois du mouvement des fluide. *Mem. Acad. Sci. Inst. France*, 6, 389 (1822).

[8] L. F. Richardson. *Weather prediction by numerical process*. Cambridge University Press (1922).

[9] A. H. Scouten and H. Teerink. *A bibliography of the writings of Jonathan Swift, 2nd ed.*. Univ. of Pennsylvania Press (1963).

[10] A. N. Kolmogorov. Dissipation of energy in locally isotropic turbulence. *Dokl. Akad. Nauk. SSSR*, 32, 16 (1941).

[11] J. Maurer, P. Tabeling, and G. Zocchi. Statistics of turbulence between two counterrotating disks in low-temperature Helium gas. *Europhysics Letters*, 26(1), 31 (1994).

[12] R. H. Kraichnan. Inertial ranges in two-dimensional turbulence. *Phys. Fluids*, 10(7), 1417 (1967).

[13] M. A. Rutgers. Forced 2D turbulence: Experimental evidence of simultaneous inverse energy and forward enstrophy cascades. *Phys. Rev. Lett.*, 81(11), 2244 (1998).

[14] H. Aref and E. D. Siggia. Vortex dynamics of the two-dimensional turbulent shear-layer. *J. Fluid Mech.*, 100(OCT), 705 (1980).

[15] J. C. Mcwilliams. The emergence of isolated coherent vortices in turbulent-flow. *J. Fluid Mech.*, 146(SEP), 21 (1984).

[16] R. Benzi, G. Paladin, S. Patarnello, *et al.*. Intermittency and coherent structures in two-dimensional turbulence. *J. Phys. A: Math. Gen.*, 19(18), 3771 (1986).

[17] V. Borue. Inverse energy cascade in stationary two-dimensional homogeneous turbulence. *Phys. Rev. Lett.*, 72(10), 1475 (1994).

[18] P. Veltri. MHD turbulence in the solar wind: self-similarity, intermittency and coherent structures. *Plasma Phys. Controlled Fusion*, 41, A787 (1999).

[19] R. Kinney, J. C. Mcwilliams, and T. Tajima. Coherent structures and turbulent cascades in two-dimensional incompressible magnetohydrodynamic turbulence. *Phys. Plasmas*, 2(10), 3623 (1995).

[20] R. H. Kraichnan. Inertial-range spectrum of hydromagnetic turbulence. *Phys. Fluids*, 8(7), 1385 (1965).

[21] D. Biskamp. *Nonlinear magnetohydrodynamics*. Cambridge University Press, New York (1993).

[22] J. G. Charney. The dynamics of long waves in a baroclinic westerly current. *Journal of Meteorology*, 4(5), 135 (1947).

[23] A. J. Wootton, B. A. Carreras, H. Matsumoto, *et al.*. Fluctuations and anomalous transport in tokamaks. *Phys. Fluids B*, 2(12), 2879 (1990).

[24] F. Wagner and U. Stroth. Transport in toroidal devices - the experimentalists view. *Plasma Phys. Controlled Fusion*, 35(10), 1321 (1993).

[25] U. Stroth. A comparative study of transport in stellarators and tokamaks. *Plasma Phys. Controlled Fusion*, 40(1), 9 (1998).

[26] J. L. Terry, S. J. Zweben, K. Hallatschek, *et al.*. Observations of the turbulence in the scrape-off layer of Alcator C-Mod and comparisons with simulation. *Phys. Plasmas*, 10(5), 1739 (2003).

[27] J. A. Boedo, D. L. Rudakov, R. A. Moyer, *et al.*. Transport by intermittency in the boundary of the DIII-D tokamak. *Phys. Plasmas*, 10(5), 1670 (2003).

[28] S. J. Zweben, R. J. Maqueda, D. P. Stotler, *et al.*. High-speed imaging of edge turbulence in NSTX. *Nucl. Fusion*, 44, 134 (2004).

[29] O. Grulke, J. L. Terry, B. LaBombard, *et al.*. Radially propagating fluctuation structures in the scrape-off layer of Alcator C-Mod. *Phys. Plasmas*, 13(1), 012306 (2006).

[30] C. Schröder, O. Grulke, T. Klinger, *et al.*. Spatial mode structures of electrostatic drift waves in a collisional cylindrical helicon plasma. *Phys. Plasmas*, 11(9), 4249 (2004).

[31] C. Schröder, O. Grulke, T. Klinger, *et al.*. Drift waves in a high-density cylindrical helicon discharge. *Phys. Plasmas*, 12, 042103 (2005).

[32] N. D'Angelo and R. W. Motley. Low-frequency oscillations in a potassium plasma. *Phys. Fluids*, 6, 422 (1963).

[33] H. Lashinsky. Universal instability in fully ionized inhomogeneous plasma. *Phys. Rev. Lett.*, 12(5), 121 (1964).

[34] F. F. Chen. Normal modes for electrostatic ion waves in an inhomogeneous plasma. *Phys. Fluids*, 7(7), 949 (1964).

[35] F. F. Chen. Spectrum of low-beta plasma turbulence. *Phys. Rev. Lett.*, 15(9), 381 (1965).

[36] H. W. Hendel, T. K. Chu, and P. A. Politzer. Collisional drift waves–identification, stabilization, and enhanced plasma transport. *Phys. Fluids*, 11(11), 2426 (1968).

[37] T. K. Chu, B. Coppi, H. W. Hendel, *et al.*. Drift instabilities in a uniformly rotating plasma cylinder. *Phys. Fluids*, 12(1), 203 (1969).

[38] S. T. Tsai, F. W. Perkins, and R. F. Ellis. Parallel current and sheath effects on collisional drift waves in an axially symmetric device with end plates. *Phys. Fluids*, 15(2), 345 (1972).

[39] H. L. Pecseli, J. J. Rasmussen, and K. Thomsen. Nonlinear interaction of convective cells. *Phys. Rev. Lett.*, 52(24), 2148 (1984).

[40] H. L. Pécseli and T. Mikkelsen. Turbulent diffusion in two-dimensional, strongly magnetized plasmas. *J. Plasma Phys.*, 34(1), 77 (1985).

[41] E. Mazzucato. Small-scale density fluctuations in adiabatic toroidal compressor. *Phys. Rev. Lett.*, 36(14), 792 (1976).

[42] A. Hasegawa and K. Mima. Pseudo-three-dimensional turbulence in magnetized nonuniform plasma. *Phys. Fluids*, 21(1), 87 (1978).

[43] A. Hasegawa and M. Wakatani. Plasma edge turbulence. *Phys. Rev. Lett.*, 50, 682 (1983).

[44] V. Naulin, K. H. Spatschek, S. Musher, *et al.*. Properties of a two-nonlinearity model for drift wave turbulence. *Phys. Plasmas*, 2, 2640 (1995).

[45] F. J. Øynes, H. L. Pécseli, and K. Rypdal. Fluctuations in a magnetized plasma without rotational transform. *Phys. Rev. Lett.*, 75(1), 81 (1995).

[46] W. Horton. Drift waves and transport. *Rev. Mod. Phys.*, 71(3), 735 (1999).

[47] S. I. Braginskii. *Reviews of plasma physics*, vol. 1. Consultants-Bureau (1965).

[48] R. J. Goldston and P. H. Rutherford. *Introduction to plasma physics*. Inst. of Phys. Pub. (1995).

[49] M. Ottaviani and J. A. Krommes. Weak-turbulence and strong-turbulence regimes of the forced Hasegawa-Mima equation. *Phys. Rev. Lett.*, 69(20), 2923 (1992).

[50] P. Terry and W. Horton. Stochasticity and the random phase approximation for three electron drift waves. *Phys. Fluids*, 25(3), 491 (1982).

[51] P. W. Terry and W. Horton. Drift wave turbulence in a low-order k space. *Phys. Fluids*, 26(1), 106 (1983).

[52] J. A. Crotinger and T. H. Dupree. Trapped structures in drift wave turbulence. *Phys. Fluids B*, 4(9), 2854 (1992).

[53] M. Lesieur. *Turbulence in Fuids*. Fluid mechanics and its applications, second edn. Kluwer Academic Publishers, Dordrecht (1990).

[54] A. Zeiler and D. Biskamp. Three–dimensional fluid simulations of tokamak edge turbulence. *Phys. Plasmas*, 3(8), 2951 (1996).

[55] M. Wakatani and A. Hasegawa. A collisional drift wave description of plasma edge turbulence. *Phys. Fluids*, 27(3), 611 (1984).

[56] S. J. Camargo, B. D. Scott, and D. Biskamp. The influence of magnetic fluctuations on collisional drift–wave turbulence. *Phys. Plasmas*, 3(11), 3912 (1996).

[57] V. Naulin, T. Windisch, and O.Grulke. Three dimensional global fluid simulations of cylindrical magnetised plasmas. *to be submitted*.

[58] W. Baumjohann and R. A. Treumann. *Basic space plasma physics*. Imperial College Press, London (1996).

[59] P. C. Stangeby. *The plasma boundary of magnetic fusion devices*. Series in Plasma Physics. IOP Publishing, Bristol, UK (2000).

[60] R. F. Ellis, E. Marden-Marshall, and R. Majeski. Collisional drift instability of a weakly ionized argon plasma. *Plasma Physics*, 22, 113 (1980).

[61] V. Naulin. priv. comm.

[62] C. Schröder. *Experimental investigations on drift waves in a linear magnetized plasma, PhD thesis*. Ph.D. thesis, Ernst-Moritz-Arndt Universität, Greifswald (2004).

[63] M. A. Liebermann and A. J. Lichtenberg. *Principles of plasma discharges and materials processing*. John Wiley & Sons, INC., New York (1994).

[64] H. M. Mott-Smith and I. Langmuir. The theory of collectors in gaseous discharges. *Phys. Rev.*, 28, 727 (1926).

[65] V. I. Demidov, S. V. Ratynskaia, and K. Rypdal. Electric probes for plasmas: the link between theory and experiment. *Rev. Sci. Instrum.*, 73(10), 3409 (2002).

[66] V. I. Demidov, S. V. Ratynskaia, R. J. Armstrong, *et al.*. Probe measurements of electron energy distributions in a strongly magnetized low–pressure helium plasma. *Phys. Plasmas*, 6, 350 (1999).

[67] F. F. Chen. Time-varying impedance of the sheath on a probe in an RF plasma. *Plasma Sources Sci. Technol.*, 15(4), 773 (2006).

[68] I. D. Sudit and F. F. Chen. RF compensated probes for high-density discharges. *Plasma Sources Sci. Technol.*, 3, 162 (1994).

[69] V. Pericoli-Ridolfini, A. Pietropaolo, R. Cesario, *et al.*. Density, temperature and potential fluctuations in the edge plasma of the FTU tokamak. *Nucl. Fusion*, 38(12), 1745 (1998).

[70] A. Latten, T. Klinger, A. Piel, *et al.*. A probe array for the investigation of spatio-temporal structures in drift wave turbulence. *Rev. Sci. Instrum.*, 66(5), 3254 (1995).

[71] I. H. Hutchinson. *Principle of plasma diagnostics*. 2nd ed., Cambridge University Press (2002).

[72] H. J. Hartfuss, T. Geist, and M. Hirsch. Heterodyne methods in millimetre wave plasma diagnostics with application to ECE, interferometry and reflectometry. *Plasma Phys. Controlled Fusion*, 39, 1693 (1997).

[73] H.-J. Kunze. *The laser as a tool for plasma diagnostics, in: Plasma diagnostics*. North-Holland Press, Amsterdam (1968).

[74] D. Johnson, N. Bretz, B. LeBlanc, *et al.*. Multipulse Thomson scattering system for the National Spherical Torus Experiment. *Rev. Sci. Instrum.S*, 70(1), 776 (1999).

[75] G. McKee, R. Ashley, R. Durst, *et al.*. The beam emission spectroscopy diagnostic on the DIII-D tokamak. *Rev. Sci. Instrum.*, 70(1), 913 (1999).

[76] A. Huber, A. V. Nedospasov, U. Samm, *et al.*. Space resolved fluctuations of electron density measured by means of two thermal Li-beams in Textor-94. *J. Nucl. Mater.*, 269, 546 (1999).

[77] G. R. McKee, C. Fenzi, R. J. Fonck, *et al.*. Turbulence imaging and applications using beam emission spectroscopy on DIII-D. *Rev. Sci. Instrum.*, 74(3), 2014 (2003).

[78] S. J. Zweben, D. P. Stotler, J. L. Terry, *et al.*. Edge turbulence imaging in the Alcator C-Mod tokamak. *Phys. Plasmas*, 9(5), 1981 (2002).

[79] J. L. Terry, S. J. Zweben, B. Bose, *et al.*. High speed movies of turbulence in Alcator C-Mod. *Rev. Sci. Instrum.*, 75(10), 4196 (2004).

[80] R. J. Maqueda, G. A. Wurden, D. P. Stotler, *et al.*. Gas puff imaging of edge turbulence (invited). *Rev. Sci. Instrum.*, 74(3), 2020 (2003).

[81] S. J. Zweben, R. J. Maqueda, J. L. Terry, *et al.*. Structure and motion of edge turbulence in the National Spherical Torus Experiment and Alcator C-Mod. *Phys. Plasmas*, 13(5), 056114 (2006).

[82] D. P. Stotler, J. Boedo, B. LeBlanc, *et al.*. Progress towards the validation of models of the behavior of neutral helium in gas puff imaging experiments. *Proc. Conf. Plasma Surface Interactions*, P-3-31 (2006).

[83] D. P. Stotler, D. A. D'Ippolito, B. LeBlanc, *et al.*. Three-dimensional neutral transport simulations of gas puff imaging experiments. *Contrib. Plasma Phys.*, 44(1-3), 294 (2004).

[84] D. P. Stotler, B. LaBombard, J. L. Terry, *et al.*. Neutral transport simulations of gas puff imaging experiments. *J. Nucl. Mater.*, 313-316, 1066 (2003).

[85] D. P. Stotler. Towards a revised Monte Carlo neutral particle surface interaction model. *Physica Scripta*, T124, 23 (2006).

[86] D. L. Rudakov, J. A. Boedo, R. A. Moyer, *et al.*. Fluctuation-driven transport in the DIII-D boundary. *Plasma Phys. Controlled Fusion*, 44(6), 717 (2002).

[87] S. G. Mallat. *A Wavelet Tour of Signal Processing*. Academic Press 2nd edition (1999).

[88] Y. T. Chan. *Wavelet basics*. Kluwer Academic Publishers (1995).

[89] G. Strang. Wavelet transforms versus Fourier-transforms. 28(2), 288 (1993).

[90] P. S. Addison. *The illustrated wavelet handbook*. Institute of Physics Publishing (2002).

[91] B. P. van Milligen. *Wavelets in physics*. Cambridge University Press (1999).

[92] M. Farge, K. Schneider, and P. Devynck. Extraction of coherent bursts from turbulent edge plasma in magnetic fusion devices using orthogonal wavelets. *Phys. Plasmas*, 13(4), 042304 (2006).

[93] Y. C. KIM and E. J. POWERS. Digital bispectral analysis and its applications to non-linear wave interactions. *IEEE Trans. Plasma Sci.*, 7(2), 120 (1979).

[94] Y. C. Kim, J. M. Beall, E. J. Powers, *et al.*. Bispectrum and nonlinear wave coupling. *Phys. Fluids*, 23, 258 (1980).

[95] C. P. Ritz, E. J. Powers, T. L. Rhodes, *et al.*. Advanced plasma fluctuation analysis techniques and their impact on fusion research. *Rev. Sci. Instrum.*, 59(8), 1739 (1988).

[96] T. D. de Wit. *Space plasma simulation*. Springer Berlin (2003).

[97] C. P. Ritz, E. J. Powers, and R. D. Bengtson. Experimental-measurement of three-wave coupling and energy cascading. *Phys. Fluids B*, 1(1), 153 (1989).

[98] J. S. Kim, R. J. Fonck, R. D. Durst, *et al.*. Measurements of nonlinear energy transfer in turbulence in the Tokamak Fusion Test Reactor. *Phys. Rev. Lett.*, 79(5), 841 (1997).

[99] G. D. Conway and J. A. Elliott. Digital signal procesing techniques for plasma dispersion curve measurements. *J. Phys. E: Sci. Instrum.*, 20, 1341 (1987).

[100] M. B. Priestley. *Spectral analysis and time series*. 6 edn. Academic, San Diego (1989).

[101] R. J. Adrian. Conditional eddies in isotropic turbulence. *Phys. Fluids*, 22(11), 2065 (1979).

[102] O. Grulke, T. Klinger, and A. Piel. Experimental study of the dynamics of conditionally averaged structures in weakly developed electrostatic turbulence. *Phys. Plasmas*, 6(3), 788 (1999).

[103] J. P. Rayner, A. D. Cheetham, and G. N. French. Radio frequency matching for helicon plasma sources. *J. Vac. Sci. Technol. A*, 14(4), 2048 (1996).

[104] C. M. Franck, O. Grulke, and T. Klinger. Mode transitions in helicon discharges. *Phys. Plasmas*, 10(1), 323 (2003).

[105] C. M. Franck, O. Grulke, A. Stark, *et al.*. Measurements of spatial structures of different discharge modes in a helicon source. *Plasma Sources Sci. Technol.*, 14 (2): 226-235 MAY 2005, 226 (2005). Accepted for publication.

[106] R. Bowers, F. Rose, and C. Legendy. Oscillatory galvanomagnetic effect in metallic sodium. *Phys. Rev. Lett.*, 7(9), 339 (1961).

[107] F. E. Rose, M. T. Taylor, and R. Bowers. Low-frequency magneto-plasma resonances in sodium. *Phys. Rev.*, 127(4), 1122 (1962).

[108] J. A. Lehane and Thoneman.Pc. An experimental study of helicon wave propagation in a gaseous plasma. *Proc. Phys. Soc.*, 85(544P), 301 (1965).

[109] R. W. Boswell. Plasma production using a standing helicon wave. *Phys. Lett.*, 33A(7), 457 (1970).

[110] R. W. Boswell. Very efficient plasma generation by whistler waves near the lower hybrid frequency. *Plasma Phys. Controlled Fusion*, 26(10), 1147 (1984).

[111] K. Yukimura. Plasma-based ion implantation and its application to three-dimensional materials. *Surf. Coat. Technol.*, 136(1-3), 1 (2001).

[112] C. Charles, R. W. Boswell, and M. A. Lieberman. Xenon ion beam characterization in a helicon double layer thruster. *Appl. Phys. Lett.*, 89(26), 261503 (2006).

[113] F. F. Chen and R. W. Boswell. Helicons - the past decade. *IEEE Trans. Plasma Sci.*, 25(6), 1245 (1997).

[114] Y. Mouzouris and J. E. Scharer. Wave propagation and absoption simulations for helicon sources. *Phys. Plasmas*, 5(12), 4253 (1998).

[115] S. W. Cho and J. G. Kwak. The effects of the density profile on the power absorption and the equilibrium density in helicon plasmas. *Phys. Plasmas*, 4(11), 4167 (1997).

[116] A. Degeling, N. Mikhelson, R. Boswell, *et al.*. Characterization of helicon waves in a magnetized inductive discharge. *Phys. Plasmas*, 5(3), 572 (1998).

[117] A. R. Ellingboe, R. W. Boswell, J. P. Booth, *et al.*. Electron-beam pulses produced by helicon-wave excitation. *Phys. Plasmas*, 2(6), 1807 (1995).

[118] J. Scharer, A. Degeling, G. Borg, *et al.*. Measurements of helicon wave propagation and Ar II emission. *Phys. Plasmas*, 9(9), 3734 (2002).

[119] M. J. Burin, G. R. Tynan, G. Y. Antar, *et al.*. On the transition to drift turbulence in a magnetized plasma column. *Phys. Plasmas*, 12(5), 052320 (2005).

[120] F. Brochard, T. Windisch, O. Grulke, *et al.*. Experimental evidence of mode coupling in drift wave intermittent turbulence using a wave number bicoherence analysis. *Phys. Plasmas*, 13, 122305 (2006).

[121] E. J. Powers. Spectral techniques for experimental investigation of plasma diffusion due to polychromatic fluctuations. *Nucl. Fusion*, 14, 749 (1974).

[122] B. A. Carreras, C. Hidalgo, E. Sánchez, *et al.*. Fluctuation-induced flux at the plasma edge in toroidal devices. *Phys. Plasmas*, 3(7), 2664 (1996).

[123] T. A. Carter. Intermittent turbulence and turbulent structures in a linear magnetized plasma. *Phys. Plasmas*, 13(1), 010701 (2006).

[124] T. Windisch, O. Grulke, and T. Klinger. Radially propagating structures in a linear helicon experiment. *J. Nucl. Mater.*, in press (2007).

[125] O. Grulke, A. Stark, T. Windisch, *et al.*. Plasma profiles in a cylindrical helicon discharge with converging magnetic source field. *Contrib. Plasma Phys.*, 47, 185 (2007).

[126] B. LaBombard, M. V. Umansky, R. L. Boivin, *et al.*. Cross-field plasma transport and main-chamber recycling in diverted plasmas on Alcator C-Mod. *Nucl. Fusion*, 40(12), 2041 (2000).

[127] P. C. Liewer. Measurements of microturbulence in tokamaks and comparisons with theories of turbulence and anomalous transport. *Nucl. Fusion*, 25(5), 543 (1985).

[128] C. Hidalgo. Edge turbulence and anomalous transport in fusion plasmas. *Plasma Phys. Controlled Fusion*, 37(11A), A53 (1995).

[129] M. Endler. The poloidal variation of the radial transport due to electrostatic fluctuations in toroidal magnetic confinement experiments. *Plasma Phys. Controlled Fusion*, 41, 1431 (1999).

[130] X. Garbet. Turbulence in fusion plasmas: key issues and impact on transport modelling. *Plasma Phys. Controlled Fusion*, 43, A251 (2001).

[131] B. Scott. Three-dimensional computation of drift alfvén turbulence. *Plasma Phys. Controlled Fusion*, 39(10), 1635 (1997).

[132] D. A. Russell, D. A. D'Ippolito, J. R. Myra, *et al.*. Blob dynamics in 3D BOUT simulations of tokamak edge turbulence. *Phys. Rev. Lett.*, 93(26), 265001 (2004).

[133] K. H. Burrell. Effects of ExB velocity shear and magnetic shear on turbulence and transport in magnetic confinement devices. *Phys. Plasmas*, 4(5), 1499 (1997).

[134] X. Q. Xu, R. H. Cohen, W. M. Nevins, *et al.*. Turbulence simulations of X point physics in the L-H transition. *Nucl. Fusion*, 42(1), 21 (2002).

[135] K. Itoh, S. I. Itoh, P. H. Diamond, *et al.*. Physics of zonal flows. *Phys. Plasmas*, 13(5), 055502 (2006).

[136] G. Y. Antar, G. Counsell, Y. Yu, *et al.*. Universality of intermittent convective transport in the scrape-off layer of magnetically confined devices. *Phys. Plasmas*, 10(2), 419 (2003).

[137] N. P. Basse, S. Zoletnik, and P. K. Michelsen. Study of intermittent small-scale turbulence in Wendelstein 7-AS plasmas during controlled confinement transitions. *Phys. Plasmas*, 12(1), 012507 (2005).

[138] V. Carbone, G. Regnoli, E. Martines, *et al.*. Intermittency and self-similarity in plasma edge fluctuations. *Phys. Plasmas*, 7(2), 445 (2000).

[139] F. Sattin, N. Vianello, and M. Valisa. On the probability distribution function of particle density at the edge of fusion devices. *Phys. Plasmas*, 11(11), 5032 (2004).

[140] J. A. Boedo, D. Rudakov, R. Moyer, *et al.*. Transport by intermittent convection in the boundary of the DIII-D tokamak. *Phys. Plasmas*, 8(11), 4826 (2001).

[141] O. E. Garcia, V. Naulin, A. H. Nielsen, *et al.*. Computations of intermittent transport in scrape-off layer plasmas. *Phys. Rev. Lett.*, 92(16), 165003 (2004).

[142] S. I. Krasheninnikov. On scrape off layer plasma transport. *Phys. Lett. A*, 283(5-6), 368 (2001).

[143] D. A. D'Ippolito, J. R. Myra, and S. I. Krasheninnikov. Cross-field blob transport in tokamak scrape-off-layer plasmas. *Phys. Plasmas*, 9(1), 222 (2002).

[144] J. R. Myra and D. A. D'Ippolito. Convective transport in the scrape-off-layer by nonthermalized spinning blobs. *Phys. Plasmas*, 11(9), 4267 (2004).

[145] O. E. Garcia, N. H. Bian, and W. Fundamenski. Radial interchange motions of plasma filaments. *Phys. Plasmas*, 13(8), 082309 (2006).

[146] O. E. Garcia, V. Naulin, A. H. Nielsen, *et al.*. Turbulence and intermittent transport at the boundary of magnetized plasmas. *Phys. Plasmas*, 12(6), 062309 (2005).

[147] J. R. Myra and D. A. D'Ippolito. Edge instability regimes with applications to blob transport and the quasicoherent mode. *Phys. Plasmas*, 12(9), 092511 (2005).

[148] J. R. Myra, D. A. D'Ippolito, D. P. Stotler, *et al.*. Blob birth and transport in the tokamak edge plasma: Analysis of imaging data. *Phys. Plasmas*, 13(9), 092509 (2006).

[149] X. Q. Xu, W. M. Nevins, T. D. Rognlien, *et al.*. Transitions of turbulence in plasma density limits. *Phys. Plasmas*, 10(5), 1773 (2003).

[150] D. Farina, R. Pozzoli, and D. D. Ryutov. Effect of the magnetic-field geometry on the flute-like perturbations near the divertor X-point. *Nucl. Fusion*, 33(9), 1315 (1993).

[151] M. Ono, M. G. Bell, R. E. Bell, *et al.*. Progress towards high-performance, steady-state spherical torus. *Plasma Phys. Controlled Fusion*, 45, A335 (2003).

[152] G. R. McKee, C. C. Petty, R. E. Waltz, *et al.*. Non-dimensional scaling of turbulence characteristics and turbulent diffusivity. *Nucl. Fusion*, 41(9), 1235 (2001).

[153] J. Terry, S. Zweben, O. Grulke, *et al.*. Velocity fields of edge/scrape-off-layer turbulence in Alcator C-Mod. *J. Nucl. Mater.*, 337-339, 322 (2005).

[154] P. Ghendrih, Y. Sarazin, G. Attuel, *et al.*. Statistical analysis of turbulent front propagation in the scrape-off-layer. *J. Nucl. Mater.*, 337-339(1-3), 347 (2005).

[155] S. I. Krasheninnikov and A. I. Smolyakov. On neutral wind and blob motion in linear devices. *Phys. Plasmas*, 10(7), 3020 (2003).

List of Publications

Journal Articles

O. Grulke, C. M. Franck, T. Klinger, *et al.*. Electromagnetic waves and instabilities in magnetoplasmas: Ion and electron dynamics of whistler, Alfvén and drift waves. *Contrib. Plasma Phys.*, 45(5-6), 385, (2006).

T. Windisch, O. Grulke, and T. Klinger. Radial propagation of structures in drift wave turbulence. *Phys. Plasmas*, 13(12), 122303 (2006).

F. Brochard, T. Windisch, O. Grulke, *et al.*. Experimental evidence of mode coupling in drift wave intermittent turbulence using a wave number bicoherence analysis. *Phys. Plasmas*, 13(12), 122305 (2006).

O. Grulke, A. Stark, T. Windisch *et al.*. Plasma profiles in a cylindrical helicon discharge with converging magnetic source field. *Contrib. Plasma Phys.*, 47(3), 185 (2007).

Conference Articles

T. Windisch, O. Grulke, and T. Klinger. Propagating structures in drift-wave turbulence. *Phys. Scripta*, T122, 15, (2005).

R. Schrittwieser, G. Amarandei, C. Ionita C, *et al.*. Results of direct measurements of the plasma potential using a laser-heated emissive probe. *Phys. Scripta*, T123, 94, (2006).

G.N. Kervalishvili, R. Kleiber, R. Schneider, *et al.*. Gyrofluid turbulence modelling of the linear device VINETA. *Contrib. Plasma Physics*, 46(7-9), 739, (2006).

T. Windisch, O. Grulke, and T. Klinger. Radially propagating turbulent structures in a linear helicon plasma device. *J. Nucl. Mater.*, *in press*, (2007).

Conference Oral Presentations

T. Windisch, O. Grulke, and T. Klinger. Structure formation in drift-wave turbulence in the Vineta device. *Third Nordic Symposium on Plasma Physics*, Oslo (2004).

T. Windisch, O. Grulke, and T. Klinger. Intermittenter Transport in linearer Magnetfeldgeometrie. *Frühjahrstagung der Deutschen Physikalischen Gesellschaft*, Augsburg (2006).

Conference Poster Presentations

T. Windisch, O. Grulke, and T. Klinger. Blobs - Eruptive Transportvorgänge in der fernen Abschälschicht. *Frühjahrstagung der Deutschen Physikalischen Gesellschaft*, Berlin (2005).

T. Windisch, O. Grulke, and T. Klinger. Intermittent spatiotemporal turbulent structures in a linear helicon experiment. *33nd European Physical Society Conference on Plasma Physics*, Rome (2006).

O. Grulke, T. Windisch, and T. Klinger. Dynamics of turbulent structures in weakly developed drift-wave turbulence. *17nd Conference on Plasma Surface Interactions*, Hefei, (2006).

Curriculum Vitae

Thomas Windisch
Suermondtstrasse 54
13053 Berlin

born 15.04.1978 in Berlin, married, one child

School education and alternative service

1984-1990	primary school ”7. POS”, Berlin
1990-1997	grammar school ”Otto-Nagel-Gymnasium”, Berlin
Juni 1997	Abitur (grade 2.1)
Sep. 97-Oct. 98	alternative service (hospital Berlin-Grunewald)

Academic education

Oct. 98-Dec. 03	physics at ”Humboldt-Universität zu Berlin”
Dec. 03	physics diploma (grade 1.5) (subsidiary subject: photonics)
Mar. 04	start Ph.D. project
	”Intermittent events and structure propagation in plasma turbulence”
since Mar. 04	enrolled in the ”IMPRS on Bounded Plasmas”
projected Apr. 07	Ph.D. graduation

Work Experience and Research stay

Apr. 02-Feb. 04	scientific staff member at ”Institut für wissenschaftlichen Gerätebau”, Berlin
Aug. 06-Sep. 06	guest researcher at Princeton Plasma Phyiscs Laboratory (PPPL), USA

Acknowledgements

There are numerous people who supported me during this work, scientifically and socially. A convenient attribute of the VINETA group is that the latter branches are closely related. First of all I thank Prof. Klinger for his offer to do my Ph.D. thesis in his group. His scientific enthusiasm and expertise mainly influenced my decision to move from the capital to the Hanse League town close to the Baltic sea. At the start of my Ph.D. project the current research field was quite new for me. Prof. Grulke is gratefully acknowledged for shedding light into this subject. Prof. Klinger, Prof. Grulke and A. Stark did an elaborative proof-reading. A special thank goes to A. Stark for saving at least some probe arrays from his occasionally occurring and redoubtable lab cleaning events. The simulation codes used in the thesis were written by V. Naulin, whose constant interest in the results lead to fruitful progress. Further I thank S. Zweben for the invitation to PPPL and the possibility to work on his data. I'm strongly indebted to my wife who partly deferred her own career while taking care of our son. Although my son won't read this thesis within the next 15 years (if at all), I apologize for the last two years I couldn't participate in our family life during the week. As always I'am much obliged to my parents and relatives who always support me in my decisions.

Eidesstattliche Erklärung

Hiermit erkläre ich an Eides statt, dass diese Arbeit bisher von mir weder der Mathematisch-Naturwissenschaftlichen Fakultät der Ernst-Moritz-Arndt-Universität Greifswald noch einer anderen wissenschaftlichen Einrichtung zum Zwecke der Promotion eingereicht wurde.
Ferner erkläre ich, dass ich diese Arbeit selbstständig verfasst und keine anderen als die darin angegebenen Hilfsmittel benutzt habe.

Greifswald, im März 2007

_____

(Thomas Windisch)